

https://dspace.org/

Investigating the metal dusting behaviour of surface modified 304L stainless steel

Mgwebi, Yonela A

2019
https://hdl.handle.net/10539/28420

Downloaded from a DSpace repository. https://dspace.org/

Investigating the Metal Dusting Behaviour of Surface Modified 304L Stainless Steel

MSc RESEARCH DISSERTATION:

Prepared by

Yonela A Mgwebi (519691)

Submitted to

School of Chemical and Metallurgical Engineering, Faculty of Engineering and the Built Environment, University of the Witwatersrand, Johannesburg, South Africa

Master of Science in Engineering by research only: A dissertation submitted to the Faculty of Engineering and the Built Environment, University of the Witwatersrand, Johannesburg, in fulfilment of the requirements for the degree of Master of Science in Engineering.

Johannesburg, 2019

Declaration

I declare that this thesis* is my own unaided work. It is being submitted to the Degree of Master of Science to the University of the Witwatersrand, Johannesburg. It has not been submitted before for any degree or examination to any other University.



……

(Signature of Candidate)

…29…. day of ……May……., in the year ……2019……

(day) *(month)* *(year)*

Abstract

Metal dusting is a catastrophic carburisation process where the affected metal is weakened by embrittlement due to an increase in carbon content and it subsequently disintegrates. The high velocity gases found in metal dusting environments erode away the brittle material resulting in the metal dusting corrosion product – coke, metal oxides and graphitic carbon. Environments favourable for metal dusting contain high carbon activities ($aC > 1$) at temperatures of 400-800^{o}C and oxygen partial pressures as low as 10^{-24} atm. Such environments are encountered in the chemical, petroleum and petrochemical industries where syngas (H_2-CO-H_2O-CO_2) and hydrocarbons are converted into other useful products.

The objective of this work was to design an experimental rig that simulates a metal dusting environment and then study the behaviour of two types of surface modifications on 304L stainless steel exposed to a metal dusting environment. The two surface modification methods were: (a) copper electroplating using the pulse plating method at varied deposition times of 30, 45 and 60 minutes and (b) laser cladding 304L with ruthenium of varied concentrations in the range (0-5 wt.%Ru).

The following conditions were used to simulate the metal dusting environment; a gas mixture of 20 vol.% CO- 60 vol.% H_2- 20 vol.% H_2O, at 525^{o}C and 650^{o}C, with resultant carbon activities of 0.679 and 0.512 atm respectively. And oxygen partial pressures of 1.599×10^{-27} at 525^{o}C and 5.118×10^{-24} atm at 650^{o}C. An additional metal dusting environment with a relatively high carbon activity was simulated. This environment contained a gas mixture of 25 vol.% CO- 75 vol.% H_2, at 650^{o}C with a carbon activity of 35 atm and an oxygen partial pressure of 1.012×10^{-24} atm. The samples were exposed for a total of 21 days and analysed after seven days and after 21 days of exposure. The samples were analysed using FESEM, Raman Spectroscopy and GIXRD.

The results showed that the copper plated samples performed the best in terms of protecting the 304L stainless steel against metal dusting. However, the copper coating was susceptible to oxidation which could not be slowed down. Increasing deposition

time resulted in increased coating thickness which in turn resulted in prolonged protection against metal dusting by the copper coating. However, a longer exposure time would result in the eventual removal of the copper by oxidation, exposing the 304L stainless steel substrate as was the result in the sample exposed at 650°C, in the gaseous environment with a carbon activity of 35 atm.

The ruthenium laser cladded samples performed well in the low carbon activity environment particularly at 525°C. Metal dusting initiation began 21 days on only the 2 wt.% Ru sample. Exposure at 650°C resulted in the spalling of the oxide layer formed on the samples and the initiation of metal dusting within seven days of exposure. However, in the low carbon activity environment the samples were able to self-heal and maintain relatively low levels of attack. Only pits smaller than 1 μm had formed on the substrate that was exposed as a result of the spalling of the oxide.

Samples exposed to the high carbon activity (35 atm) environment revealed that the high ruthenium (2-5 wt.%) containing samples were highly susceptible to metal dusting, resulting in large pits greater than 20 μm. The pitting occurred at the areas enriched with ruthenium. In contrast, the low ruthenium content samples (0 and 0.5 wt.% Ru), underwent metal dusting initiation as opposed to pitting even after 21 days of exposure. It was identified that to achieve maximum benefit from the ruthenium laser cladded samples against metal dusting, a single phase coating may be applied.

Conferences and Publications

This thesis is based on research carried out at the University of the Witwatersrand, Johannesburg which includes the following papers and conference presentations:

1. Y.A. Mgwebi and J.W. van der Merwe, "*Behaviour of ruthenium laser cladded stainless steel in carbonaceous environments*", presented at the University of the Witwatersrand, 7th Cross Faculty Postgraduate Symposium and IOM^3 young lecturer's competition 2016. (Third best speaker in the Engineering Faculty & 3rd place winner at IOM^3 SA)
2. Y.A. Mgwebi and J.W. van der Merwe, "*Effect of ruthenium laser cladding on metal dusting of 304L stainless steel*", African Journal of Corrosion, Vol. 1, no. 2, pp. 46-55. Presented at African Corrosion Congress 2016, Midrand, South Africa, (2016).
3. Y.A Mgwebi and J.W. van der Merwe, "*Metal dusting behaviour of laser cladded 304L stainless steel, enriched with ruthenium*", Conference Proceedings: EUROCORR- European Corrosion Congress 2016. Presented at the Annual Congress of the European Federation of Corrosion Congress, Montpellier, France, (2016).
4. Y.A. Mgwebi and J.W. van der Merwe, "*Metal dusting behaviour of annealed copper-plated 304 stainless steel*", Conference Proceedings: Ferrous 2016- Ferrous and base metals development network conference, Symposium Series S9, pp.111-120. Presented in Durban, South Africa, (2016).
5. Y.A. Mgwebi and J.W. van der Merwe, "*The behaviour of ruthenium laser cladded 304L, in metal dusting environments*", Conference Proceedings: AMI Precious Metals 2017: The precious metals development network (PMDN) conference in association with Platinum 2017, Symposium Series S94, pp.219-231. Presented in Polokwane, South Africa, (2017).
6. Y.A. Mgwebi and J.W. van der Merwe, "*Studying the metal dusting resistance of copper ion implanted 304l stainless steel*", Conference Proceedings: Microscopy Society of Southern Africa, vol. 47, p.30. Presented in Bela-Bela, South Africa (2017).
7. F. Moyo, J.W. van der Merwe, D. Wamwangi and Y.A. Mgwebi, "*Cathodic modification of stainless steels with ruthenium: a review of recent advances in making the cheaper option cheaper*", Corrosion Review, pp. 1-10, (2018). [Currently available online]

Dedication

This is dedicated to my family that has been very supportive throughout my masters: to my mother, **Notemba Queen Qangule-Mgwebi** for her endless support and chastisement when I would not type during the holidays. My siblings, who encouraged me to do my best: **Nindiphiwe Qangule**, **Sande Mgwebi** and **Ovayo Mgwebi**. Not forgetting my nephew who has brought hope and light to my life **Avethandwa Owam Qangule**. And **God,** for carrying me through to the end.

Isaiah 40:28-31

"Do you not know? Have you not heard? The LORD is the everlasting God, the Creator of the ends of the earth. He will not grow tired or weary, and his understanding no one can fathom. He gives strength to the weary and increases the power of the weak. Even youths grow tired and weary, and young men stumble and fall; but those who hope in the LORD will renew their strength. They will soar on wings like eagles; they will run and not grow weary, they will walk and not be faint."

Acknowledgements

I would like to first thank my supervisor **Prof. Josias van der Merwe** for his support and his patience with my many never ending suggestions, allowing me the opportunity to think outside the box and allowing me the freedom to fail and rise again. I would also like to thank the **NRF-DST Centre of Excellence in Strong Materials, NRF and the DST-SA,** for their financial assistance throughout my project and the Centre's staff who were very patient and understanding. I would also like to thank **CorrISA** for the recognition and endorsement of my project when they awarded me with the prestigious **Ivan Oglivie** award. Thank you to **Mr Gregory Combrink** as well for his invaluable input and encouragement.

I would also like to thank the technical staff at the School of Chemical and Metallurgical Engineering. I have to name these great humans **Tat'Shadrack Moqabulane** for his 1 μm polishing resin for my very stubborn 304L stainless steel. The **RW-CHMT workshop staff** for helping with strength when I was failing in that department, their ideas and their willingness to help especially **Hopwell Gumede** who went over and beyond his duties to see me through to the finish of this project. Thank you to **Shahil Ramallal** for helping with the initial setup designs. I would also like to thank **Sifiso** the senior technician at the high voltage lab, in the **School of Electrical and Information Systems Engineering**. I would also like to thank **Ndivhuwo Nelwalani** for the outstanding SEM results, **Dr Steven Lotter** from **Necsa** for offering to help us generate the GD-OES and Raman Spectroscopy results and their interpretation. **Ithemba labs**: **Tony Miller**. I would like to give a big thank you to **Mr Paul Den Hoed** for his unending patience and willingness to help and go out of his way to find resources for the progress of my work for his efforts to help find the necessary resources to put my experimental rig together and the School of Chemistry for their help.

Not forgetting my support system, **Fortunate Moyo** who took me under her wing and has helped me both academically and emotionally when this project was falling apart. Not forgetting **Dr Rodney Genga** for always encouraging me to hold on and that I should focus and God will pave the way for me. Thank you to the multitudes of postgraduate students that have helped me and mentored me even indirectly. I also thank the **MMU staff** for their patience and forever smiling faces, which made it easier to approach them. **My loving family and friends especially Matsobane Nong, LeeAnne Masilela and Takudzwa Magada.**

Contents

Declaration i
Abstract ii
Conferences and Publications iv
Dedication v
Acknowledgements vi
List of Figures x
List of Tables xiv
List of Symbols xv
Nomenclature xvii
1 Introduction 1
1.1 Problem Statement 2
1.2 Research Questions 3
1.3 Aim 3
1.4. Research Objectives 3
1.4 Limitations 4
1.5 Project Outline 4
1.6 References 5
2 Literature Review 9
2.1 Mechanisms of Metal Dusting 10
2.1.1 Type I 10
2.1.2 Type II 10
2.1.3 Type III 11
2.1.4 Type IV 11
2.2 Protective methods against metal dusting 12
2.2.1 Changes in the Process Conditions 13
2.2.2 Protective Oxide Layer 13
2.2.3 Surface Poisoning 16
2.2.4 Mechanical Surface Treatments 16
2.2.5 Chemical Surface Treatments 16
2.2.6 Laser Treatments 18

2.2.7 Alloying Elements 18
2.2.8 Coatings 21
2.3 Copper 25
2.4 Ruthenium 26
2.5 Electroplating 28
2.6 Laser Cladding 29
2.7 References 31
3 Experimental Methods 44
3.1 Materials 44
3.2 Surface Modification 44
3.2.1 Copper Electroplating 44
3.2.2 Laser Cladding 45
3.3 Material Characterisation 46
3.4 Experimental Rig Design 47
3.4.1 Safety Precautions 49
3.5 Metal Dusting Exposure Tests 50
3.6 Post Exposure Characterisation 51
3.7 References 51
4 Results and Discussion 52
4.2 Stainless steel 304L 52
4.2.1 Pre-exposure material characterisation 52
4.2.2 Post exposure results 53
4.2.3 Discussion 66
4.2.4 Chapter Summary 68
4.2.5 References 69
4.3 Copper Electroplating 73
4.3.1 Pre-exposure material characterisation 73
4.3.2 Post-exposure results 79
4.3.3 Discussion 92
4.3.4 Summary 93
4.3.5 References 94

4.4 Ruthenium Laser Cladding 97
4.4.1 Pre-exposure material characterisation 97
4.4.2 Post exposure results 104
4.4.3 Discussion 124
4.4.4 Summary 127
4.4.5 References 128
5. Conclusions 132
6. Recommendations 133

List of Figures

Figure 2.1: Schematic of the metal dusting mechanism for austenitic stainless steel and nickel alloys [36]. 12
Figure 3.1: Electrochemical setup for the copper electroplating process. 45
Figure 3.2: Shows the (a) metal dusting experimental rig and (b) schematic diagram of the steam reactor. 48
Figure 4.1: FESEM-BSE micrograph of the austenitic 304L grains before exposure. 52
Figure 4.2: Typical XRD spectrum of the 304L stainless steel. 53
Figure 4.3: Mass change after exposure to an environment favourable for metal dusting for 504 hours at 525°C (a_C < 1 atm), 650°C (a_C < 1 atm) and 650°C (a_C >> 1 atm) 54
Figure 4.4: (a) FESEM-BSE and (b) FESEM-SE micrographs of 304L exposed for seven days at 525°C showing minor amounts of corrosion debris, carbon deposits and areas of attack (a) low magnification and (b) high magnification. 56
Figure 4.5: FESEM-BSE micrographs of 304L exposed for seven days at 650°C showing minor amounts of corrosion debris, spalled oxide layer and the substrate at (a) low magnification and (b) high magnification. 57
Figure 4.6: (a) FESEM-BSE image of the 304L surface after 21 days of exposure at 525°C where (A) shows the porous iron rich oxide formed, (B) where the oxide spalled revealing the substrate, (C) oxide particles rich in chromium and (D) carbon rich particles deposited on the 304L stainless steel sample. (b) EDS analysis of the porous iron rich oxide (A). 58
Figure 4.7: FESEM-BSE images of 304L surface after 21 days at 650°C showing (a) spalled oxide and the grain boundary etching inside the pit and (b) iron rich porous oxide, revealed substrate and carbon. 59
Figure 4.8: Raman spectra obtained on the surface of the 304L stainless steel samples exposed at both 525°C and 650°C. 60
Figure 4.9: GIXRD spectra obtained on the surface of the 304L stainless steel samples exposed at both 525°C and 650°C. FESEM-BSE cross-section images of the 304L sample exposed at (a) 525°C and (b) 650˚C. 62
Figure 4.10: FESEM-BSE micrographs of 304L exposed for seven days at 650°C showing the spalled oxide, the substrate and iron rich porous oxide. 63
Figure 4.11: FESEM-BSE micrographs of 304L exposed for 21 days at 650°C showing the spalled oxide, the substrate and iron rich porous oxide. 64
Figure 4.12: (a) Raman and (b) GIXRD spectra obtained on the surface of the 304L stainless steel samples exposed at 650°C for 21 days. 65
Figure 4.13: FESEM-BSE cross-section image of the 304L sample exposed at 650°C. 66
Figure 4.14: FESEM-BSE images of annealed and un-etched samples copper electroplated for (a) 30 minutes, (b) 45 minutes and (c) 60 minutes. 73
Figure 4.15: FESEM-BSE images of annealed and etched samples copper electroplated for: (a) 30 minutes, (b) 45 minutes, and (c) 60 minutes. 74
Figure 4.16: FESEM-BSE showing the difference between the copper coating and the 304L stainless steel substrate, as well as typical measuring points to determine coating thickness. 75

Figure 4.17: Heat-quenched of the copper electroplated samples. 76
Figure 4.18: GDOES plots of depth vs wt% of the electroplated copper samples and the elemental concentration profile of Fe, Ni, Cu, Cr, C, Ni and O at the interface of the copper plated 304L samples: (a) 30 minutes, (b) 45 minutes and (c) 60 minutes. 77
Figure 4.19: XRD spectra of surface of the samples electrodeposited with copper for 30, 45 and 60 minutes. 78
Figure 4.20: Hardness profiles at the interface of the cross-section of the electroplated 304L stainless steel..... 79
Figure 4.21: Change in mass of the 304L stainless steel copper electroplated for 30,45 and 60 minutes, exposed for 21 days at 525 and 650˚C. 79
Figure 4.22: FESEM-BSE images after seven days of exposure for samples electroplated for (a) 30 minute exposed at 525ºC (b) 30 minutes exposed at 650ºC, (c) 45 minutes exposed at 525ºC, (d) 45 minutes exposed at 650ºC, (e) 60 minutes exposed at 525ºC and (f) 60 minutes exposed at 650ºC. 82
Figure 4.23: FESEM-BSE after 21 days of exposure for samples electroplated for (a) 30 minutes exposed at 525ºC, (b) 30 minutes exposed at 650ºC, (c) 45 minutes exposed at 525ºC, (d) 45 minutes exposed at 650ºC, (e) 60 minutes exposed at 525ºC and (f) 60 minutes exposed at 650ºC. 84
Figure 4.24: (a) Raman spectra and (b) GIXRD spectra of the samples copper electroplated for 30, 45 and 60 minutes exposed for 21 days. 85
Figure 4.25: FESEM-BSE cross-section after 21 days of exposure for samples (a) 30 minutes exposed at 525ºC, (b) 30 minutes exposed at 650ºC, (c) 45 minutes exposed at 525ºC, (d) 45 minutes exposed at 650ºC, (e) 60 minutes exposed at 525ºC and (f) 60 minutes exposed at 650ºC. 86
Figure 4.26: FESEM-BSE images of samples after seven days of exposure to 650ºC for samples plated for: (a) 30 minutes, (b) 45 minutes and (c) 60 minutes. 88
Figure 4.27: FESEM-BSE after 21 days of exposure for samples plated for (a) 30 minutes at low magnification (b) 30 minutes at high magnification, (c) for 45 minutes and (d) for 60 minutes. . 89
Figure 4.28: (a) Raman spectra and (b) GIXRD spectra of the copper electroplated samples exposed for 21 days at 650ºC. 90
Figure 4.29: FESEM-BSE cross-section after 21 days of exposure at 650ºC, with a carbon activity of 35 atm, for samplescopper plated for: (a) 30 minutes (b) 45 minutes (c) 60 minutes. 91
Figure 4.30: FESEM-SE micrographs of the (a) stainless steel 304L and (b) ruthenium powder used for the laser cladding process. 97
Figure 4.31: FESEM-BSE micrographs of the mixed powders with (a) 0.5 wt.% Ru and (b) 5 wt.% Ru used for the laser cladding process. 98
Figure 4.32: FESEM-BSE micrographs of the loaser cladded region with (a) 0.5 wt.% Ru and (b) 5 wt.% Ru used for the laser cladding process. 98
Figure 4.33: Fe-Ru phase diagram [3]..... 99
Figure 4.34: FESEM-BSD image of etched cross-section showing the contrast between the grains of the substrate and the laser cladding of the 0 and 0.5 wt.% Ru samples. 100

Figure 4.35: FESEM-BSD of the substrate and the laser cladding of the 2-10 wt.% Ru, contrasting different grain images. 101
Figure 4.36: FESEM-SE micrograph of the ruthenium enriched sites on which the ruthenium was removed during the etching process. 102
Figure 4.37: FESEM-SE micrograph of the grain size change from the laser cladding transition to the fusion zone and finally the substrate. 102
Figure 4.38: XRD spectrum of the laser cladded samples. 103
Figure 4.39: Hardness profiles of the laser cladded materials. 104
Figure 4.40: Shows the mass change of the ruthenium laser cladded 304L stainless steel. 104
Figure 4.41: FESEM-BSE micrograph of (a) the 0wt% Ru, showing (b) the 0.5 wt.% Ru, (c) the 2 wt.% Ru and (d) 5 wt.% Ru of the oxide layer after seven days of exposure to a metal dusting environment at 525°C. 106
Figure 4.42: FESEM-BSE micrograph at of the 0 wt.% Ru, showing (a) shows the initiation of spalling of the oxide layer and (b) the spalled oxide, with pits and intergranular attack exposed at 650°C for seven days 107
Figure 4.43: FESEM-BSE micrograph at of the 0.5 wt.% Ru, showing (a) the spalled oxide, showing the substrate and (b) shows intergranular attack exposed to a metal dusting favourable environment at 650°C, for seven days. 108
Figure 4.44: FESEM-BSE micrograph at of the 2 wt.% Ru, showing the cracked and spalled oxide, showing the substrate, intergranular attack and self-healing exposed to a metal dusting favourable environment at 650°C, for seven days. 109
Figure 4.45: FESEM-BSE micrograph at of the 5 wt.% Ru, showing the spalled oxide, showing the substrate and intergranular attack exposed at 650°C, for seven days in a metal dusting favourable environment. 109
Figure 4.46: FESEM-BSE micrograph of (a) the 0 wt.% Ru, showing (b) the 0.5 wt.% Ru, (c) the 2 wt.% Ru and (d) 5 wt.% Ru of the oxide layer exposed to a metal dusting favourable environment at 525°C, for 21 days. 110
Figure 4.47: FESEM-BSE showing pitting and intergranular attack on the 304L substrate exposed at 525°C, for 21 days in a metal dusting favourable environment. 111
Figure 4.48: Raman spectra of the ruthenium laser cladded samples exposed for 21 days. 112
Figure 4.49: GIXRD spectra of the ruthenium laser cladded samples exposed for 21 days. 112
Figure 4.50: Typical FESEM-BSE of the cross-section of the laser cladded samples that have been exposed at 525°C for 21 days. 113
Figure 4.51: FESEM-BSE micrographs showing the oxide layer that formed after exposure at 650°C for 21 days, on the 0 wt.% Ru sample where (a) the oxide layer had spalled revealing the laser cladding (substrate) and, (b) the black particle growing into the oxide layer. 113
Figure 4.52: FESEM-BSE micrograph of the 0.5 wt.% Ru samples showing the spalling of the oxide layer formed after exposure at 650°C for 21 days. 114
Figure 4.53: FESEM-BSE micrograph of the 2 wt.% Ru samples showing (a) the spalling of the oxide layer formed, and (b) growths into the oxide layer. 114

Figure 4.54: FESEM-BSE micrograph of the 5 wt.% Ru samples showing (a) depression in the oxide layer, and (b) the spalled oxide layer after exposure at 650°C for 21 days. 115
Figure 4.55: Raman spectra of the ruthenium laser cladded samples exposed at 650°C for 21 days. 116
Figure 4.56: GIXRD spectra of the ruthenium laser cladded samples exposed for 21 days. 116
Figure 4.57: Typical FESEM-BSE of the cross-section of the laser cladded samples that have been exposed at 650°C for 21 days, showing carbon growths into the laser clad. 117
Figure 4.58: FESEM-BSE micrograph of the (a) 0 wt.% Ru and (b) 0.5 wt.% Ru (c) 2 wt.% Ru and (d) 5 wt.% Ru samples revealing the spalling of the oxide layer and the shallow pits formed exposed at 650°C, for seven days with a_C of 35 atm. 118
Figure 4.59: FESEM-BSE micrograph showing the 5 wt.% Ru sample with a pit filled with corrosion debris, formed after exposure at 650°C, for seven days in a carbon activity of 35 atm. 119
Figure 4.60: FESEM-BSE micrograph of the (a) 0 wt.% Ru and (b) 0.5 wt.% Ru samples revealing the spalling of the oxide layer formed and carbon deposits after exposure at 650°C, for 21 days in a carbon activity of 35 atm. 120
Figure 4.61: FESEM-BSE micrograph of the (a) 2wt% Ru, (b) 5 wt.% Ru samples revealing the corrosion pits after exposure at 650°C, for seven days in a carbon activity of 35 atm. 121
Figure 4.62: Raman spectra of the ruthenium laser cladded samples exposed for 21 days after exposure at 650°C, for 21 days in a carbon activity of 35 atm. 122
Figure 4.63: GIXRD spectra of the ruthenium laser cladded samples exposed for 21 days at 650°C, with a_C = 35 atm. 122
Figure 4.64: Typical FESEM-BSE of the cross-section of the laser cladded samples that have been exposed at 650°C for 21 days (a) showing cracks and oxidation and (b) shows the cross-section of the pits 123

List of Tables

Table 3-1: Composition of the 304L stainless steel. 44
Table 3-2: Target ruthenium compositions of the powdes used for the cladding. 46
Table 3-3: Carbon activity and partial pressure of each exposure gas and temperature. 50
Table 4-1: Approximate thicknesses of the laser cladding. 103

List of Symbols

ΔG° - Gibb's free energy change

R - ideal gas constant (8.314 J /mol.K)

T – absolute temperature

K – equilibrium constant

ΔH° - standard enthalpy change

ΔS° -standard entropy change

a_C - carbon activity established at catalytic surface

a_{C_1}- carbon activity as a result of carbon monoxide reduction

a_X - activity of chemical component

k_0 – adsorption constant of the water formation reaction

$v = \frac{dn_c}{A\,dt} = r$ – rate of coking or metal wastage

m_c – mass of component (e.g. carbon)

k – rate constant

P_{O_2} – oxygen partial pressure

A,B – constants used to calculate ΔG°

t – time (s or min or days)

r_1 – rate of material wastage (mg/cm^2)

r_2 – rate of coking (mg/cm^2)

$\hat{v}$ - specific volume (m^3/kg)

$\dot{m}$ – mass flowrate of water (g/min)

$\dot{Q}$ – volumetric flowrate (mL/min)

$V_{T,gas}$ – total volume of gas

x_i – mole ratio of component i

n_i – moles of component i

CR – corrosion rate (mm/year)

Nomenclature

CO – carbon monoxide

H_2 – hydrogen

CO_2 – carbon dioxide

H_2O – water vapour

CH_4 - methane

Fe_3C - cementite

C – carbon

Fe - iron

PGMs –platinum group metals

P_{O2} – oxygen partial pressure

Cr – chromium

BCC – body centred cubic

FCC – face centred cubic

Si – silicon

Al – aluminium

Cr – chromium

SiO_2 – silicon dioxide/silica

Cr_2O_3 – chromium oxide/ chromia

Al_2O_3 - aluminium oxide/ alumina

Fe_2O_3 – haematite

Fe_3O_4 – magnetite

M_7C_3 & $M_{23}C_6$ – metallic carbides (M = Cr, Fe, Ni)

$(Fe,Cr,Ni)_2O_3$ – oxide spin

1 Introduction

Improved output efficiencies of high temperature applications such as gas and coal gasification for power generation, nuclear power generation as well as petrochemical plants can often be achieved by increasing operating temperatures. High temperature engineering alloys have to be employed and type 304L austenitic stainless steel is one such material. AISI 304L stainless steel is a versatile material with corrosion and creep resistance while retaining its strength and excellent mechanical properties even at high temperatures. It is also the most widely produced and used austenitic stainless steel and can be a cost-effective material. However, at elevated temperatures it can fail due to oxidation, carburisation and metal dusting [1,2].

Metal dusting corrosion is defined as a catastrophic form of carburisation which causes a material to disintegrate into fine metal and graphite dust particles [3-6]. It occurs at intermediate temperatures of 400-800˚C, and in environments with high carbon activities ($a_C > 1$), as well as low oxygen partial pressures. Such environments usually contain hydrocarbons and/or synthesized gas (syngas) composed of CO, H_2, H_2O, CO_2 and CH_4 [6-9]. This phenomenon degrades the desirable properties of typical high temperature engineering materials such as iron, nickel and cobalt based alloys [9-11]. The affected metal is weakened by the increased carbon content, leading to embrittlement and material disintegration. Gases moving at high velocities subsequently erode away the embrittled material thus resulting in the metal dusting corrosion product (coke) [11,12]. The sizeable coke production reduces the process efficiency because of the resultant poor heat transfer and gas flow, therefore increasing process plant operating expenses [13]. Unfortunately no material currently in existence is entirely resistant to this type of attack and stainless steels exhibit pitting penetration rates in the order of 9-12 mm/y whereas low alloyed steels exhibit even higher rates of metal dusting attack [14,15].

Metal dusting poses a major threat to the safety of processing plants, because it can be sudden and unpredictable. The US Department of Energy estimated that should metal dusting be mitigated in the United States, the hydrogen production industry alone could save $220-290 million per annum [16,17]. In South Africa, PetroSA experienced two failures due to metal dusting within a decade. The first failure occurred within just 21 months of commissioning the plant, in 1993 and the second resulted in maintenance costs that amounted to R52 million [18,19]. It is therefore imperative that this type of corrosion be minimised. PetroSA reported that maintenance costs due to metal dusting amounted to R25 million in the 2011 financial year.

This corrosion attack often plagues chemical industries, petrochemical plants, and the energy production industry. In light of South Africa's recent electricity shortage, the control and mitigation of metal dusting corrosion is essential, in the development and growth of industries and subsequently the economy. In the past, research has been largely concentrated on clarifying the mechanisms of metal dusting [11,20-26]. However, in recent years the focus shifted towards finding control measures for the prevention of metal dusting [27-33]. Corrosion is a surface chemistry dependent process, therefore this research attempted to mitigate the metal dusting of 304L by surface modification with ruthenium and copper. Surface modification instead of bulk alloying was considered to minimise the use of alloying elements and minimise costs.

1.1 Problem Statement

Type 304L stainless steel generally exhibits exceptional corrosion and high temperature properties. However, research has shown that it is susceptible to high temperature corrosion such as carburisation and metal dusting, which occur both in the presence and absence of oxygen [34-38]. In recent years, research has shifted towards the investigation of protective methods that can control and mitigate metal dusting attack [39-43]. Some protective methods that have been explored are: alloy development, modifying the corrosive environment, application of coatings and surface modification of alloys [8,15, 39-43].

This research used copper and ruthenium which are readily mined in South Africa, to control the metal dusting of 304L stainless steel. These elements were used for their superior corrosion properties. Copper has an extremely low carbon solubility and does not catalyse carbon deposition, thus rendering it inert to carburization and metal dusting [32,33]. Whereas ruthenium is a noble metal and is non-reactive at temperatures less than 800˚C [44]. Consequently, surface modification techniques, pulse electroplating and laser cladding were used to apply copper or ruthenium to 304L stainless steel, to determine if the metal dusting of 304L stainless steel can be controlled. There has been little or no known research yet on the application of these surface modification techniques combined with the two alloying elements used in this work to control metal dusting.

1.2 Research Questions

1. How does copper electroplating of 304L affect its resistance to metal dusting?
2. How does ruthenium laser cladding of 304L stainless steel affect its resistance to metal dusting?
3. What is the influence of the variation of time on the metal dusting of copper electroplated and the ruthenium laser cladded stainless steel 304L?

1.3 Aim

The aim of this study was to determine the effect that surface modification of 304L stainless steel by copper electroplating and ruthenium laser cladding would have on the metal dusting behaviour of 304L.

1.4. Research Objectives

1. Establish the extent of metal dusting, on an uncoated 304L stainless steel sample under the specific metal dusting condition.

2. Establish if the surface modification of 304L stainless steel by copper electroplating will result in the reduction of the metal dusting of 304L stainless steel.

3. Determine if the surface modification of 304L stainless steel by laser cladding with ruthenium will result in the reduction of the metal dusting of 304L stainless steel.
4. Investigate the effect of varying time on the metal dusting of the surface modified 304L stainless steel.

1.4 Limitations

The major limitation with the project was that it was performed in a laboratory experiment setup and the results were not verified under actual plant conditions. Additionally, limited access to high resolution equipment such as the Transmission Electron Microscope (TEM) restricted the analysis process.

1.5 Project Outline

This thesis opens with Chapter 1, the introduction which outlines the project aims, objectives and the research questions.

Chapter 2, the literature survey; this chapter focuses on describing the metal dusting process, its mechanisms, metal dusting prevention methods and the laser cladding process.

Chapter 3, is the experimental methods where the materials, parameters and analysis techniques are described.

Chapter 4, is the results and discussion chapter for the reference 304L stainless steel, copper electroplated and ruthenium laser cladded samples where pre-exposure characterisation results and post-exposure characterisation results are shown and discussed.

Chapter 5 and 6, are the Conclusions and Recommendations.

1.6 References

1. J. Kelly, Heat resistant alloys, *Rolled Alloys,* bulletin 401, pp. 1-2, (2006).
2. M.I. Sahri, N.K. Othman, Z. Samsu and A.R. Daud, Investigation of high temperature corrosion behavior on 304L austenite stainless steel in corrosive environments, *AIP Conference Proceedings* 1614, pp. 152-157, (2014).
3. P.S. Vangeli, B. Ivarsson and R. Pettersson, Comparative behaviour of specialty austenitic stainless steels in high temperature environments, *Outokumpu Stainless AB: acom,* vol. 3, pp. 3-9, (2012).
4. J. Stringer, Introduction to Corrosion in fossil and alternative fuel industries, *ASM Corrosion: Environments and Industries*, vol. 13C, pp. 438–440, (2006).
5. P. Szakalos, R. Pettersson and S. Hertzman, An active corrosion mechanism for metal dusting on 304L stainless steel, *Corrosion Science*, vol. 44, pp. 2253–2270, (2002).
6. Y. Nishiyama, N. Otsuka and T. Kudo, Metal dusting behaviour of Cr-Ni steels and Ni-base alloys in a simulated syngas mixture, *Corrosion Science*, vol. 48, pp. 2064–2083, (2006).
7. H.J. Grabke, R. Krajak and E.M. Müller-Lorenz, Metal dusting of high temperature alloys, *Materials and Corrosion*, vol. 44, pp. 89–97, (1993).
8. G.M. Tanner, Metal dusting (catastrophic carburization) of a waste heat boiler tube, *Engineering Failure Analysis*, vol. 1, pp. 289-306, (1994).
9. C.M. Chun and T.A. Ramanarayanan, Metal dusting resistant alumina forming coatings for syngas production, *Corrosion Science*, vol. 51, pp. 2770–2776, (2009).
10. J.C.N. Paz and H.J. Grabke, Metal dusting, *Oxidation of Metals*, vol. 39, pp. 437–456, (1993).
11. C.M. Chun, J.D. Mumford and T.A. Ramanarayanan, Mechanisms of Metal Dusting Corrosion of Iron, *Journal of the Electrochemical Society*, vol. 149, pp. B348-B355, (2002).
12. H.J. Grabke, R. Krajak and J.C. Nava Paz, On the mechanism of catastrophic carburization: 'metal dusting', *Corrosion Science*, vol. 35, pp. 1141–1150, (1993).
13. J. Zhang, A. Schneider and G. Inden, Characterisation of the coke formed during metal dusting of iron in CO-H_2-H_2O gas mixtures, *Corrosion Science*, vol. 45, pp. 1329–1341, (2003).

14. E.M. Müller-Lorenz and H.J. Grabke, Coking by metal dusting of steels, *Materials and Corrosion*, vol. 50, pp. 614-621, (1999).
15. G.A. Slabbert, The effect of carbide-forming elements on the metal dusting rate in hydrocarbon environments, *MSc dissertation, University of the Witwatersrand,* South Africa, (2012).
16. P. Szakálos, M. Lundberg and R. Pettersson, Metal dusting on an alumina forming Ni-base alloy, *Corrosion Science*, vol. 48, pp. 1679–1695, (2006).
17. K. Natesan and Z. Zeng, Development of materials resistant to metal dusting degradation, U.S. Department of Energy: Argonne National Laboratory -*Annual Report for Calendar Year 2005,* p. 14, (2006).
18. J. Alvarez, D. Melo, O. Salas, J. Oseguera and V. López, Protective coatings against metal dusting, *Surface and Coatings Technology*, vol. 203, pp. 422–426, (2008).
19. M.D. Marekwa, Evaluation of metal dusting of Ni-Fe-Cr based alloys in laboratory environment, *MSc dissertation, University of Cape Town,* South Africa, (2006).
20. M.L. Holland and H.J. de Bruyn, Metal dusting failures in methane reforming plant, *International Journal of Pressure Vessels and Piping,* vol. 66, pp. 125-133, (1996).
21. H.J. Grabke, C.B. Bracho-Troconis and E.M. Müller-Lorenz, Metal dusting of low alloy steels, *Materials and Corrosion*, vol. 45, pp. 215-221, (1994).
22. H.J. Grabke, Thermodynamics, mechanisms and kinetics of metal dusting, *Materials and Corrosion*, vol. 49, pp. 303–308, (1998).
23. J. Klöwer, H.J. Grabke and E.M. Müller-Lorenz, Metal dusting of nickel-base alloys, *Materials and Corrosion*, vol. 49, pp. 328–329, (1998).
24. Q. Wei, E. Pippel, J. Woltersdorf and H.J. Grabke, Microprocesses of coke formation in metal dusting, *Materials and Corrosion*, vol. 50, pp. 628–633, (1999).
25. E. Pippel, J. Woltersdorf and R. Schneider, Micromechanisms of metal dusting on Fe-base and Ni-base alloys, *Materials and Corrosion*, vol. 49, pp. 309–316, (1998).
26. C.M. Chun, T.A. Ramanarayanan and J.D. Mumford, Relationship between coking and metal dusting, *Materials and Corrosion*, vol. 50, pp. 634–639, (1999).
27. P. Szakálos, Mechanisms and driving forces of metal dusting, *Materials and Corrosion*, vol. 54, pp. 752–762, (2003).

28. H.J. Grabke, D. Moszynski, E.M. Müller-Lorenz and A. Schneider, Role of sulphur in carburization, carbide formation and metal dusting of iron, *Surface and Interface Anal*ysis, vol. 34, pp. 369–374, (2002).
29. W. Brandl, G. Marginean, N. Marginean, V. Chirila and D. Utu, Prevention of metal dusting on Ni-based alloys by MCrAlY coatings, *Corrosion Science*, vol. 49, pp. 3765–3771, (2007).
30. A. Schneider and H.J. Grabke, Effect of H_2S on metal dusting of iron, *Materials and Corrosion*, vol. 54, no. 10, pp. 793–798, (2003).
31. A. Agüero, M. Gutiérrez, L. Korcakova, T.T.M. Nguyen, B. Hinnemann and S. Saadi, Metal dusting protective coatings. A literature review, *Oxidation and Metals*, vol. 76, pp. 23–42, (2011).
32. D. J. Young, J. Zhang, C. Geers and M. Schütze, Recent advances in understanding metal dusting: A review, *Materials and Corrosion*, vol. 62, pp. 7–28, (2011).
33. J. Zhang, D.M.I. Cole, and D.J. Young, Alloying with copper to reduce metal dusting of nickel, *Materials and Corrosion*, vol. 56, pp. 756–764, (2005).
34. P. Speck and D.J. Young, Influence of hafnium additions and pre-oxidation treatment on the metal dusting of Ni-Al alloys, *Oxidation and Metals*, vol. 76, pp. 287–305, (2011).
35. G.A. Slabbert, F.M.L. Mulaudzi, L.A. Cornish, M.J. Papo, V. Morudu and J. Zhang, The effect of the matrix structure on the metal dusting rate in hydrocarbon environments, *Journal of Southern African Institute of Mining and Metallurgy*, vol. 113, pp. 81–90, (2013).
36. P. Szakálos, Mechanisms of metal dusting, *PhD thesis, Royal Institute of Technology Stockholm,* Sweden, (2004).
37. J. Zhang and D.J. Young, Contributions of carbon permeation and graphite nucleation to the austenite dusting reaction: A study of model Fe-Ni-Cu alloys, Corrosion Science, vol. 56, pp. 184–193, (2012).
38. Z. Zeng and K. Natesan, Relationship of carbon crystallization to the metal-dusting mechanism of nickel, *Chemistry of Materials*, vol. 15, pp. 872-878, (2003).
39. Z. Zeng and K. Natesan, Relationship between the growth of carbon nanofilaments and metal dusting corrosion, *Chemistry of Materials*, vol. 17, pp. 3794-3801, (2005).
40. J. Zhang and D.J. Young, Effect of copper on metal dusting of austenitic stainless steels, *Corrosion Science*, vol. 49, pp. 1450–1467, (2007).

41. L. Melo-Máximo, O. Salas, D. Melo-Máximo, J. Oseguera, V.M. López-Hirata, R.D. Torres, C.M. Lepienski and R.M. de Souza, Performance of Cr oxide coatings on 304 steel against metal dusting, *Surface and Coatings Technology*, vol. 237, pp. 39-50, (2013).
42. L.M. López, O. Salasa,, L. Melo-Máximo, J. Oseguera, C.M. Lepienski, P. Soares, R.D. Torres and R.M. Souza, Structural and mechanical analysis for the optimization of PVD oxide coatings for protection against metal dusting, *Applied Surface Science*, vol. 258, pp. 7306–7313, (2012).
43. C. Geers, M. Galetz and M. Schütze, Investigation of the effect of the alloy 600 substrate for the stability of a Ni_3Sn_2 coating for metal dusting protection at 620°C, *Surface and Coatings Technology*, vol. 215, pp. 2-6, (2013).
44. S.C. Tjong and C.Y. Shih, Oxidation characteristics of some Fe-40Cr-Pd and Fe-40Cr-Ru alloys in air at 900°C, *Materials Characterization*, vol. 27, pp. 175-182, (1991).

2 Literature Review

Metal dusting is the embrittlement of a material due to increased carbon content resulting in the loss of mechanical properties and the disintegration of the material into a fine dust [1-8]. The dust is a coke deposit consisting of a combination of metal, metal carbides, metal oxides, and graphitic carbon [9-12]. Metal dusting manifests itself as uniform metal wastage in low alloyed steels and iron, or as pits in high alloyed steels [13-15]. Metal dusting thrives in environments that contain CO-H_2-CO_2-H_2O gas mixtures, with high carbon activities ($a_C > 1$), which can either be oxidizing or non-oxidizing. The temperature range at which this corrosion attack occurs is often indistinct, however, it is mostly documented as occurring between 400-800˚C[1-15]. Though, in the heat treating industry it has been witnessed in the 900-930˚C temperature range, whereas in strongly reducing, environments the metal dusting temperature has been observed to be 1100˚C [10,15-17]. Therefore, in theory [10,15-19] metal dusting could occur in any environment and at any temperature as long as the carbon activity is high enough ($a_C >> 1$).

The occurrence of metal dusting is influenced by various factors, making it difficult to predict its initiation and occurrence. However, three primary factors have been identified to greatly influence metal dusting which are: (1) the composition of the process stream, (2) operating temperature and (3) the composition of the alloy [20—21]. According to Grabke [21], the initiation of metal dusting is commonly due to changes in at least one of the following conditions:

- process operating conditions such as pressure and temperature,
- equipment repairs resulting in damaged units due to poor expertise,
- changes in the materials of construction and contamination by impurities such as chlorine or mineral salts, which may damage the protective oxide scale.

Metal dusting is complex in nature because there is no one type of condition that causes metal dusting. Industries affected by this phenomenon generally utilise different operating conditions, such as temperature, gas composition and total pressure [23].

Typical industries affected by metal dusting are: petrochemical plants, fuel refineries, nuclear plants cooled with carbon dioxide, reforming plants, heat treating industry, and in ammonia plants waste heat boilers [16,24-26]. Metal dusting also occurs in coal gasification plants, especially in processes where strongly carburizing conditions are present. Carburizing conditions are such that the CO-H_2 mixtures may react with the metallic components. These reactions may also be found in processes where organic compounds are reacting, such as butane dehydrogenation systems, hydrodealkalation systems and acetic acid cracking furnaces as well as in iron ore reduction furnaces [16,24-26].

2.1 Mechanisms of Metal Dusting

Metal dusting mechanisms of engineering alloys have been studied extensively since the 1950s, however, no universal agreement exists regarding these mechanisms, due to the varied parameters that affect the onset and occurrence of metal dusting [5,16,27]. Szakálos summarised three primary, accepted mechanisms, which are characterized as: Type I, II, III and a secondary Type IV [5,28].

2.1.1 Type I

Type I was first defined by Hochman et al. [29,30] and later extended by Grabke *et al.* [19,32]. This mechanism involves the decomposition of the metastable cementite (Fe_3C) which forms during the initiation process of metal dusting [19,26]. It is only applicable to iron and low alloyed steels, because stainless steels form more stable carbides [5,28,33].

2.1.2 Type II

According to Szakálos [28], Type II was first identified by Hultgren *et al.* [31] and developed by Pippel *et al.* [35]. This mechanism is defined as the disruption of a carbon-supersaturated matrix due to embrittlement by graphite formation [31,35]. Type II can

be identified in metal dusting of iron and low alloyed steels, nickel, binary iron-nickel alloys as well as chromium depleted austenitic stainless steels [5,28]. According to thermodynamics, both carbides and oxides are unstable in Ni and Fe-Ni austenitic steels, and only metal and graphite are identified as stable. Therefore, minute metal fragments surrounded by graphite allow for slower metal dusting kinetics [5,28,33].

2.1.3 Type III

Type III was determined by Szakálos [5,28,33], during his PhD studies. This mechanism is the selective oxidation of alloyed carbides, and was found in Ni-based alloys as well as stainless steels. It was first found in 304L stainless steel at 650˚Cexposed to H_2-CO gas mixtures. This proposed mechanism was termed active corrosion by carbon and oxygen [5,28,33]. It is supposed that oxygen plays an active role during metal dusting especially in environments that contain 2-3 vol.% and 30-50 vol.% water vapour. Type III is the most detrimental metal dusting mechanism for high alloyed materials that can form a protective chromium oxide layer which are exposed to CO containing environments, with and without water vapour. The carbon reacts with the matrix and forms carbides, these carbides are oxidized resulting in free carbon, which continues to form carbides with the metal [5,28,33].

2.1.4 Type IV

In addition to the three main metal dusting mechanisms there is the secondary Type IV mechanism. This mechanism was identified by Szakálos [5,28] and it was described as the formation of carbon nanotubes during the metal dusting process which is catalysed by the continued fragmentation of the corrosion product as more carbon was introduced to the process [5,28].

A combination of these mechanisms are usually operating, when steels undergo metal dusting, [5,28,35]. Generally accepted mechanism for Fe-Ni-Cr alloys such as 304L stainless steel is illustrated by Figure 2.1. This mechanism was defined as follows [5,7-9, 28, 36]:

a. Carbon containing gases such as carbon monoxide, carbon dioxide, hydrocarbons are decomposed on an active, catalytic alloy, into carbon atoms and others such as oxygen and hydrogen.
b. The carbon atoms are adsorbed onto the catalytically active alloy and dissolve into the alloy.
c. Once the alloy is supersaturated with carbon, graphite crystallization occurs and causes volume expansion of the alloy.
d. The volume expansion of the alloy causes disintegration of the material into corrosion product in the form of dust containing, alloy particles, oxides and graphite.

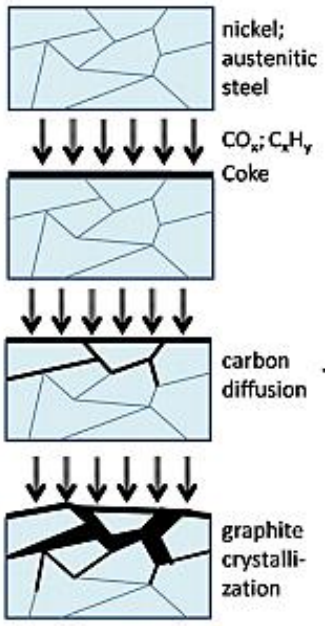


Figure 2.1: Schematic of the metal dusting mechanism for austenitic stainless steel and nickel alloys [36].

2.2 Protective methods against metal dusting

According to Zeng *et al.* [37,38] there are two primary methods of mitigating metal dusting: (a) the development of an oxide scale on the surface of the material, which results in the inhibition of carbon ingress-due to the low solubility of carbon in the oxide scale, or (b) the use of an inhibitor. Agüero *et al.* [39] have reviewed the metal

dusting phenomenon and the methods that are in existence that mitigate metal dusting. These can be changes in process conditions, surface poisoning, alloying, mechanical and chemical surface treatments, thermal treatments and coatings [39,40]. Madloch *et al.* [41] have recently suggested an additional approach of suppressing metal dusting by catalytic inhibition of the metal itself.

2.2.1 Changes in the Process Conditions

Metal dusting can be reduced or mitigated by changing process conditions or designing around the process conditions that are favourable for metal dusting [39,42,43]. Unfortunately this method induces economic penalties such as the decrease in efficiency of the process, increased energy consumption as well as decreases in the product yield of the process. It has proven to not be an efficient or effective way of mitigating metal dusting [37,39,43]. However, research groups continue to study factors that influence metal dusting such as the influence of the total pressure, the velocity of the gas in the system, and the effect of water vapour [44-50].

2.2.2 Protective Oxide Layer

Metal dusting in industrial processes is often mitigated by means of a protective oxide layer. This protective oxide scale forms as a result of an alloying element mostly Cr, forming an oxide with the oxygen in the atmosphere. The oxide layer forms on the surface of the material, forming a protective coating that separates the substrate and the gaseous environment [39-41]. In order for this oxide layer to successfully protect a material against metal dusting it should be stable, continuous, self-healing and should exhibit excellent adherence. The oxide layer lowers the amount of carbon that is transported to the matrix because oxides have lower solubility limits of carbon than the metal matrix [37,38,51]. Formation of the oxide scale is promoted by increasing Cr content, addition of minor alloying elements such as Si and/or Al, and decreasing the grain size thereby increasing the diffusion paths of Cr, to increase its diffusion rates within the material [52,53]. The oxide scale grows faster in BCC ferrite materials, due to the improved diffusion paths that are available, than in FCC austenite structures. FCC

structures have slower diffusion paths for Cr. Oxide scale growth is always guaranteed in austenitic materials when the alloy contains a high chromium content, Cr ≥ 17 wt.%, because the high Cr content allows for the formation of a continuous oxide protective layer [28,54].

The protection by oxide scale can be further re-enforced by the addition of Al and Si at quantities of 1.5 wt.% or greater, so that they can form a continuous oxide layer underneath the chromium oxide layer. Highly reactive elements such as niobium, yttrium and cerium, can be added in quantities of 0.1 wt.% or less to improve the adherence of the protective scale [53]. Yttrium, as well as the rare earth metals, are able to improve oxide formation because they segregate to the oxide-alloy interface, providing sites for oxide formation [55-57]. Carbon has a low solubility in FeO, Fe_3O_4, Cr_2O_3, Al_2O_3 and MnO, and therefore, would not permeate in dense and continuous oxide scales [58]. Unfortunately oxide layers can be destroyed by the growth of graphite, on and within the scale, which results in pits within the scale and thereafter metal dusting cannot be mitigated [2,53]. The failure of the protective oxide layer is dependent upon the temperature and chemistry of the corrosion environment and the main mechanism of failure is the spalling of the coating. Spalling occurs when the oxide layer does not heal itself as a result of the depletion of chromium in the substrate, or an oxide former in the substrate. It will also occur if the layer is not stable enough or due to internal stresses that develop during thermal cycling [59]. There are two other mechanisms of failure that have been identified: firstly failure as a result of the reduction of the oxide layer when in the presence of higher oxides such as Fe_2O_3, Cr_2O_3 and nickel spinels and secondly through the conversion of the oxide into carbides. This is more probable in environments that contain high carbon activities and this can be prevented by alloying the substrate with 1.5-2 wt.% silicon to promote the formation of a more stable oxide [53,60]. Protection against metal dusting with the use of an oxide layer has a limited protection period however, the oxide layer improves the incubation period of metal dusting. The oxide layer delays the initiation of metal dusting thereby

protecting the material for longer periods than if no protective oxide scale formed. Researchers have found that once pits form as a result of a broken oxide scale, metal dusting is unstoppable and occurs at a rapid rate [38,60]. A protective oxide scale that is adherent, continuous and self-sustaining for long periods of time is essential for the mitigation of metal dusting.

In addition the formation of a protective oxide layer is promoted by the presence of high temperatures, water vapour, a fine grained structure and surface pre-treatments such as grinding and sandblasting. The above mentioned, promoters of the chromium oxide are beneficial because they provide easy chromium diffusion paths and excess oxygen [19,21,62,63]. Water vapour is [23,61] a good inhibitor of metal dusting in austenitic stainless steels and high chromium containing alloys, because it effectively facilitates the formation of stable oxides that cannot be reduced by carbon monoxide. There have been varying opinions regarding the presence of water vapour in metal dusting environments. However, the general consensus was that it reduces metal dusting, but its protection is highly dependent upon the type of alloy and the content of the water vapour in the environment. It has been found that in laboratory experiments where there is little (1-3%) or no water vapour, and these environments tend to favour the resistance of metal dusting of nickel-base alloys [23,43]. However, research was conducted, in environments with relatively high water vapour contents (>20%), and iron based alloys such as 304 and 310 stainless steels performed better than the expensive nickel base alloys [23,43,64].

Other factors that influence the effectiveness of the oxide scale are: a high melting point and low vapour pressure of the oxide at the operating temperatures and pressures [65,66]. The oxide scale should have a thermal expansion coefficient close to that of the metal substrate, in order to limit spalling and cracking of the oxide scale. It also should have low diffusion co-efficients for metal ions and oxygen, as well as erosion resistance and resistance to impurities such as carbon deposition [23,65].

2.2.3 Surface Poisoning

Another approach to improve resistance, would be to poison the surface of the material by the addition of an inhibitor such as H_2S or PH_3 [39,54]. These inhibitors are adsorbed onto the surface of the material, breakdown to release phosphorus or sulphur which adsorb onto the surface more strongly than carbon, subsequently poisoning it [39]. The poisoning element adsorbs onto the surface, retards the carburization process by blocking the gas entry sites, thereby stopping the entire metal dusting process [32,68,69]. When this happens the carbon diffusion into the metal matrix is inhibited, preventing the subsequent metal dusting steps such as supersaturation and cementite formation. Graphite formation is stopped, which prevents the disintegration of the solid phase [32]. Sulphur unfortunately has disadvantages because its build up can result in sulphidation corrosion, but most importantly affects the subsequent processes because it reduces the process efficiency by poisoning the catalyst [39,40]. The laws governing process industries are promoting greener and more environmentally friendly processes, discouraging the use of hydrogen sulphide. Phosphorus does not affect the subsequent processes, but it is also considered to be environmentally unfriendly [39].

2.2.4 Mechanical Surface Treatments

Research has been conducted into the mechanical surface treatment of steels, specifically cold-work, and has yielded positive results in the mitigation of metal dusting. It was first identified by Grabke *et al.* [26,42,70] and later others considered different mechanical surface treatments such as sand blasting, grinding, peening and machining which yielded positive results by promoting metal dusting resistance of materials [39-43,53,63,71-76]. These processes resulted in grain refinement which in turn promoted the diffusion of chromium by providing chromium diffusion paths. This is desirable because the chromium then forms a protective oxide layer at the surface of the material thereby inhibiting carbon ingress and therefore stopping metal dusting.

2.2.5 Chemical Surface Treatments

Chemical surface treatment methods refer to chemically treating the surface prior to exposure to metal dusting conditions. This has been studied and mainly focused on

depositing a continuous and well adhering Cr_2O_3 layer. This layer has been achieved by pre-oxidation of the material prior to oxidation. In these studies was for identified that alumina (Al_2O_3) forming alloys have performed better in instances where they were pre-oxidised prior to application, than without pre-oxidation [56]. As promising as this method was for alumina forming alloys, the pre-oxidised 304 stainless steel has performed poorly in metal dusting environments [74]. Although 304 performed poorly in other studies [74], Zeng *et al.* [37,38] proposed that this method may still work on nickel-based alloys such as alloy 800. They suggested that this method would control metal dusting on alloys that have long incubation periods. Secondly, the alloys can periodically be oxidised during breaks in the operations, to cover and stop the growth of existing pits. Thereby allowing for pro-longed incubation of metal dusting attack [37,38]. Another study that was conducted showed that the addition of pre-oxidised CeO_2 and nano-dispersed CeO_2 particles on Ni_3Al coatings significantly improved the metal dusting resistance of the coatings because pre-oxidation promoted the formation of Al_2O_3 [78]. In another study it was observed that the efficiency of pre-oxidation treatments was highly dependent upon the integrity and the mechanical properties of the scale formed as a result of pre-oxidation. Therefore, defects on the oxide scale should be avoided [79]. Lin *et al.* [80] decided to pre-carburize as opposed to pre-oxidising, unfortunately this work was unsuccessful because it resulted in accelerated metal dusting in high carbon activity environments.

Some other methods that were investigated, but did not prove successful, were etching, pickling, electro-polishing and cold rolling [23,59,64]. Etching and pickling exert a negative influence because they attack grain boundaries and increase metal dusting attack. Electro-polishing and rolling result in coarse grains which slow down the diffusion of chromium [39]. The surface roughening of a material can result in the blockage of carbon diffusion paths, therefore reducing the metal dusting process [54].

2.2.6 Laser Treatments

Voisey *et al.* [81,82] investigated laser surface treatment of alloy 800H, as well as the application of laser treatment to thermal spray coatings in order to inhibit metal dusting. They found that surface laser treatment produces a refined microstructure that creates more chromium diffusion paths which promoted the formation of a dense and continuous protective layer. The laser treatment of alloy 800H resulted in adequate resistance of alloy 800H against metal dusting [81]. However, others have since found that grain refinement may not necessarily be beneficial to metal dusting mitigation particularly in environments containing higher gas velocities and high total pressures [9]. To improve the performance of coatings, laser treatment was used to apply NiCrAlY and NiCr thermal spray coatings onto two substrates, alloy 600 and 800, by eliminating inter-connected porosity in the coatings. Eliminating interconnected porosity promotes the formation of sites of carbon ingress, therefore reducing metal dusting resistance. The Ni-Cr-Al-Y coating gave the best resistance as expected because chromium, aluminium and yttrium form a protective oxide scale that remains intact. The laser treatment of both coatings resulted in improved metal dusting resistance of the coatings [82].

2.2.7 Alloying Elements

Nickel and iron and their alloys have been studied extensively due to their importance in engineering applications especially for high temperature applications [82,83]. The focus will be on the alloying elements used to alloy Fe-Ni-Cr alloys, because 304L is an Fe-Ni-Cr alloy. In such alloys, the importance of the Fe:Ni ratio has been emphasized [19,39]. Researchers agree that metal dusting resistance increases with increasing Ni and this is attributed to the low solubility of carbon in Ni [1,19, 40]. However, there is a limit to the amount of nickel that can be added to steels so that maximum protection can be achieved. Grabke *et al.* [12,26] observed that austenitic stainless steels containing more than 30 wt.% nickel experienced significant metal dusting; this is because nickel is a graphitizer and graphite plays a major role in the metal dusting of Fe-Ni-Cr alloys.

Chromium and aluminium are the most studied oxide forming alloying elements. Both these elements form stable oxides. Aluminium forms a much more thermodynamically stable oxide layer than any other oxide former. However, aluminium diffuses slowly into the metal substrates. This slows down the self-heling ability of the oxide layer [7,39,40,84]. Chromium can also be added to aluminium containing alloys to minimise the effect of the slow aluminium diffusion and to form an inter-diffusion chromium oxide barrier between the substrate and the aluminium oxide forming on the surface, improving the protection. Studies have found that an increase in aluminium or chromium in alumina and chromia forming, iron and nickel base alloys resulted in increased metal dusting resistance however, this increase in resistance in iron based alloys is subject to the type of alloy. For instance ferritic alloys are better alumina and chromium oxide formers than austenite alloys because they allow for better diffusion of aluminium and chromium relative to austenitic steels [23,85]. Therefore, ferritic steels perform much better than austenitic steels in metal dusting environments.

Other oxide formers of interest are silicon and titanium because these elements have the ability to form thermodynamically stable protective oxides. Silicon is argued to reduce the solubility of carbon in materials and promotes the formation of the protective oxide layer and thereby reducing metal dusting attack [86]. Titanium performs much better in conjunction with aluminium, because titanium promotes the formation of α-Al_2O_3, even at low temperatures [7,84]. However, titanium is a prominent carbide former that should not be added as an alloying element on its own to improve metal dusting resistance [35].

Carbide formers have not been studied extensively and the results obtained have not been consistent [87]. Carbide formers such as tungsten, molybdenum and niobium improve the incubation period by retarding the metal dusting process [39]. Due to their relatively high affinity for carbon, compared to chromium, they are prone to form carbides first, increasing the free chromium available to diffuse to the interface to form a protective chromium oxide. This protective oxide prevents the ingress of carbon,

thereby increasing the metal dusting incubation time by more than 500 hours [62,63]. However, Slabbert [35] found that these elements initially improved resistance, but more rapid and severe damage of the material occurred once the metal carbides had been oxidised. He recommended that carbide formers not be used as alloying elements in ferrous alloys, especially Fe-Ni-Cr alloys such as 304L and 316L, as a means to control metal dusting, because they result in severe degradation of ferritic alloys [35]. This rapid material degradation is caused by the carbides forming precipitates that cause defects in the oxide layer that allow for carbon ingress into the substrate and subsequent material degradation [21, 87].

Copper is another alloying element that is of interest in metal dusting, because of its resistance to carburization, metal dusting and its low solubility of carbon [87]. It has been found to enhance the metal dusting resistance of nickel base alloys and iron based alloys containing high nickel contents. Copper has a high solubility in nickel alloys and promotes the dilution of the carbon catalytic sites [87-89]. This results in the inhibition of the nucleation of graphite, and has also been observed on some austenitic stainless steels [87]. However, iron alloyed with copper showed no improvement because copper has a low solubility in ferrite and does not suppress carbon diffusion in the ferrite phase at these levels [90,91]. Alloying the austenite phase with large quantities of copper resulted in the formation of copper rich intermetallic precipitates and a significant increase in new grain boundaries that promote internal carbide formation [90,91].

Zhang and Young [90,91] studied the effect of copper additions to austenitic steels 304, 310 and alloy 800H which has a slightly higher nickel content. The 304 stainless had a higher ferrite content, therefore reducing the solubility of copper in the steel. This resulted in copper having no significant effect on the metal dusting resistance of the 304 stainless steel when 5 and 10 wt.% Cu were added to the steel. Interestingly, at 20 wt.% Cu the stainless steel, exhibited degradation [90]. It was proposed that a fully austenitic 304 stainless steel might have been more resistant to metal dusting. Additions of 5 and 10 wt.% Cu to alloy 800H and 310 stainless steel resulted in the suppression of metal

dusting for the first 500 hours of the experiments. The addition of 20 wt.% Cu to 310 stainless steel resulted in degradation of the stainless steel as a result of intermetallic copper rich precipitates, which enhanced the formation of carbide precipitates thereby increasing metal dusting potential. The alloy 800H when alloyed with 20 wt.% Cu resulted in very low amounts of surface degradation [90]. The results obtained by Zhang and Young indicate that the alloying of iron based alloys with copper for metal dusting applications is dependent upon the microstructural phase of the alloy as well as the nickel content [90,91].

2.2.8 Coatings

Protective coatings have been studied and developed to extend the lifetime and efficiency of processing units as well as increase operating temperatures of high temperature operations [66]. Such coatings are diffusion, overlay and nanotechnological coatings [7,39,40,66]. The efficiency of coatings depends on the absence of defects and pores, particularly in metal dusting environments because metal dusting initiates at these defects [7,40]. Metal dusting is believed to occur in two stages: incubation and growth. Coatings are used to lengthen the metal dusting incubation period [92]. However, this is dependent upon the integrity of the coating. Thus coatings for this application are designed for prevention of the catalytic decomposition of CO or carbon containing gas molecules and/or prevention of the absorption or dissolution of carbon into the substrate [7,40].

A review by Schütze *et al.* [66] outlines four design criteria for high temperature protective coatings, these criteria are:

1. The coating should be designed so that it can form a thermodynamically stable protective phase such as Al_2O_3, Cr_2O_3 and SiO_2 and spinel phases.
2. The protective phases should be slow growing so that the rate of depletion of the coating reserve at the interface is kept at a minimum.

3. The rate of inter-diffusion between the substrate and the coating should be very slow. An inter-diffusion barrier can be introduced or the substrate should be such that it has a low tolerance for the diffusion of the coating species.
4. The thermal expansion coefficient of the coating and the substrate should be similar to limit contraction and expansion stresses. Coating systems should be strain-tolerant.

2.2.8.1 Diffusion Coatings

Diffusion coatings are produced by adding metallic components onto a metal substrate at temperatures high enough to allow metallurgical bonding between the substrate and the coating. The atoms from the coating diffuse into the metal substrate and react therein. Such coatings are produced by means of thermochemical methods such as pack cementation, as well as chemical vapour deposition (CVD) [75,92]. According to Rosado and Schütze [93] the performance of diffusion coatings is highly dependent upon the structure and chemistry of the substrate. Therefore, for maximum protection against metal dusting different and compatible coating-substrate systems need to be developed.

The focus on diffusion coatings studies, for metal dusting control has been on alumina forming coatings, the Fe_3Al and TiAl intermetallic coatings [51]. The most popular diffusion coatings currently employed in industry especially the chemical industry as well as hot sections in power generation plants are aluminium containing diffusion coatings, mostly applied for the protection of materials against oxidation and corrosion at high temperatures [39,94]. The efficiency and longevity of these coatings can be improved by adding alloying elements such as Cr or Pt to them. In addition these alloying elements greatly increase their application operating temperatures [94]. These alumina forming coatings have been observed to inhibit metal dusting on both steels and nickel based alloys [39,94].

2.2.8.2 Overlay Coatings

Overlay coatings are such that the substrate and the coating have very little or no mixing. Mixing occurs only at the coating-substrate interface and some degree of inter-diffusion may occur [7,39,40]. Overlay coatings are usually general alloys or intermetallic materials and are not significantly affected by the composition of the substrate. These coatings are obtained by plasma spraying, electroplating, high velocity oxy fuel (HVOF) and shrouded plasma spraying (SPS). Overlay coatings can disintegrate at the coating-substrate interface because the coating is not intrinsically part of the substrate [39,40,66].

The resilience of various protective overlay coatings have been studied, but the most successful work has been on coatings for nickel-base alloys as seen in the extensive review done by Agüero [39]. Some, coatings however, have been successfully applied on ferritic alloys and have yielded good results. A γ-TiAl coating deposited by HVOF thermal spraying, was studied on both ferritic and austenitic steels, this coating performed well on ferritic steels. However, it failed when applied to austenitic steels due to the dissimilar thermal expansion coefficients of the coating and the substrate [82,93]. Thermally sprayed HVOF coatings of NiAl and Ni-50Cr have decreased the metal dusting of HP steels and 1Cr-0.5Mo steels respectively [82].

2.2.8.3 Nanotechnological Coatings

Nanotechnological coatings or nanotechnological surface modifications are the alteration of the surface of a substrate by adding a thin film on the substrate or alloying the surface of the substrate with nano-particles. The altered surface will contain nano structured materials with nano sized grains that make up a thin film or layer on the surface that is nanoscale [95]. These coatings are produced using technology such as ion implantation, RF sputtering and the sol-gel method [96-98]. Coatings of this nature can be diffusion or overlay coatings, for example ion implantation results in a diffusion coating whereas RF sputtering results in an overlay coating.

2.2.8.4 Oxide Coatings

Natsen *et al.* [99] also studied the effect of oxide coatings on nickel and iron base alloys. The coatings were produced using three different methods [99]:

1. Pre-oxidation of alloys so that an oxide layer forms on the surface.
2. Enriching the substrate surface with oxide formers such as aluminium, silicon and chromium by a pack diffusion process with an additional oxidising step, in order to form an oxide layer.
3. Thermal deposition of FeAl coatings.

The results obtained showed that the oxide scale due to pre-oxidation was ineffective in protecting the substrates against metal dusting. However, the pack diffusion deposited coatings retarded the carbon deposition process, thus preventing metal dusting [99]. The thermal sprayed coatings were found to contain pores and cracks which were assumed to be the cause of the low resistance to metal dusting of the coating [97,99].

Rosado and Schutze [85] also carried out a study on oxide coatings where oxide formers such as silicon, titanium, aluminium and chromium were deposited by means of a diffusion packing process on austenitic and ferritic steels. In their studies they found that the aluminium coatings performed the best. Silicon coatings were not protective, given that they were covered with pores and cracks and did not form a continuous protective oxide layer. A combination of silicon and aluminium resulted in improved metal dusting resistance. However, with time the aluminium coatings developed pores and became susceptible to metal dusting. Titanium performed best when combined with aluminium and assisted in the formation of the oxide layer [85].

Metal dusting studies of Al/Al_2O_3 and Cr/Cr_2O_3 magnetron sputtered coatings on HK40 were carried out by Melo et al. and Cheruvu et al. [97,100]. These deposited coatings successfully improved metal dusting resistance. However, the Al/Al_2O_3 coatings experienced cracking during exposure to carburizing environments [100]. The Cr/Cr_2O_3 coatings formed a thin coating layer which prevented the permeation of carbon to the substrate. This study also showed that, for these coatings to maintain

resistance to metal dusting, residual stresses that occurred during coating deposition, coating adherence and density, had to be optimised [97]. Magnetron sputtered Cr_2O_3 coatings deposited on 304 exhibited good resistance against metal dusting in the first 20 hours up to a temperature of 800°C. The chromium oxide protected the substrate by not catalyzing the carbon deposition process, as well as prevented the ingress of carbon. In this same study the importance of adherence and a dense oxide structure were once again emphasized [86]. More work still has to be done to improve the performance of the magnetron sputtered Cr_2O_3 and Al_2O_3 coatings [96,97,100,101].

2.2.8.5 Other Coatings

Other types of coatings such as electrodeposited Ni_3Al coatings on Fe-Ni-Cr substrates with nano-dispersed cerium oxide particles have been studied, and these coatings were found to be highly susceptible to metal dusting. The uncoated substrate materials performed much better than the coating. These studies were conducted at 650˚C and it was postulated that the coatings performed poorly because a continuous and adherent alumina oxide layer did not form at this temperature [102].

Agüero [39] has expounded on other successful coatings such as aluminide diffusion coatings on steel substrates. These aluminides are quoted as having, a life time of approximately fourteen years in service in methanol plants in a wide temperature range up to 1000°C [39]. This shows that the development of coatings for metal dusting applications is a field with great potential, but there is still a need for more research to be done so that a wider range of coatings suitable for a wider range of metal dusting environments can be developed.

2.3 Copper

Copper possesses properties which are desirable for material applications, such as exceptional corrosion resistance in non-oxidising environments, high electrical and thermal conductivity, good formability and machinability [103,104]. Copper is one of the most abundantly used commercial metals. In addition to its unique properties, copper and its alloys are so resistant, that they are deemed immune to carburization,

coking and metal dusting [101,102]. Copper has a relatively low melting temperature of 1085°C, which is above the metal dusting temperature range. Therefore, copper can still be suitable for application in metal dusting environments. Alloying ferrous and nickel alloys with copper to increase their resistance to carburization have been studied and 10 wt.% copper gave the best resistance in ferrous alloys that contained high nickel contents. However, prolonged exposure still resulted in the occurrence of metal dusting [101,105]. Additionally, Zeng et al. and Chun et al. [106,107] studied the effect of copper electroplating on steel substrates in metal dusting environments and found that copper is highly protective. However, they did not give the experimental details of the electroplating process and the parameters they used.

Additionally, copper has a low resistance to oxidation at high temperatures [104]. Unfortunately the oxides formed by copper are not self-protecting, to prevent degradation by copper oxidation. Two copper oxides are stable in Cu-O systems, these are Cu_2O and CuO which are stable at lower ($T<350^oC$) and higher temperatures ($T>350^oC$) respectively [108,109]. Mechanisms of copper oxidation at both intermediate and high temperatures have been identified: whisker formation with grain boundary diffusion and bulk diffusion. In grain boundary diffusion, the Cu^{2+} and O^{2-} ions are transported through the grain boundaries to form the CuO oxide and Cu_2O at the substrate-oxide interface [108-110].

2.4 Ruthenium

Ruthenium is a transition element and is a member of the Platinum Group Metals (PGMs) [111,112]. It is highly resistant to oxidation and corrosion, especially in air, water and acids. This metal is brittle due to its hcp structure, has high tensile strength, a high melting temperature, as well as superior heat and electrical conductivity [113,114].

Ruthenium has been identified as a potential alloying element for stainless steel alloys because it has been found to increase the corrosion resistance of these alloys in non-oxidising media [111,115-,116]. However, this improvement in corrosion properties is

mostly evident in aqueous corrosion where the protection method is by means of cathodic modification [117,118].

In the early 1990s, van Staden and Roux [119,120] studied the effect of minor ruthenium additions to high chromium steels in high temperature oxidation environments. The addition of 3 wt.% Ru to 40 wt.% Cr containing steel resulted in much faster oxidation of chromium than the bulk iron. This was credited to the fact that ruthenium supresses the diffusion of iron to the surface, but promotes that of the chromium. Therefore, the performance of the steel is improved because a protective oxide Cr_2O_3 formed [119-121]. This behaviour was observed in the temperature range of 375-600^oC. Tjong and Shihh [122] conducted similar research, but at a much higher temperature of 900^oC, which yielded disappointing results, in that both the 1 wt.% Ru and 3 wt.% Ru additions to Fe-40 wt.% Cr alloys did not improve the oxidation resistance of the alloys. However, a decrease in the rate of oxidation was observed. This research shows that ruthenium additions to Fe-Cr alloys have the potential to improve the oxidation resistance of these alloys at temperatures below 900^oC. Unfortunately, ruthenium is cited in literature as a good catalyst for carbon deposition, however, on its own without the support of SiO_2 or graphite, ruthenium is only able to catalyse amorphous, highly disordered carbon [123,124].

Ruthenium is a suitable noble metal to use in the alloying of stainless steels in South Africa to improve their corrosion properties because it is a readily available resource and it is the least expensive of the PGMs [117,122]. Although ruthenium is deemed the least expensive of the PGMs, bulk alloying with ruthenium would still result in high costs, because the cost of ruthenium is $250/ounce. Considering corrosion is a surface phenomenon, it would be best to modify the surface with minor additions of ruthenium, to reduce the alloying costs. This can be done to improve surface properties by using laser cladding, laser alloying, sputtering, but it should be noted that not all stainless steels would yield the desired result. Ruthenium is a poor crystalline carbon deposition catalyst and is often used in conjunction with graphite or SiO_2 when used as

a catalyst for graphite formation [123,124]. Ruthenium on its own produces amorphous, carbon which is advantageous because according to metal dusting mechanisms by Szákalos [28] which are generally more accepted, graphite is the main culprit for metal dusting in austenitic steels.

2.5 Electroplating

Electroplating is the process of applying a metal coating to a conducting surface most often metallic, by means of an electrochemical process [125,126]. This coating method is often done to achieve material protection, better surface appearance, imparting of special surface properties as well as improved engineering or mechanical properties to the material [127]. Electroplating is an inexpensive, reliable, efficient and highly flexible technology because it can be applied to a wide range of sizes and shapes of components [128,129]. It is a more viable method because it is a less expensive option compared to bulk alloying. Electroplating technology produces coatings that are dense, uniform and adherent which are widely used in industries such as the automobile industry, shipping, air space, machinery and defence [130-134]. The integrity of an electroplated coating is highly dependent upon the chemistry, physical nature of the substrate to be plated and the electroplating technique [135-138].

Pulse plating is used in acid copper deposition in order to improve the mechanical properties of the coating, producing a finer grain structure, reducing surface roughness, porosity and stresses. It also results in improved hardness and surface levelling. Pulse plating uses forward current for a certain period alongside a short energy reverse pulse that is interposed periodically. The current density can be varied, therefore eliminating stresses and the improved levelling and surface roughness [127].

Copper is an excellent choice as a coating which is applied by means of electroplating, because it has the ability to cover the imperfections often found in the base metal. In solutions usually used for the plating of other common metals, copper is relatively inert, it is generally a high plating efficiency metal resulting in a highly adhesive and continuous coating, even difficult to coat components [125,126]. The benefit of applying

a copper electroplating is that the coating can regulate thermal expansion irregularities such as stress, which occur between two metals with different thermal expansion coefficients by acting as thermal expansion barriers, especially if the material will be used in high temperature applications [125-127].

As such the pulse electroplating of copper has been studied and has been found to produce better quality deposits. These deposits are of superior morphology and properties, moreover this can be achieved without the addition of an additive [135-138]. The deposits tend to have a finer grain structure. This is attributed to the improved mass transfer caused by pulse plating which results in a plating mechanism that allows for continuous nuclei formation throughout the deposit allowing for progressive nucleation. However, electroplating copper onto stainless steel has proven to be a challenge as the coating adheres poorly to the steel [135-138].

2.6 Laser Cladding

Laser cladding is a technique used for the modification of the microstructure and composition of the region near the surface of the component [139,140]. The modification is achieved by fusing the substrate with the same or a different metal while maintaining minimum melting of the substrate with the aid of a laser beam [141,142]. The change in the properties occurs because of the addition of a powder mixture containing the alloying element to a molten region as a result of heat from a high power laser. This addition of the powder and heat is to achieve intermixing, that is followed by rapid solidification causing the formation of an alloyed zone that is confined near the surface of the substrate [139-142].

The laser cladding of ferrous and non-ferrous materials has been successfully applied to alter the surface properties of these materials [141-143]. Laser cladding takes advantage of rapid melting and solidification, which results in a fine grained structure and metastable phases, producing better surface properties [144,145]. A major advantage of laser cladding as a surface modification process is the flexibility of altering the surface properties of the substrate, such as improved hardness, corrosion and wear resistance,

while the properties of the bulk material are maintained. Other advantages of laser cladding are the reduced production time, enhanced thermal control as well as producing coatings with better a surface quality and denser metallurgical bonding relative to conventional coatings [146-148].

The major application of laser cladding is in the repairing and refurbishment of high value components; in industrial environments it is applied in surface cladding, repair welding as well as manufacturing processes [149]. These applications and advantages of laser cladding render this technology one of very high industrial application potential, even so industries for a time were highly reluctant to implement laser cladding due to its high investment and operating costs [141]. Another disadvantage is that laser equipment is relative expensive therefore limiting the laser applications [141,145]. However, over the years due to development and implementation of high-power diode lasers and diode pumped lasers, the costs associated with laser cladding processes have lowered, and it has become a more industrially accepted technology [150,151].

Laser cladding of ruthenium has been studied for aqueous corrosion, the deposits were found to contain an inhomogeneous distribution of ruthenium [151,152]. Ruthenium islands were observed on the laser cladded surface. Measurements by EDS resulted in lower ruthenium concentrations than expected on the surface after exposure to corrosive environments [151,152]. No further elaboration on the behaviour of ferrous alloys containing ruthenium in aqueous corrosive environments will be conducted in this study, because the mechanism of protection, in aqueous environments is different to the mechanism of protection in gaseous corrosive environments.

2.7 References

1. H.J. Grabke, R. Krajak and J.C. Nava Paz, On the mechanism of catastrophic carburization: metal dusting, *Corrosion Science*, vol. 35, pp. 1141–1150, (1993).
2. J.C.N. Paz and H.J. Grabke Metal dusting, *Oxidation of Metals*, vol. 39, pp. 437–456, (1993).
3. E. Pippel, J. Woltersdorf and R. Schneider, Micromechanisms of metal dusting on Fe-base and Ni-base alloys, *Materials and Corrosion,* vol. 49, pp. 309–316, (1998).
4. C.M. Chun, J.D. Mumford and T.A. Ramanarayanan, Mechanisms of metal dusting corrosion of iron, *Journal of the Electrochemical Society*, vol. 149, pp. B348-B355, (2002).
5. P. Szakálos, Mechanisms and driving forces of metal dusting, *Materials and Corrosion*, vol. 54, pp. 752–762, (2003).
6. Z. Zeng and K. Natesan, Relationship between the growth of carbon nanofilaments and metal dusting corrosion, *Chemistry of Materials*, vol. 17, pp. 3794-3801, (2005).
7. D.J. Young, J. Zhang, C. Geers and M. Schütze, Recent advances in understanding metal dusting: A review, *Materials and Corrosion*, vol. 62, pp. 7–28, (2011).
8. S. Madloch, A.S. Dorcheh and M.C. Galetz, Effect of pressure on metal dusting initiation on Alloy 800H and Alloy 600 in CO-rich syngas, *Oxidation and Metals*, vol. 89, pp. 483–498, (2018).
9. A. Rouaix-Vande Put, A. Fabas, S. Doublet and D. Monceau, Relevance of other parameters than carbon activity in defining the severity of a metal dusting environment, *Oxidation and Metals*, vol. 87, pp. 655–666, (2017).
10. A. Al-Meshari and J. Little, Metal dusting behaviour of furnace tube alloys, *Journal of Engineering and Applied Science*, vol. 4, pp. 68–81, (2009).
11. M. Schütze, Corrosion resistance at elevated temperatures in highly aggressive environments, *Materials and Corrosion*, vol. 63, pp. 4-18, (2007).
12. H.J. Grabke, R. Krajak, E.M. Müller-Lorenz and S. Strauß, Metal dusting of nickel-base alloys, *Corrosion Science*, vol. 47, pp. 495-504, (1996).
13. C.M. Chun and T.A. Ramanarayanan, Metal dusting resistant alumina forming coatings for syngas production, *Corrosion Science*, vol. 51, pp. 2770–2776, (2009).
14. J.Z. Albertsen, Ø. Grong, J.C. Walmsley, R.H. Mathiesen and W. Van Beek, A model for high-temperature pitting corrosion in nickel-based alloys involving internal

precipitation of carbides, oxides, and graphite, *Metallurgical and Materials Transactions A Physical Metallurgy and Material*, vol. 39 A, pp. 1258–1276, (2008).

15. S. Strauβ, R. Krajak, M. Palm and H.J. Grabke, Metal Dusting of Fe_3Al and $(Fe,Ni)_3Al$, *Oxidation of Intermetallics*, vol. 15, pp. 233-236, (1998).
16. A.I. Al-Meshari, Metal dusting of heat-resistant alloys, *PhD thesis, Cambridge University*, United Kingdom, (2008).
17. C.M. Chun and T.A. Ramanarayanan, Corrosion resistance of a high-silicon alloy in metal-dusting environments, *Oxidation and Materials*, vol. 67, pp. 215–234, (2007).
18. H.J. Grabke, Thermodynamics, mechanisms and kinetics of metal dusting, *Materials and Corrosion*, vol. 49, pp. 303–308, (1998).
19. H.J. Grabke, R. Krajak and E.M. Müller-Lorenz, Metal dusting of high temperature alloys, *Materials and Corrosion*, vol. 44, pp. 89–97, (1993).
20. Shell Services International, Damage mechanisms affecting fixed equipment in the refining industry, First Edition, Recommended Practice 571, *American Petroleum Institute*, pp. 118-121, (2003).
21. H.J. Grabke and M. Spiegel, Occurrence of metal dusting - Referring to failure cases, *Materials and Corrosion*, vol. 54, no. 10, pp. 799–804, (2003).
22. G. Lai, High temperature corrosion of engineering alloys, First Edition, *ASM International*. pp. 97–145, (2007).
23. A. Rouaix-Vande Put, K.A. Unocic, M.P. Brady and B.A. Pint, Performance of chromia- and alumina-forming Fe- and Ni-base alloys exposed to metal dusting environments: The effect of water vapor and temperature, *Corrossion Science*, vol. 92, pp. 58–68, (2015).
24. J. Alvarez, D. Melo, O. Salas, J. Oseguera and V. López, Protective coatings against metal dusting, Surface Coatings and Technology, vol. 203, pp. 422–426, (2008).
25. G.A. Slabbert, F.M.L. Mulaudzi, L.A. Cornish, M.J. Papo, V. Morudu and J. Zhang, The effect of the matrix structure on the metal dusting rate in hydrocarbon environments, *Journal of the Southern African Institute of Mining and Metallurgy*, vol. 113, pp. 81–90, (2013).
26. H.J. Grabke, Metal dusting of low and high alloy steels, *Corrosion Science*, vol. 51, pp. 711–720, (1995).
27. J.Z. Albertsen, Experimental and theoretical investigations of metal dusting corrosion in

plant exposed nickel-based alloys, *PhD thesis, Norwegian University of Science and Technology,* Norway, (2007).

28. P. Szakálos, Mechanisms of metal dusting, *PhD thesis, Royal Institute of Technology Stockholm,* Sweden, (2004).
29. R.F. Hochman and J.H. Burson, The fundamentals of metal dusting, in *Amsterdam Petroleum Institute Division of Refining, Proceedings,* vol. 46, pp. 331–334, (1966).
30. R.F. Hochman, Basic Studies of metal dusting deterioration in carbonaceous environments at elevated temperatures, *Proceedings of the 4th International Congress on Metal Corrosion*, pp. 258–263, (1972).
31. S. Pippel, E. Woltersdorf, H.J. Grabke and S. Strauβ, Microprocesses of metal dusting on iron, *Steel Research,* vol. 66, no. 7, pp. 217–221, (1996).
32. A. Schneider and H.J. Grabke, Effect of H_2S on metal dusting of iron, *Materials and Corrosion*, vol. 54, no. 10, pp. 793–798, (2003).
33. P. Szakálos, M. Lundberg and R. Pettersson, Metal dusting on an alumina forming Ni-base alloy, *Corrossion Science*, vol. 48, pp. 1679–1695, (2006).
34. S.R. Pippel, E., Woltersdorf and H.J. Grabke, Micromechanisms of Metal dusting on Fe-base and Ni-base alloys, *Materials and Corrosion*, vol. 49, pp. 309–316, (1998).
35. G.A, Slabbert, The effect of carbide-forming elements on the metal dusting rate in hydrocarbon environments, *MSc dissertation, University of the Witwatersrand,* South Africa, (2012).
36. C. Geers, Inhibition of coking and metal dusting on conventional alloys by using a Ni-Sn intermetallic coating, *PhD thesis, RWT Aachen*, Germany, (2013).
37. Z. Zeng and K. Natesan, Control of metal dusting corrosion in Ni-based alloys, *International Journal of Hydrogen Energy*, vol. 32, pp. 3640–3647, (2007).
38. Z. Zeng and K. Natesan, Initiation of metal-dusting pits and a method to mitigate metal-dusting corrosion, *Oxidation of Metals*, vol. 66, pp. 1–20, (2006).
39. A. Agüero, M. Gutiérrez, L. Korcakova, T.T.M. Nguyen, B. Hinnemann and S. Saadi, Metal dusting protective coatings. A literature review, *Oxidation of Metals*, vol. 76, pp. 23–42, (2011).
40. C. Strübbe and V. Şerban, Prevention and controlling of metal dusting, *Scientific Bulletin of the Scientific Bulletin of the Politechnica University of Timisoara, Romania,* vol. 57, pp. 7-12

(2012).

41. S. Madloch, M.C. Galetz, C. Geers and M. Schütze, Development of a metal dusting resistant functional coating by Sn and Al pack cementation, *Surface Coatings and Technology*, vol. 299, pp. 29–36, (2016).
42. P. Szakálos, R. Pettersson and S. Hertzman, An active corrosion mechanism for metal dusting on 304L stainless steel, *Corrosion Science*, vol. 44, pp. 2253–2270, (2002).
43. J.J. Hoffman, M. Lin, W.R. Watkins and S.W. Dean, Proposed metal dusting mechanism in lower temperature, high steam syngas, *NACE (2009)*, paper no. 09161, (2009).
44. A. Fabas, D. Monceaua, C. Josseb, P. Lamesle and A. Rouaix-Vande Put, Mechanism of metal dusting corrosion by pitting of a chromia-forming alloy at atmospheric pressure and low gas velocity, *Corrosion Science*, vol. 107, pp. 204–210, (2016).
45. A. Fabas, A. Rouaix-Vande Put, S. Doublet, D. Domergue, M. Salem and D. Monceaua, Metal dusting corrosion of austenitic alloys at low and high pressure with the effects of Cr, Al, Nb and Cu, *Corrosion Science,* vol. 123, pp. 310–318, (2017).
46. E.T Bentria, G.K. N'tsouaglo, C.S. Becquart, O. Bouhali, N. Mousseau and F. El-Mellouhi, The role of emerging grain boundary at iron surface, temperature and hydrogen on metal dusting initiation*, Acta Materialia,* vol. 135, pp. 340-347, (2017).
47. S. Madloch, A.S. Dorcheh and M.C. Galetz, Effect of pressure on metal dusting initiation on alloy 800H and Alloy 600 in CO-rich syngas, *Oxidation of Metals*, vol. 89, pp. 483-498, (2017).
48. H.M. Tawancy, On the degradation modes of various steel grades used in heat recovery systems: An application from the petrochemical industry, *Metallography and Microstructure Analysis*, vol. 6, pp. 36–43, (2017).
49. J. Orlikowskia, A. Jazdzewska, K. Darowicki and J. Karczewski, Metal dusting phenomena of 501 AISI furnace tubes in refinery fractional distillation unit, *Engineering Failure Analysis*, vol. 91, pp. 108–114, (2018).
50. X. Yang and Y-W Mai, J-integral for spallation of protective layer subjected to metal dusting corrosion, *Materials and Design,* vol. 119, pp. 263–269, (2017).
51. D. Röhnert, F. Phillipp, H. Reuther, T. Weber, E. Wessel and M. Schütze, Initial stages in the metal-dusting process on Alloy 800, *Oxidation of Metals*, vol. 68, pp. 271-293, (2007).

52. G.W. Han, D. Feng and B. Deng, Metal dusting and coking of alloy 803, *Corrosion Science*, vol. 46, pp. 443–452, (2004).
53. H.J. Grabke and I. Wolf, Carburization and oxidation, *Material Science and Engineering*, vol. 87, pp. 23–33, (1987).
54. G. Palasantzas, H.J. Kooij and J.T.M. DeHosson, Carbon induced metal dusting of iron-nickel-chromium alloy surfaces: A scanning auger microscopy study, *Applied Surface Science*, vol. 229, no. 1–4, pp. 190–196, (2004).
55. R.D. Kane, High Temperature Gaseous Corrosion, *ASM Handbook: Volume 13 A, Corrosion: Fundamentals, Testing and Protection,* pp. 228–235, (2006).
56. P. Speck and D.J. Young, Influence of hafnium additions and preoxidation treatment on the metal dusting of Ni-Al alloys, *Oxidation and Metals*, vol. 76, no. 3–4, pp. 287–305, (2011).
57. H.J. Grabke, G. Kurbatov and H.J. Schmutzler, Segregation beneath oxide scales, *Oxidation of Metals,* vol. 43, no. 1-2, pp. 97-114, (1995).
58. I. Wolf, H.J. Grabke and P. Schmidt, Carbon transport through oxide scales on Fe-Cr alloys, *Oxidation of Metals*, vol. 29, pp. 289–306, (1988).
59. J. Zhang, P. Speck and D.J. Young, Metal dusting of alumina-forming creep-resistant austenitic stainless steels, *Oxidation of Metals*, vol. 77, pp. 167–187, (2012).
60. H.J. Grabke, Carburization, carbide formation, metal dusting, coking, *Materials Tehnology*, vol. 36, pp. 297–305, (2002).
61. G.M. Tanner, Metal dusting (catastrophic carburization) of a waste heat boiler tube, *Engineering Failure Analysis*, vol. 1, pp. 289-306, (1994).
62. H.J. Grabke, Metal Dusting, *Materials and Corrosion*, vol. 54, no. 10, pp. 736–746, (2003).
63. S. Strauß and H.J. Grabke, Role of alloying elements in steels on metal dusting, *Materials and Corrosion*, vol. 49, pp. 321–327, (1998).
64. A. Putrevu, S.K. Varma, Z. Zeng and K. Natesan, Effect of water vapor on metal dusting behavior of ferrous alloys, *TMS Letters,* vol. 3, pp. 49–50, (2006).
65. D. Jones, Principles and prevention of corrosion, Second Edition, *Upper Saddle River: Prentice Hall*, (1996).

66. M. Schütze, M. Malessa, V. Rohr and T. Weber, Development of coatings for protection in specific high temperature environments, *Surface Coatings and Technology*, vol. 201, pp. 3872–3879, (2006).
67. M. Schütze, Mechanical properties of oxide scales, *Oxidation of Metals,* vol. 44, pp. 29-61, (1995).
68. C. Geers, M. Galetz and M. Schütze, Investigation of the effect of the alloy 600 substrate for the stability of a Ni_3Sn_2 coating for metal dusting protection at 620°C, *Surface Coatings and Technology,* vol. 215, pp. 2–6, (2013).
69. E.M. Müller-Lorenz and H.J. Grabke, Coking by metal dusting of steels, *Materials and Corrosion*, vol. 50, pp. 614-621, (1999).
70. H.J. Grabke, H.P. Martinz and E.M. Müller-Lorenz, Metal dusting resistance of high chromium alloys, *Materials and Corrosion*, vol. 54, pp. 860-863, (2003).
71. M. Maier, J.F. Norton, P.D. Frampton and C.M. Maier, Metal dusting of 9 ± 20% Cr steels in increased pressure environments at 560°C, *Materials and Corrosion,* vol. 49, pp. 330-335, (1998).
72. S. Strauss, E. Pippel and J. Woltersdorf, Effects of grain size, cold working, and surface finish on the metal-dusting resistance of steels, *Oxidation of Metals*, vol. 50, pp. 241–254, (1998).
73. J. Zhang and D.J. Young, Kinetics and mechanisms of nickel metal dusting and morphology, *Corrosion Science*, vol. 49, pp. 1496–1512, (2007).
74. C.Y. Lin, C.H. Chang and W.T. Tsai, Morphological and microstructural aspects of metal dusting on 304L stainless steel with different surface treatments, *Oxidation of Metals*, vol. 62, pp. 153–174, (2004).
75. X. Yang and S-T Tu, Stresses from oxide film imperfections during metal dusting, *Oxidation of Metals,* vol. 78, pp. 295-305, (2012).
76. M. Hänsel, C.A. Boddington and D.J. Young, Internal oxidation and carburisation of heat-resistant alloys, *Corrosion Science*, vol. 45, no. 5, pp. 967–981, (2003).
77. C.G.M. Hermse, H. Asteman, R.M. Ijzerman and D. Jakobi, The influence of surface condition on the metal dusting behavior of cast and wrought chromia forming alloys, *Materials and Corrosion*, vol. 64, pp. 856–865, (2013).

78. H. Liu and W. Chen, Effect of pre-oxidation on coke formation and metal dusting of electroplated Ni_3Al-CeO_2-based coatings in CO-H_2-H_2O, *Materials and Corrosion*, vol. 59, pp. 311–318, (2008).
79. R. Bernst, A. Schneider and M. Spiegel, Metal dusting of binary iron aluminium alloys at 600°C, *Materials and Corrosion*, vol. 57, pp. 724–728, (2006).
80. C.Y. Lin and W.T. Tsai, Nano-sized carbon filament formation during metal dusting of stainless steel, *Materials Chemistry and Phys*ics, vol. 82, pp. 929–936, (2003).
81. K.T. Voisey, Z. Liu and F.H. Stott, Inhibition of metal dusting of alloy 800H by laser surface melting, *Applied Surface Science*, vol. 252, no. 10, pp. 3658–3666, (2006).
82. K.T. Voisey, Z. Liu and F.H. Stott, Inhibition of metal dusting using thermal spray coatings and laser treatment, *Surface Coatings and Technology*, vol. 201, no. 3–4, pp. 637–648, (2006).
83. Shell Services International, Damage mechanisms affecting fixed equipment in the refining industry, First Edition, *American Petroleum Institute*, Recommended Practice, 571, pp. 118-121, (2003).
84. C. Rosado and M. Schütze, Protective behaviour of newly developed coatings against metal dusting, *Materials and Corrosion*, vol. 54, pp. 831–853, (2003).
85. C. Rosado and M. Schütze, Protective behaviour of newly developed coatings against metal dusting, *Materials and Corrosion*, vol. 54, pp. 831–853, (2003).
86. M. Schütze and H.J. Grabke, Corrosion by carbon and nitrogen: metal dusting, carburization and nitridation, First Edition, England: Abington-Cambridge, *Woodhead Publishing Limited-Abington Hall*, pp. 25-48, (2007).
87. C.H. Chang and W.T. Tsai, Carburization behavior under the pits induced by metal dusting in 304L and 347 stainless steels, *Materials Chemistry and Physics,* vol. 116, pp. 426–432, (2009).
88. J. Zhang and D.J. Young, Contributions of carbon permeation and graphite nucleation to the austenite dusting reaction: A study of model Fe-Ni-Cu alloys, *Corrosion Science*, vol. 56, pp. 184–193, (2012).
89. D.J. Young and J. Zhang, Carbon corrosion of alloys at high temperature, *Journal of the Southern African Institute of Mining and Metallurgy*, vol. 113, pp. 149–154, (2013).

90. Z. Zeng and K. Natesan, Control of metal dusting corrosion in Ni-based alloys, *International Journal of Hydrogen,* vol. 32, pp. 3640-3647, (2007).
91. J. Zhang and D.J. Young, Effect of copper on metal dusting of austenitic stainless steels, *Corrosion Science*, vol. 49, pp. 1450–1467, (2007).
92. J. Zhang, D.M.I. Cole, and D.J. Young, Alloying with copper to reduce metal dusting of nickel, *Materials and Corrosion*, vol. 56, pp. 756–764, (2005).
93. X.Yang and S.T. Tu, Stresses from oxide film imperfections during metal dusting, *Oxidation of Metals*, vol. 78, pp. 295–305, (2012).
94. N.S. Cheruvu, K.S. Chan, R. Viswanathan, N.S. Cheruvu, K.S. Chan and R. Viswanathan, Evaluation, degradation and life assessment of coatings for land based combustion turbines, *Energy Materials*, vol. 1, pp. 33-47, (2006).
95. D.R. Baer, P.E. Burrows and A.A. El-azab, Enhancing coating functionality using nanoscience and nanotechnology, *Progress in Organic Coatings*, vol. 47, pp. 342-356, (2003).
96. L. Melo-Máximo, O. Salas, D. Melo-Máximo, J. Oseguera, V.M. López-Hirata, R.D. Torres, C.M. Lepienski and R. M. de Souza, Performance of Cr oxide coatings on 304 steel against metal dusting, *Surface and Coatings Technology*, vol. 237, pp. 39-50, (2013).
97. D. Melo, D. Sigüenza, O. Salas, J. Oseguera, R. Reichelt and V.M. López, Production, characterization and evaluation of protective Cr oxide coatings against metal dusting, *Surface Coatings and Technology*, vol. 204, pp. 788–792, (2009).
98. G. Carbajal, A. Martinez-Villafańe, F.G. Gonzalez-Rodriguez and V.M. Castańo, Corrosion-resistant coatings: a nanotechnology approach, *Anti-Corrosion Methods and Materials*, vol. 48, pp. 241-244, (2001).
99. K. Natesan, Z. Zeng, W.K. Soppet and D.L. Rink, International workshop on metal dusting, *Argonne National Laboratory*, Argonne IL, USA, September (2001).
100. J. Alvarez, D. Melo, O. Salas, R. Reichelt, J. Oseguera and V. López, Role of Al oxide PVD coatings in the protection against metal dusting, *Surface Coatings and Technology*, vol. 204, pp. 779–783, (2009).
101. L.M. López, O. Salas, L. Melo-Máximo, J. Oseguera, C.M. Lepienski, P. Soares, R.D. Torres and R.M. Souza, Structural and mechanical analysis for the optimization of PVD

oxide coatings for protection against metal dusting, *Applied Surface Science*, vol. 258, pp. 7306–7313, (2012).

102. H. Liu and W. Chen, Coke formation and metal dusting of electroplated Ni_3Al-CeO_2-based coatings in CO-H_2-H_2O, *Corrosion Science*, vol. 49, pp. 4134–4153, (2007).
103. P.J. Gellings, Introduction to corrosion prevention and control, *Delft University Press,* Netherlands, pp. 72-73, (1986).
104. G.M. Fontana, Corrosion engineering, Third Edition, *McGraw Hill International*, New York, (1987).
105. Y. Nishiyama, K. Moriguchi, N. Otsuka and T. Kudo, Improving metal dusting resistance of transition-metals and Ni-Cu alloys, *Materials and Corrosion*, vol. 56, pp. 806-813, (2005).
106. C.M. Chun, S. Desai and T.A. Ramanarayanan, Metal dusting resistant copper-based materials, *ECS Transactions*, vol. 41, pp. 61-72, (2012).
107. K. Natesan and Z. Zeng, Development of materials resistant to metal dusting degradation, Final report, *Argonne National Laboratory- Nuclear Engineering Division*, pp.112-118, (2007).
108. J.H. Park and K. Natesan, Oxidation of copper and electronic transport in copper oxides, *Oxidation of Metals*, vol. 39, pp. 411–435, (1993).
109. Y. Wan, X. Wang, H. Sun, Y. Li, K. Zhang and Y. Wu, Corrosion behavior of copper at elevated temperature, *Journal of Electrochemical Science,* vol. 7, pp. 7902–7914, (2012).
110. J. Li, J.W. Mayer, E.G. Colgan, J. Li and J.W. Mayer, Oxidation and protection in copper and copper alloy thin film, *Journal of Applied Physics*, vol. 70, pp. 2820-2826, (1991).
111. J.H. Potgieter, A.M. Heyns and W. Skinner, Cathodic modification as a means of improving the corrosion resistance of alloys, *Journal of Applied Electrochemistry*, vol. 20, pp. 711–715, (1990).
112. O. Chyan, R. Chan, T. Arunagiri, R.M. Wallace, M. J. Kim and T. Hurd, Ruthenium-based copper diffusion barrier: Studied by electrochemistry, SIMS depth profiling and sheet resistance measurements, *Proceedings from the Electrochemical Society*, vol. 10, pp. 174–181, (2003).
113. Y. Schuurman, C. Mirodatos, P. Ferreira-Aparico, I. Rodriguez-Ramos and A. Guerrero-Ruiz, Bifunctional pathways in the CO_2 reforming of methane over MgO-

promoted Ru/C catalyst, *Catalysis Letter*, vol. 66, pp. 33-37, (2000)

114. M.A. Guitar, Design of new protective systems based on the intermetallic compound RuAl, *PhD thesis, University of the Saarland,* Germany, (2014).
115. P.A. Olubambi, J.H. Potgieter and L. Cornish, Corrosion behaviour of superferritic stainless steels cathodically modified with minor additions of ruthenium in sulphuric and hydrochloric acids, *Materials Design and Technology*, vol. 30, pp. 1451–1457, (2009).
116. G. Myburg , K. Varga, W.O. Barnard, P. Baradlai, L. Tomcsányi, J.H. Potgieter, C.W. Louw and M.J. Van Staden, Surface composition of Ru containing duplex stainless steel after passivation in non-oxidizing media, *Applied Surface Science*, vol. 136, pp. 29–35, (1998).
117. E.S.M. Sherif, J.H. Potgieter, J.D. Comins, L. Cornish, P.A. Olubambi and C.N. Machio, The beneficial effect of ruthenium additions on the passivation of duplex stainless steel corrosion in sodium chloride solutions, *Corrosion Science*, vol. 51, pp. 1364–1371, (2009).
118. M.B. Lekala, J.W. Van Der Merwe and S.L. Pityana, Laser surface alloying of 316L stainless steel with Ru and Ni mixtures, *International Journal of Corrosion*, vol. 2012, pp. 1–5, (2012).
119. M.J. van Staden and J.P. Roux, Surface segregation in the alloys Fe-40Cr-3Ru, Fe-40Cr-3Pt and Fe-40Cr with a 1000 Å Pt, *Applied Surface Science*, vol. 44, pp. 271–277, (1990).
120. M.J. Van Staden and J.P. Roux, The controlled oxidation of the high chromium steel alloys Fe40Cr and Fe40Cr3Ru, *Applied Surface Science*, vol. 44, pp. 263–269, (1990).
121. S.C. Tjong and C.Y. Shih, Oxidation characteristics of some Fe-40Cr-Pd and Fe-40Cr-Ru alloys in air at 900 °C, *Materials Characterisation,* vol. 182, pp. 175–182, (1991).
122. I.M. Wolff, L.E. Iorio, T. Rumpf, P.V.T. Scheers and J.H. Potgieter, Oxidation and corrosion behaviour of Fe-Cr and Fe-Cr-Al alloys with minor alloying additions, *Materials Science and Engineering A*, vol. 241, pp. 264–276, (1998).
123. R.T.K. Baker and J.J. Chludzinski Jr, Carbon deposition from catalysed decomposition of acetylene, *American Chemical Society,* vol. 90, pp. 4734-4738, (1986).
124. M.L. Mabudafhasi, R. Bodkin, C.P. Nicolaides, X. Liu, M.J. Witcomb and N.J. Coville, The ruthenium catalysed synthesis of carbon nano-structures, *Carbon,* vol. 40, pp. 2737-2742, (2002).
125. B. J. Weisenberg and L.M. Durkin, Surface engineering- copper plating, *ASM Handbook:*

Volume 5, pp. 167–176, (1994).

126. J. R. Davids, Copper and copper alloy platings, *ASM International Speciality Handbook*. pp. 127–152, (2001).
127. J. W. Dini and D. D. Snyder, Electrodeposition of copper, Fifth Edition, *John Wiley and Sons*, pp. 33–78, (2011).
128. K.L. Mittal and W. Kern, Selected bibliography on adhesion measurement of films and coatings, *Journal of Adhesion Science and Technology,* vol. 1, pp. 249-262, (1987).
129. H.H. Lou and Y. Haung, Electroplating, *Encyclopedia of Chemical Processing*, pp. 1–10, (2006).
130. L. Wei, P. Liua, K. Lina, J. Yia, C. Lioua, G. Yanga, H. Hsub and T. Tsa, Selective iron sorption for on-line reclaim of chromate electroplating solution at highly acidic condition, *Chemical Engineering Journal*, vol. 281, pp. 434–443, (2015).
131. M. Schwartz, Handbook of Deposition Technologies for Films and Coatings - Science, Technology and Applications: Deposition from aqueous solutions- an overview, Second Edition, United States , *William Andrew Publishing/Noyes,* pp. 506-606, (1994).
132. W. Blum, and G.B. Hogaboom, Principles of electroplating and electroforming, Third Edition, New York, *McGraw Hill International*, (1949).
133. R. Weil, Structure brightness and corrosion resistance of electrodeposits, *Plating*, vol. 61, p. 654, (1974).
134. W. Safranek, The properties of electrodeposited metals and alloys, Second Edition, Orlando, Florida *: American Electroplaters and Surface Finishers Society*, pp. 517-527, (1986).
135. V. Lamb, electroplating, elecroforming and electroless deposition, in Chapter 32: Techniques of Materials Prearation and handling-Part 3, *Interscience Publishers,* (1968).
136. C.C. Hu and C.M. Wu, Effects of deposition modes on the microstructure of copper deposits from an acidic sulfate bath, *Surface Coatings and Technology*, vol. 176, pp. 75–83, (2003).
137. N. Tantavichet and M.D. Pritzker, Effect of plating mode, thiourea and chloride on the morphology of copper deposits produced in acidic sulphate solutions, *Electrochimical Acta Journal*, vol. 50, pp. 1849–1861, (2005).
138. Y.Z. Wan, G.Y. Xiong, H. Liang, S. Raman, F. He and Y. Huang, Modification of

medical metals by ion implantation of copper, *Applied Surface Science,* vol. 253, pp. 9426–9429, (2007).

139. M. Riabkina-Fishman and J. Zahavi, Laser alloying and cladding for improving surface properties, *Applied Surface Science*, vol. 106, pp. 263–267, (1996).
140. A. Dorbanski, L.A. Jonda, A. Lukaszkowicz, K. Labisz and K. Klimpel, Surface modification of the alloying and PVD coatings and deposition, *Journal of Achievement in Materials Manufacturing and Engineering*, vol. 27, pp. 179–182, (2008).
141. M.F. Schneider, Laser cladding with powder- effect of machining parameters on clad properties, *Phd thesis, University of Twente, Netherlands,* (1998).
142. H. Gedda, Laser Cladding : An experimental and theoretical investigation, *Phd thesis, Luleå University of Technology,* (2004).
143. S. Toyserkani, E. Khajepour and A. Corbin, Laser cladding, First Edition, Washington D.C*, CRC Press LLC,* pp. 1-5, (2005).
144. M. Qunshuang, L. Yajiang, W. Juan and L. Kun, Investigation on cored-eutectic structure in Ni60-WC composite coatings fabricated by wide-band laser cladding, *Journal of Alloys Compounds*, vol. 645, pp. 151–157, (2015).
145. T. Orims, The application of laser cladding to mechanical component repair, renovation and regeneration, *DAAAM International Scientific Book*, pp. 587–608, (2013).
146. F. Weng, H. Yu, C. Chen, J. Liu and L. Zhao, Microstructures and properties of TiN reinforced Co-based composite coatings modi fi ed with Y_2O_3 by laser cladding on Ti-6Al-4V alloy, *Journal of Alloys and Compounds,* vol. 650, pp. 178–184, (2015).
147. J. Yang, X. Miao, X. Wang, H. Chen and F. Yang, Microstructure, magnetic properties and empirical electron theory calculations of laser cladding FeNiCr-60%WC composite coatings with Mo additions, *International Journal of Refractory Metals and Hard Materials*, vol. 54, pp. 216–222, (2015).
148. Y. Diao and K. Zhang, Applied Surface Science Microstructure and corrosion resistance of TC2 Ti alloy by laser cladding with Ti/TiC/TiB_2 powders, *Applied Surface Science*, vol. 352, pp. 163–168, (2015).
149. B. Liu and S. Dong, Stress evaluation of laser cladding coating with critically refracted longitudinal wave based on cross correlation function, *Applied Acoustics*, vol. 101, pp. 98–103, (2016).

150. D. Wang, Q. Hu, Y. Zheng, Y. Xie and X. Zeng, Optics & laser technology study on deposition rate and laser energy efficiency of laser-induction hybrid cladding, *Optical Laser Technology*, vol. 77, pp. 16–22, (2016).

151. J. van der Merwe and D. Tharandt, Corrosion resistance of laser-cladded 304L stainless steel enriched with ruthenium additions exposed to sulphuric acid and sodium chloride media, *Journal of the Southern African Institute of Mining and Metallurgy*, vol. 115, pp. 499–505, (2015).

152. J. van der Merwe, D. Tharandt and P. Masiu, Corrosion resistance of laser-cladded 304L stainless steel surfaces enriched with ruthenium additions in sulphuric acid media, *The 6th International Platinum Conference, 'Platinum–Metal for the Future-Journal of the Southern African Institute of Mining and Metallurgy*, pp. 219-224, (2014).

3 Experimental Methods

Detailed herein are the design of the experimental rig that simulated the metal dusting environment, materials, experimental methodology and the equipment that was utilised to carry out the research. The research aimed to study the behaviour of surface modified 304L stainless steel in simulated metal dusting environments for varied time periods. The surface modification was achieved by copper pulse electroplating and ruthenium laser cladding.

3.1 Materials

The proposed alloy of study was 304L, which was subjected to surface modification by means of laser cladding with ruthenium. The standard composition of 304L is given in Table 3-1, as determined by the optical emission spectroscopy (OES).

Table 3-1: Composition of the 304L stainless steel.

	Composition of the element (wt.%)							
Alloy	Ni	Fe	Cr	Mn	C	Si	S	P
304L	9.25	68.59	19.00	2.00	0.030	1.00	0.030	0.045

3.2 Surface Modification

The parameters used for the surface modification of the 304L stainless steel are shown below, both for electroplating with copper as well as laser cladding with ruthenium.

3.2.1 Copper Electroplating

Electroplating the stainless steel 304L with copper was performed using a three electrode electrochemical cell as shown in Figure 3.1. The electrochemical cell was connected to an Autolab 302 Potentiostat operated by Nova version 1.11 software. The surface pre-treatment was achieved by grinding the surface to an 80 grit SiC surface finish thereafter activated using a solution with composition 18.5 vol.% HNO_3– 7.5 vol.% HF– 74 vol.% H_2O for 12.5 minutes. Stainless steel samples of 15mm x 15mm x 4mm were plated in a conventional sulphate-sulphuric bath comprising of $CuSO_4 \cdot 5H_2O$ (67.5 g/L) and H_2SO_4 (225 g/L) in distilled water was used to electroplate the 304L

stainless steel with copper at room temperature of approximately 25°C. The pulse electrodeposition method was used to apply the copper platings. A Ag/AgCl reference electrode was used, to measure the electrochemical potential used to apply the copper plating with deposition potentials of t_{off} equalling 5 seconds and a steady potential of -0.2 V and a t_{on} of 10 seconds and a potential equal to -0.3 V at plating times of 30, 45 and 60 minutes. Thereafter, the samples were annealed at 600°C for four hours in a nitrogen atmosphere.

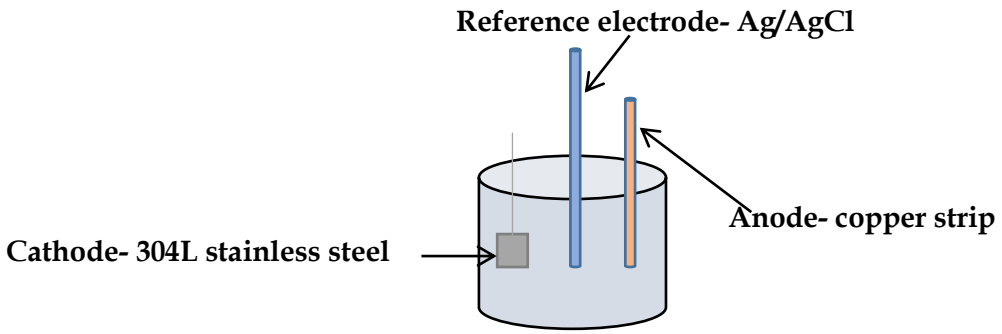


Figure 3.1: Electrochemical setup for the copper electroplating process.

The samples were subjected to a heat-quench coating adhesion test, according to ASTM B571-97. The annealed samples were heated to 250°C, in a low pressure nitrogen atmosphere for 30 minutes and quenched in liquid toluene [1].

3.2.2 Laser Cladding

The 304L substrate was laser cladded with 304L powder mixed with varied concentrations of ruthenium powder, at the National Laser Centre of Southern Africa using a 3 kW IPG Ytterbium Laser System, model YLS-3000-TR that has a wavelength of 1073 nm and a fibre target of neodium yttrium aluminium laser. The ruthenium compositions were as shown in Table 3-2, the powders were pre-mixed using a turbulent mixer where every 100 g of powder was mixed using a medium of 25 steel balls with a 5 mm diameter amounting to a total mass of 20 g at a speed of 50 rpm.

Table 3-2: Target ruthenium compositions of the powdes used for the cladding.

Sample	1	2	4	5	6
Ru (wt %)	0.00	0.50	2.00	3.50	5.00

The parameters that were used to apply the coatings were as follows:

1. Laser Power: 1.75 kW.
2. Scan Speed: 0.75 m/min.
3. Using a carrier and shielding gas of argon.
4. Mixed powder feed rate: 0.65 g/min.

3.3 Material Characterisation

The samples were subjected to metallographic preparation. They were ground with SiC of grades: 320, 600 and 1200 grit. Thereafter polished with 1 μm alumina particle solution to a mirror surface finish. The stainless steel samples were etched in 10% oxalic acid, at 10 V for 60 s and the copper electroplated sample were etched in a 110 mL ethanol, 35 mL hydrochloric acid and 7.5 g ferric chloride solution.

Material characterisation was achieved by analysing the samples with a field emission scanning electron microscope (FESEM- ΣIGMA, CARL ZEISS). The FESEM was used in conjunction with energy-dispersive x-ray spectroscopy (EDS) to determine the relative ruthenium and copper contents in the samples. The average grain size was calculated using the intercept technique as per ASTM E112-13 [2]. Where the Image J software version 1.8.0_112, was used in conjunction with the FESEM images to determine the grain size of the 304L stainless steel as-received sample and the copper electroplated samples. X-ray diffraction (XRD) analysis was also performed on the samples using XRD-D2 Phaser, to determine the phases that may have formed or precipitated as a result of the copper electroplating and laser cladding.

The coating thicknesses were measured using the FESEM and glowing discharge optical emission spectroscopy (GDO-ES: Leco GDS-850A) for the copper electroplated samples.

FESEM was used to measure the coating thickness along the cross-section of the polished coated samples, the measurements were taken at three different positions and the average of the three measurements was taken as the thickness of the thickness. The GDOES analysis was performed by placing the samples inside the glowing discharge source which is filled with argon, where the argon ions and the argon atoms collectively form plasma. Argon cations are accelerated towards the sample where they strike while displacing some atoms from the sample, therefore sputtering the atoms. The sputtered atoms diffuse into the plasma where they collide with high-energy electrons. During these collisions, energy is transferred to the sample atoms promoting them to excited energy states. When the samples return to the ground state, the atoms emit light with a characteristic wavelength spectrum resulting in their identification. The analysis was performed for 60 seconds per sample, to eliminate noise and at a sampling time of 0.01 seconds to obtain high depth resolution.

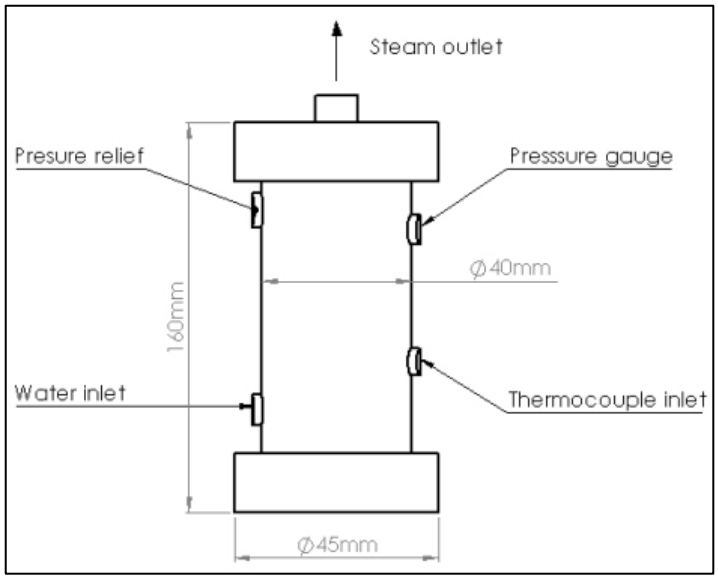
Hardness profiles were also performed on the samples using a FM-700 Vicker's Microhardness Tester at a dwell time of 10 s and varied loads. The electroplated samples were indented using a load of 10 gf and the cladded samples were indented using a 1000 gf.

3.4 Experimental Rig Design

In this work the experiments were designed such that the water vapour is approximately 20% by volume. Figure 3.3 (a), shows the experimental rig used in this work. The experimental rig was initially modelled after a single toluene, gas stream process and then developed such that a steam reactor as shown in Figure 3.3 (b) was designed.



(a)



(b)

Figure 3.2: Shows the (a) metal dusting experimental rig and (b) schematic diagram of the steam reactor.

The gas flowrates were measured using a bubble metre. The flowrate of the steam was controlled by assuming that the Law of conservation of matter was followed by the system such the density of steam at the production temperature may be used to determine the flow as follows:

- Required steam flowrate: 20 mL/min

- Steam was created at 120°C, $\rho_{steam,at\ 120℃}$ = 0.001129 g/mL

$$Q_{steam} = \dot{m}\,\rho_{steam,at\ 120℃}$$

$$\dot{m} = 20mL/\min \times 0.001129 g/mL$$

$$\dot{m} = 0.02258 \frac{g}{min}$$

Due to the Law of conservation of mass:

Mass In = Mass Out

$$\therefore Q_{water} = \frac{\dot{m}}{\rho_{water,at\ 25℃}}$$

$$= \frac{0.02258\ g/min}{1\ g/mL}$$

$$\underline{= 0.0226\ mL/min}$$

Condensation experiments were carried out to determine if the Law of Conservation of Mass was obeyed by the system and this was found to be true, the system does obey the Law.

3.4.1 Safety Precautions

- Gas detectors installed to detect carbon monoxide and hydrogen in the atmosphere in the event that there were leaks in the system.
- The lab was well ventilated by keeping the windows open as well as adding an extra fan throughout the duration of the experiments. It was however, recommended that the setup be fitted in a fume hood for better ventilation and safety of the laboratory.
- Flashback arrestors were fitted on the gas cylinders to prevent explosions.

3.5 Metal Dusting Exposure Tests

The exposure of the samples to a metal dusting simulated environment, were conducted at 525°C and 650°C and analysed after varied exposure time periods of 7 and 21 days. The temperatures used were based on studies that have been conducted before that show that metal dusting is prevalent at 525°C and 650°C[3,4]. The gas compositions used were based on work done by Hoffman [5] who emphasized that industrial processes often contain up to 40% H_2O findings that in industrial processes. However, these high steam compositions have been performed with high pressures, which was not the case in the present work. The gas mixtures used were 20 vol.% CO- 60 vol.% H_2– 20 vol.% H_2O and 25 vol.% CO- 75 vol.% H_2, with a flow rate of 100 mL/min. These gases produced different carbon activities and oxygen partial pressures as shown in Table 3-3. The 0,679 atm carbon activity was used as a result of the work conducted by De Bruyn et al. [3], where they found that metal dusting occurred in steam reformers at 650°C and activities as low as 0.28 atm. A ceramic (Al_2O_3) tube of 53 mm internal diameter was used to contain the samples during exposure with a length of 910 mm.

Table 3-3: Carbon activity and partial pressure of each exposure gas and temperature.

20 vol.% CO- 60 vol.% H_2– 20 vol.% H_2O	**20 vol.% CO- 60 vol.% H_2– 20 vol.% H_2O**	**25 vol.% CO- 75 vol.% H_2**
a_C = 0.679 atm	a_C = 0.512 atm	a_C = 35 atm
P_{O_2} = 1.559 x 10^{-27} atm	P_{O_2} = 5.118 x 10^{-24} atm	P_{O_2} = 1.012 x 10^{-24} atm
525°C	650°C	650°C

All the samples i.e. untreated 304L stainless steel of 15 mm x 15 mm x 4 mm dimension, the copper elecotroplated samples and the laser cladded samples, were exposed to all three conditions shown in Table 3-3.

The samples were ground to 500 SiC surface finish prior to exposure and 304L stainless steel was used as a reference. The furnace was purged with N_2 gas for approximately 45 minutes while the furnace was heated up to the temperature at which the experiments

were carried out at atmospheric pressure, in two gas mixtures of composition, which flowed at a rate of 100 mL/min for a maximum of 21 days, at a temperature of 650^{o}C. The gas mixture upon entering the furnace was at a total pressure of 1 atm and exited at 1 atm. The mass of the samples was measured prior to exposure

3.6 Post Exposure Characterisation

Post exposure the samples were removed from the furnace where their mass was measured before and after cleaning in an ultrasonic bath with acetone for 10 minutes. Thereafter surface morphology and corrosion debris were studied using optical microscope (Olympus BX-510), FESEM in conjunction with EDS, Raman Spectroscopy, and low angle grazing-incidence x-ray diffraction (GIXRD). Raman spectroscopy was conducted using a Horiba Jobina-Yvon, LabRAM HR Raman Spectrometer, with an excitation wavelength of 514.5 nm with the use of an Argon ion laser, and three different areas were analysed on each sample. Grazing incidence x-ray diffraction (GIXRD) was conducted with a Bruker-D8 using Kα-Cu radiation as the internal reference, in the 20-90° θ range, using an incident angle range 2° and a scan rate of 2°/min.

3.7 References

1. ASTM B571-97(2013), Standard practice for qualitative adhesion testing of metallic coatings, *ASTM International*, West Conshohocken, PA, (2010).
2. ASTM E112-13, Standard test methods for determining average grain size, West Conshohocken, PA, *ASTM International*, pp. 12-14, (2013).
3. H.J. Grabke, Corrosion by carbon and nitrogen: metal dusting, carburisation and nitridation, *European Federation of Corrosion (EFC) Series*, pp. 1-24, (2007).
4. H.J. de Bruyn, E.H. Edwin and S. Brendryen, Apparent influence of steam on metal dusting corrosion, *NACE (2001)*, paper no. 01383, (2001).
5. J.J. Hoffman, M. Lin, W. R. Watkins and S.W. Dean, Proposed metal dusting mechanism in lower temperature, high steam syngas, *NACE (2009)*, paper no. 09161, (2009).

4 Results and Discussion

The results section describes the characterisation of the materials in the as-received condition as well as the characterisation of the materials post exposure to an environment favourable for metal dusting. The materials that will be discussed in this section are:

1. The 304L stainless steel control samples.
2. The 304L stainless steel samples electroplated with copper for 30, 45 and 60 minutes.
3. The ruthenium laser cladded 304L stainless steel samples with ruthenium concentrations of 0 wt.% (cladded with 304L stainless steel powder only), 0.5 wt.%, 2 wt.% and 5 wt.%.

4.2 Stainless steel 304L

4.2.1 Pre-exposure material characterisation

The microstructure and material characterisation of the as-received 304L stainless steel were determined using the FESEM, the Vicker's microhardness and phase analysis obtained from XRD analysis.

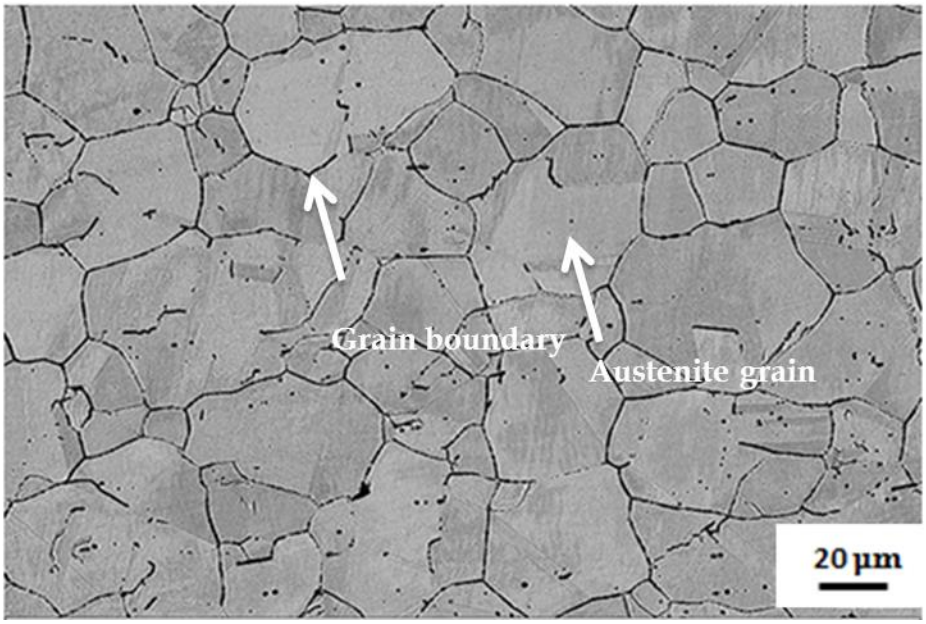


Figure 4.1: FESEM-BSE micrograph of the austenitic 304L grains before exposure.

The microstructure analysis showed that the substrate was made up of relatively large austenitic grains, in the order of 40 µm as shown in Figure 4.1, determined according to ASTM E112-13 [1].

The XRD analysis of the 304L stainless steel, revealed an FCC crystal structure and the typical 304L stainless steel peaks at 2θ of 51.5°, 60° and 90° as shown in Figure 4.2 [2].

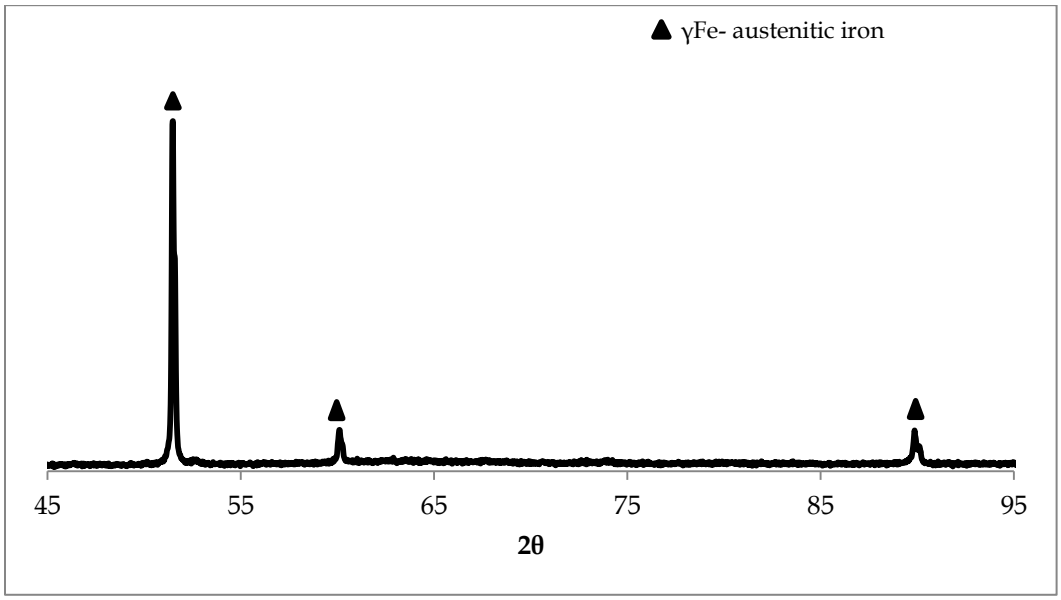


Figure 4.2: Typical XRD spectrum of the 304L stainless steel.

A hardness profile of 10 indents was performed across the cross-section of the rolled 304L stainless steel plate. The average Vicker's hardness value obtained was 179 HV with a standard deviation of 2 HV [3]. The characterisation of the as-received stainless steel confirmed that it was 304L stainless steel.

4.2.2 Post exposure results

This section shows the post exposure analysis results obtained from the 304L stainless steel samples that were exposed to a metal dusting environment.

4.2.2.1 Mass change results

Post exposure samples were weighed to determine the mass change so as to determine a rough estimate of the rate of metal dusting [4-6]. This method of corrosion rate

determination, as a penetration rate, is not accurate as metal dusting generally manifests itself as pitting and not uniform attack.

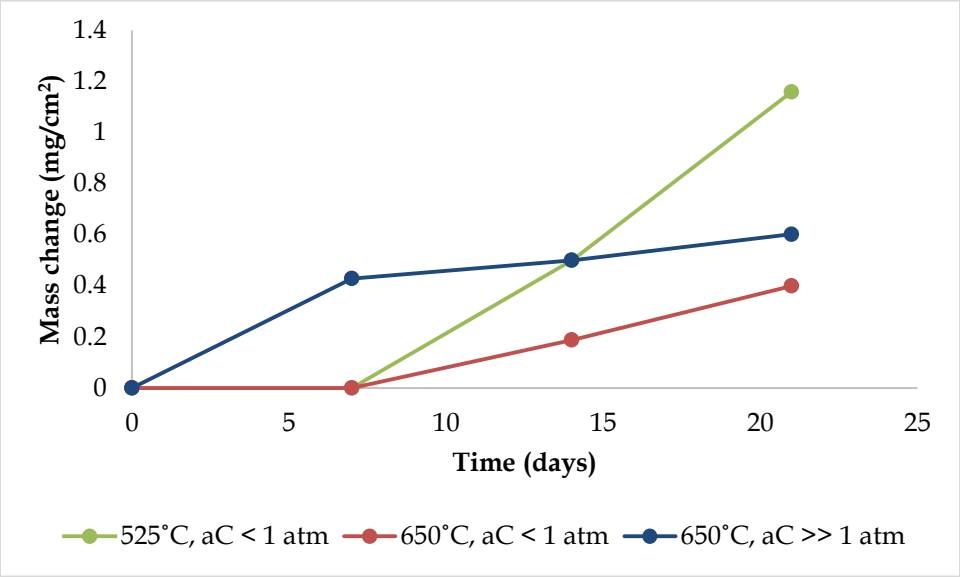


Figure 4.3: Mass change after exposure to an environment favourable for metal dusting for 504 hours at 525°C (a_C < 1 atm), 650°C (a_C < 1 atm) and 650°C (a_C >> 1 atm).

(a) Mass change results after exposure to a_C < 1 atm

In the first seven days of exposure the sample exposed to 525°C with a carbon activity of 0.657 atm and an oxygen partial pressure of 1.559×10^{-27} atm, underwent a mass loss. However, after further exposure the sample gained relatively large amounts of mass such that after 21 days the mass gained was approximately 1.2 mg/cm² as shown in Figure 4.3.

The sample exposed at 650°Cwhere the carbon activity and oxygen partial pressure were 0.512 atm and 5.118×10^{-24} atm respectively, also initially experienced mass loss during the first seven days of exposure. Thereafter the sample gained mass, however, the mass gain was not as high as the sample exposed at 525°C. Figure 4.3 shows the mass gained after 21 days of exposure was approximately 0.40 mg/cm².

These results imply that the 304L samples may possibly have undergone general mass loss as a result of the initiation of corrosion attack, which slowed down with further exposure to the gaseous environment, resulting in mass gain. The mass gain is

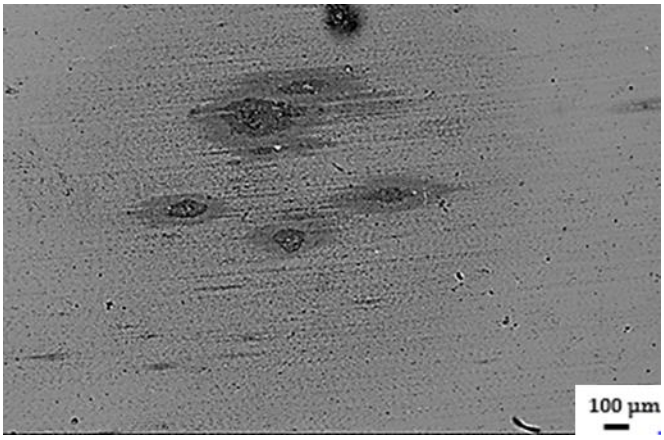
suspected to be a result of the growth of an oxide scale on the sample as seen by other researchers [7-9].

(b) Mass change results after exposure to a_C >> 1 atm

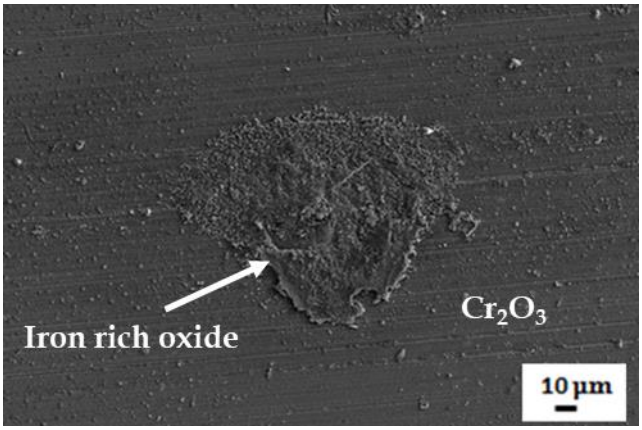
In contrast the sample exposed at 650°C containing a carbon activity of 35 atm with an oxygen partial pressure of 1.012×10^{-24} atm, gained mass regardless of the exposure period. However, the mass gain gradually slowed down such that after 21 days the mass gained was only 0.602 mg/cm^2 as shown in Figure 4.3. The continued growth in mass may be attributed to self-healing of the oxide layer and/or the formation of coke as suggested by other researchers [10-12].

(c) Exposure to low carbon activity (a_C < 1 atm)

FESEM investigation of the 304L stainless steel sample exposed for seven days in a metal dusting environment, with a carbon activity less than unity and a total pressure of 1 atm, at 525°C, revealed that the sample formed a protective oxide layer and islands suspected to be corrosion that has formed on pits as shown in Figure 4.4. However, further analysis showed that the islands were a porous oxide that is rich in iron and high contents of silicon and manganese were detected by EDS. The presence of this porous oxide implies that it is highly probable that the stainless steel has undergone some attack as the porous oxide has low resistance to carbon ingress and that its formation was a result of the surface attempting to self-heal [13-15]. This has been the case in other studies [8,16] where the material underwent attack due to a break in the oxide layer and in an attempt to self-heal the substrate was unable to form a stable and protective oxide. In this work the same mechanism is suspected and it is postulated that the substrate was unable to self-heal due to the FCC structure of the 304L stainless steel which affords chromium a low diffusion coefficient, coupled with the relatively low exposure temperature therefore promoting the formation of a rich iron oxide which is not protective [17,18]. The formation of the porous oxide and the possible attack of the substrate underneath it explain the initial mass loss during the first seven days of exposure.



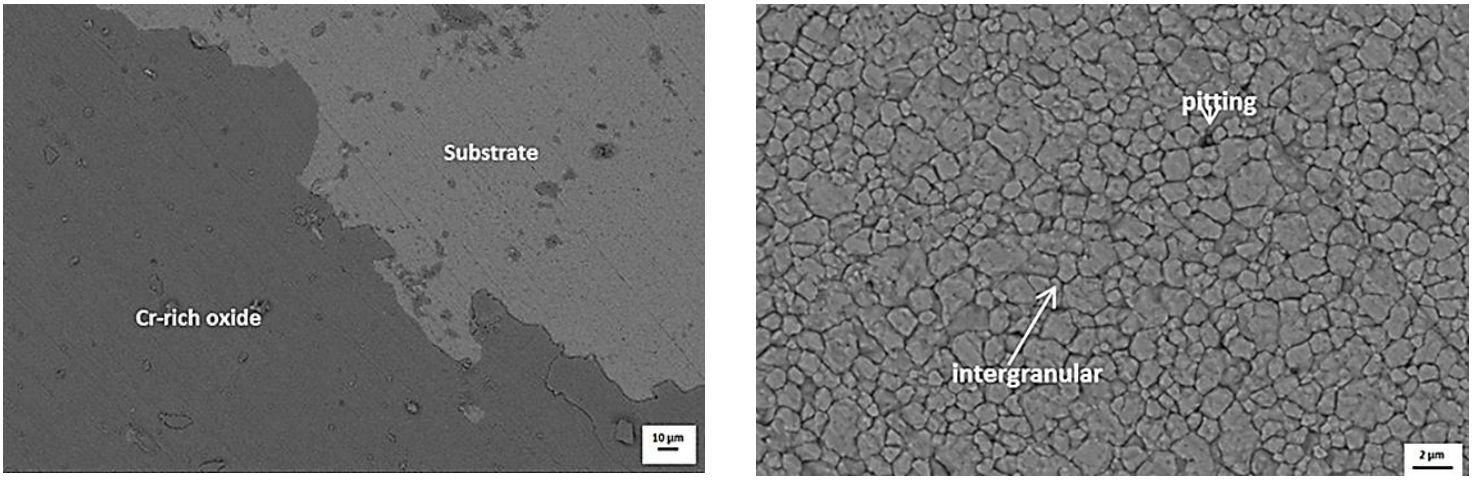
(a)



(b)

Figure 4.4: (a) FESEM-BSE and (b) FESEM-SE micrographs of 304L exposed for seven days at 525°C showing minor amounts of corrosion debris, carbon deposits and areas of attack (a) low magnification and (b) high magnification.

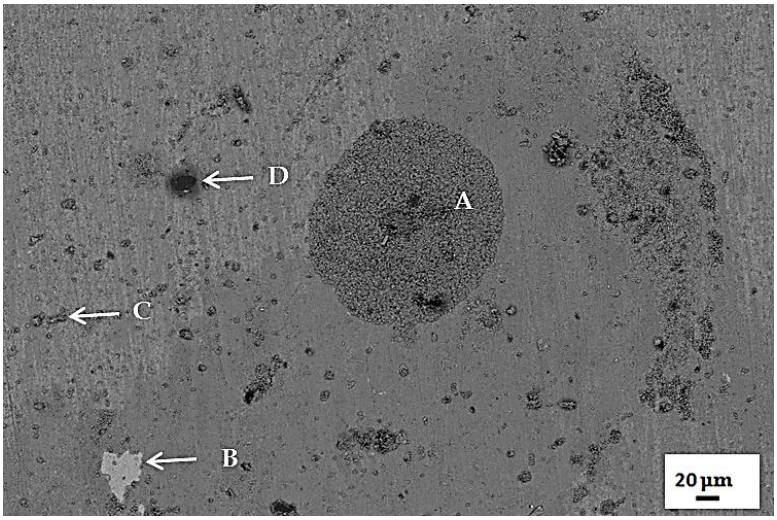
In contrast the sample exposed to 650°C for seven days, underwent damage of the protective oxide that formed during exposure and it was observed that surface intergranular attack was initiating, as the grain boundaries can be distinctly seen. It also appeared as if pitting was initiating on the exposed substrate as shown in Figure 4.5 (b). The protective oxide failed by spalling and this is suspected to be a result of the instability of the oxide layer that formed. This would be the case because the oxygen partial pressure of 5.118×10^{-24} atm is conducive to the formation of chromites rather than the stable oxide. Secondly, the stresses induced during the growth of the oxide layer coupled with the exposure to a relatively high temperature resulting in faster kinetics, would cause the spalling of the oxide [19,20]. The faster kinetics effect is two-fold, (i) it hastens the growth of the oxide layer which results in greater stress build up and (ii) the increased dissolution of the grain boundaries which reduced the available diffusion paths hence the absence of the iron rich porous oxide [21-23].



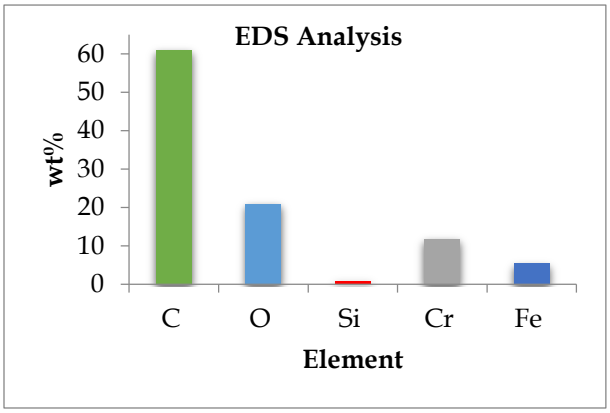
(a) **(b)**

Figure 4.5: FESEM-BSE micrographs of 304L exposed for seven days at 650°C showing minor amounts of corrosion debris, spalled oxide layer and the substrate at (a) low magnification and (b) high magnification.

The surface appearance of 304L after 21 days of exposure at 525°C is shown in Figure 4.6 (a), where no significant coke deposition was observed. However, a porous oxide rich in manganese and silicon formed depicted by (A) in Figure 4.6 (a), with chromium content lower than the nominal amount in 304L was present. Additionally, on the porous oxide, EDS analysis revealed a prominent carbon peak, implying the presence of carbon within the porous oxide as shown in Figure 4.6 (b). The presence of the carbon on the porous oxide, implies that the oxide deposit was not protective therefore leading to catalysed carbon deposition. This is also suggested by others who have encountered such porous deposits [8] where similar deposits with a nodular shape were observed that contained iron, chromium and oxygen. Melo-Maximo et al. [8] found this type of oxide on 304L after just 2.5 hours of exposure which continued to grow, in a CH_4-H_2-O_2(residual) environment at 800°C. They concluded that it was mainly Fe_2O_3 and it was porous therefore catalysing carbon deposition and mass gain. Additionally, the partial pressure of oxygen 1.559 x 10^{-27} atm is suitable for the formation of hematite [9,24]. It is therefore postulated that the continued growth of this oxide caused the consistent increase in mass gain.



(a)

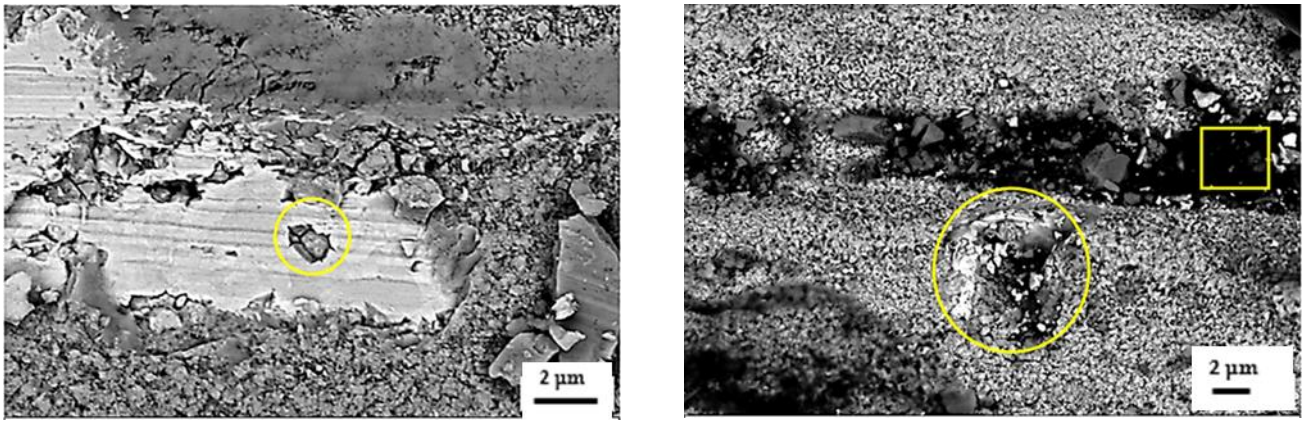


(b)

Figure 4.6: (a) FESEM-BSE image of the 304L surface after 21 days of exposure at 525°C where (A) shows the porous iron rich oxide formed, (B) where the oxide spalled revealing the substrate, (C) oxide particles rich in chromium and (D) carbon rich particles deposited on the 304L stainless steel sample. (b) EDS analysis of the porous iron rich oxide (A).

There are areas at which the oxide had spalled as shown by (B) in Figure 4.6 (a), revealing the 304L substrate. There were small particles at (C) on the surface, which were found to be oxides rich in chromium with minor amounts of manganese and silicon. Where (D), shows the carbon rich deposits identified on the surface of the 304L stainless steel sample post exposure.

Exposure at 650°C for 21 days, revealed that an oxide layer formed but had spalled, revealing the substrate as shown in Figure 4.7 (a) and (b). The substrate underwent pitting attack and intergranular degradation inside the pits as shown in Figure 4.7 (a). In addition, there were areas on which carbon was deposited and these are characterised by the black deposits shown in Figure 4.7 (b). Additionally, a porous oxide rich in iron also covered the surface. This oxide is similar to the one observed on the sample exposed at 525°C- hematite. The growth of the oxide could have been a consequence of the relatively low partial pressure of oxygen that is conducive for hematite formation compounded by the depletion of the chromium oxide at the surface. Chromium has relatively low diffusion co-efficient of approximately 1.3x10-16 m^2/s at 650°C and even lower in 525°C in austenitic 304L stainless steel which is mostly attributed to its FCC structure and as a result diffuses at relatively low rates, resulting in limited replenishment of the chromium at the surface [25]. The depletion of the chromium therefore allowed for the rich iron oxide formation [26,27]. The growth of this oxide, the continued spalling of the oxide and the possible attack below the oxide of the fresh substrate offset each other resulting in a slower growth of the oxide, hence the lower mass gain after 21 days of exposure.



(a) **(b)**

Figure 4.7: FESEM-BSE images of 304L surface after 21 days at 650°C showing (a) spalled oxide and the grain boundary etching inside the pit and (b) iron rich porous oxide, revealed substrate and carbon.

The Raman spectra shown in Figure 4.8 are the analyses of the corrosion products produced after 21 days of exposure to a metal dusting favourable environment. For statistical significance three areas were sampled on each sample. Raman analysis revealed similar corrosion products for the 304L stainless steel samples exposed at both 525 and 650°C with minor differences.

Analysis of the sample exposed at 525°C, revealed the presence of hematite (Fe_2O_3), a chromite solid solution $(Fe,Ni)Cr_2O_4$, and Cr_2O_3. The chromite solid solution $(Fe,Ni)Cr_2O_4$ is shown by the broad peak that ranges from 600-740 cm^{-1}, which is the region where the rim of the chromite grain that peaks at 642 cm^{-1} and the core of the chromite grain which peaks at 692 cm^{-1} [28-30]. In the same wave number region lies the Cr_2O_3 peak at approximately 646-648 cm^{-1} [31,32].

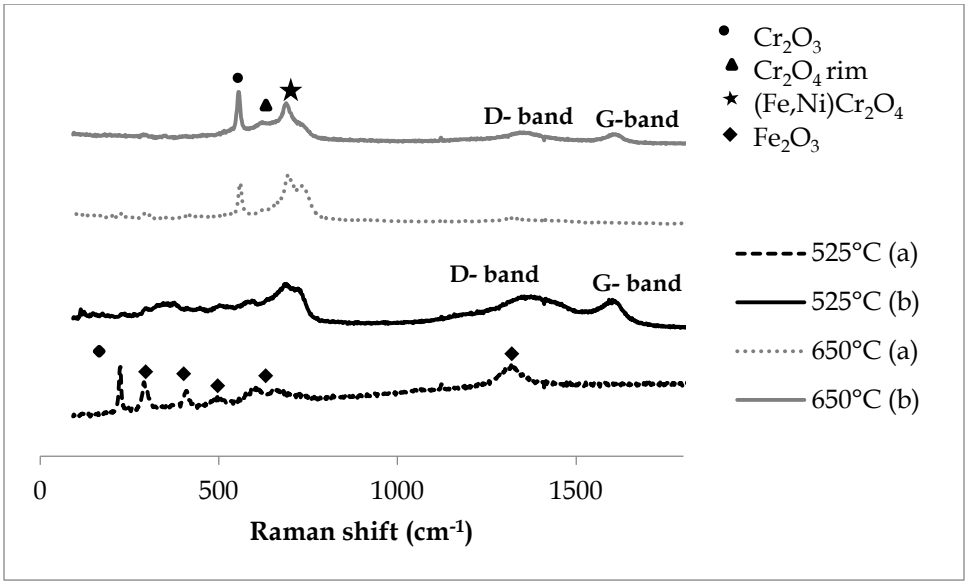


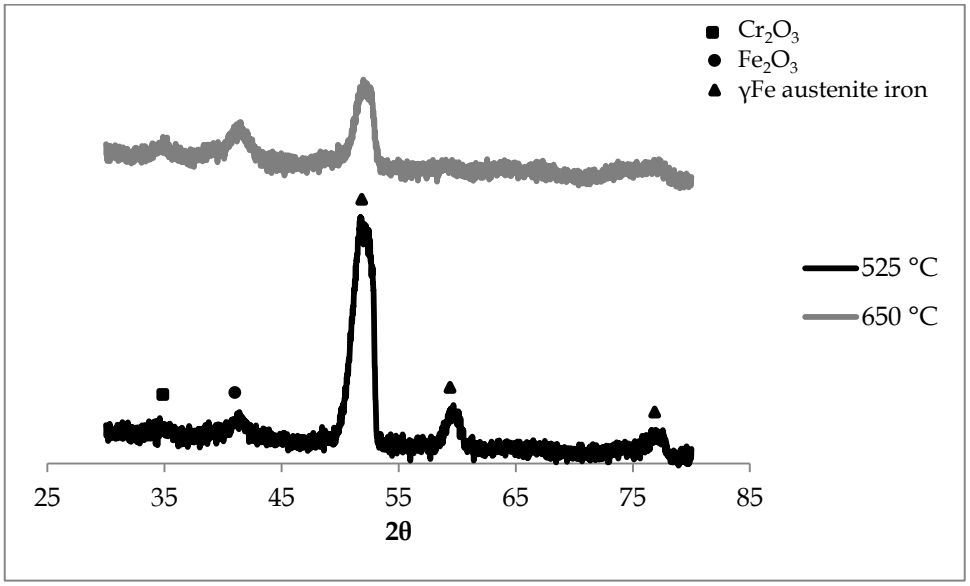
Figure 4.8: Raman spectra obtained on the surface of the 304L stainless steel samples exposed at both 525°C and 650°C.

Whereas the Raman spectra obtained for the sample exposed to 650°C, for 21 days, showed that the sample had formed Cr_2O_3 at a Raman wavelength of approximately 558 cm^{-1}, as well as variations of the $(Fe,Ni)Cr_2O_4$ solid solution depicted by peak 698 cm^{-1} with the chromite rim found at 642 cm^{-1}. Hematite was also observed however, at

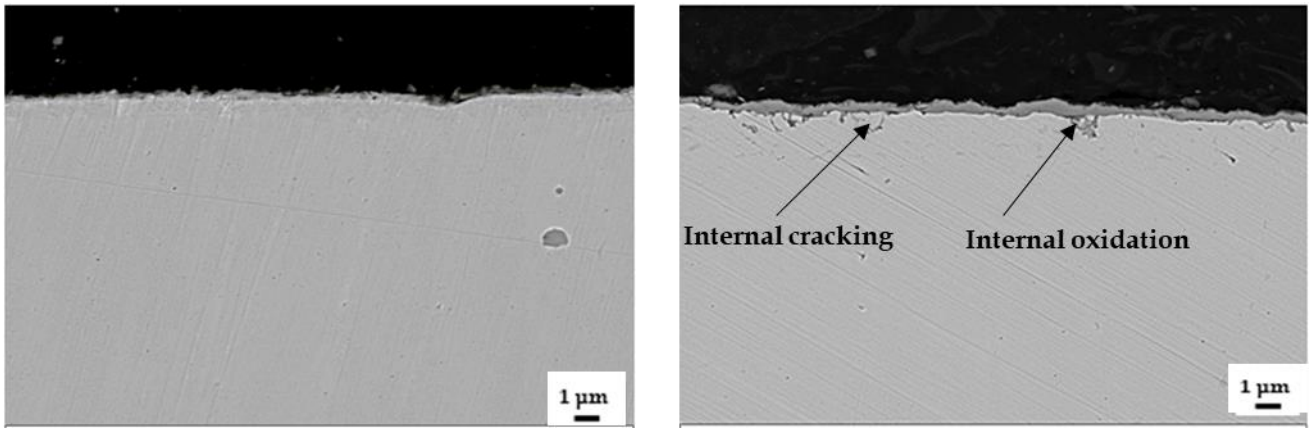
very low intensities and this is evident in the slightly increased intensity of the D-band peak (1300 cm^{-1}) where the Fe_2O_3 can be found.

The D and G peaks of carbon on the exposed samples were observed under Raman spectroscopy for the samples exposed at both 525 and 650°C. This result is in agreement with the findings of Ferrari who found the D (1350 cm^{-1}) and G (1682 cm^{-1}) bands representative of disordered and ordered carbon respectively. The G band is often synonymous with graphite [33-35]. The nature of the carbon observed on this sample was crystalline and graphitic in nature, although the D and G bands had shifted to higher wave numbers, due to the thin bandwidths and the I_D/I_G ratio in the range of 1.01 and 1.05 that was obtained for both exposure temperatures, it can be concluded that the carbon was graphitic in nature. Increasing exposure temperature from 525 to 650°C decreased from 1.05 to 1.01 suggesting increased propensity for metal dusting. It has to be noted that the D band for the sample exposed at 525°C, is exaggerated by the Fe_2O_3 peak, often observed between 1300 and 1400 cm^{-1}, therefore widening the peak.

Figure 4.9 (a), shows the results obtained from GIXRD analysis, which indicate the presence of austenitic iron at the surface as well as the presence of the chromium oxide and hematite, at the shallow peaks at 35.6 and 41° respectively. An interesting observation is that the oxide layer can be seen, though thin on the cross-section FESEM as shown in Figure 4.9 (b) and (c). In contrast the cross-section of the sample exposed at 650°C in Figure 4.9 (c), shows the presence of an oxide on the surface which is relatively thick compared to the sample exposed at 525°C. Internal oxidation can also be observed on this sample, as well as minor cracking highlighted in Figure 4.9 (c). This implies that the environment was conducive to self-healing of the oxide layer, but supporting the preferential oxidation of the iron and not the chromium.



(a)



(b) (c)

Figure 4.9: GIXRD spectra obtained on the surface of the 304L stainless steel samples exposed at both 525°C and 650°C. FESEM-BSE cross-section images of the 304L sample exposed at (a) 525°C and (b) 650˚C.

4.2.2.2 Exposure to high carbon activity (aC >> 1 atm)

The 304L stainless steel sample was exposed to an environment containing a carbon activity of 30 atm at 650°C. Analysis of the stainless steel 304L after seven days of exposure showed that the material did not undergo any mass gain or loss. However, it did form a porous oxide rich in iron. This oxide did spall in some areas while it appears to have self-healed as shown in Figure 4.10. The spalling of the oxide is suspected to be a result of the stresses that occurred as a result of the growth of the oxide, whereas the self-healing is caused by the high affinity of iron to oxygen [21-24]. The oxide failed in

some areas revealing the substrate, however no significant damage was observed on the exposed substrate. No pitting and any grain boundary damage was observed on the exposed surface. There were deposits of carbon debris on the surface of the exposed 304L stainless steel.

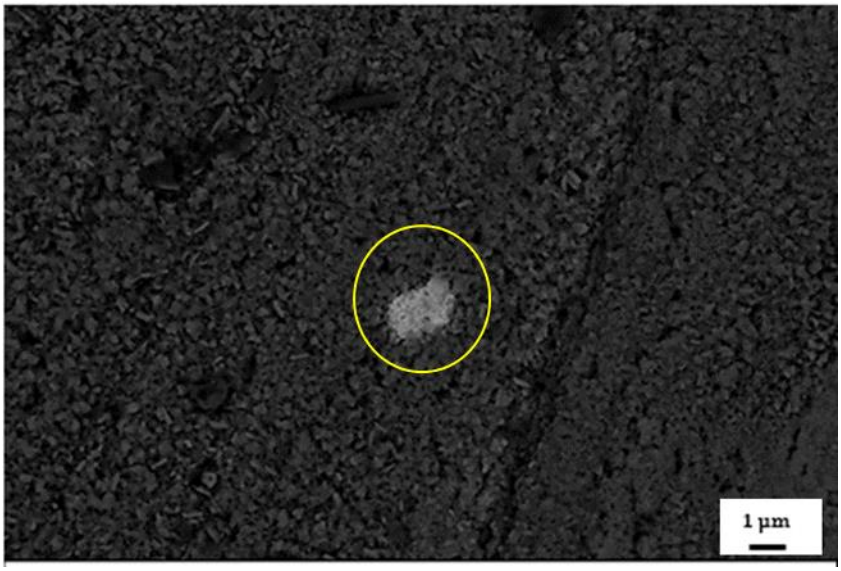


Figure 4.10: FESEM-BSE micrographs of 304L exposed for seven days at 650°C showing the spalled oxide, the substrate and iron rich porous oxide.

A similar result was observed on the sample exposed for 21 days, where the porous, iron rich oxide had formed on the exposed surface as shown in Figure 4.11. However, it was observed that larger areas of the substrate were exposed to the gaseous environment. The obtained results are suspected to be a result of the oxygen partial pressure of 1.012×10^{-24} atm, which is conducive for the formation of chromites and hematite rather than the stable and protective chromium oxide. It does not prevent gas ingress to the substrate and can be easily broken down by growth stresses, thereby leaving the substrate vulnerable to attack. Additionally, exposure to high temperatures may be accelerating the degradation of the oxide formed, therefore depleting the chromium much faster and thereby enhancing the iron rich oxide formation on the surface [26,27].

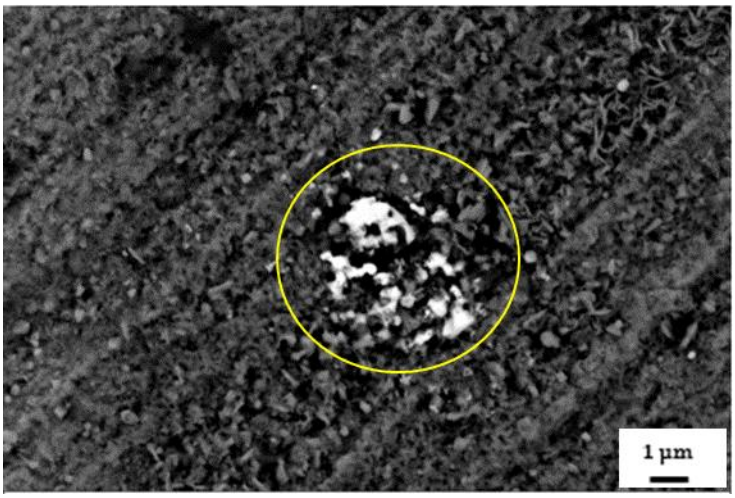
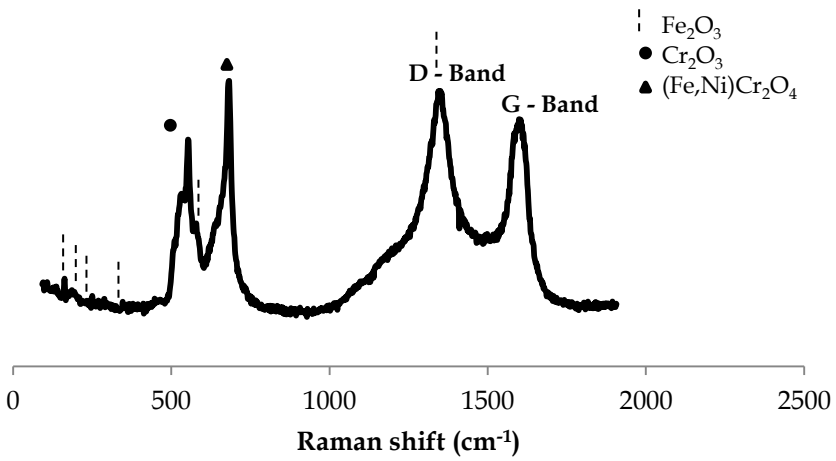
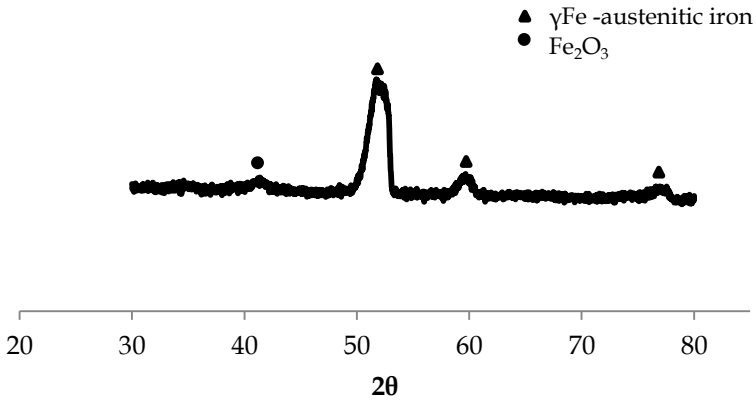


Figure 4.11: FESEM-BSE micrographs of 304L exposed for 21 days at 650°C showing the spalled oxide, the substrate and iron rich porous oxide.

In addition the Raman spectra indicates the presence of the hematite, depicted by the presence of the shallow peaks seen at approximately 200, 220,350, 430 cm^{-1}, including the intense peak at ≈ 1300 cm^{-1}. Chromium oxide (Cr_2O_3) at ≈ 683 cm^{-1} and the iron chromite ($FeCr_2O_4$) at ≈ 554 cm^{-1} were evident on the Raman spectra as well. Moreover the Raman spectra revealed the presence of graphitic carbon shown by the sharp G band in Figure 4.12 (a). Figure 4.12 (a) shows the presence of both the D and the G band with the D band with a higher intensity. The high intensity of the D band is attributable to the hematite peak found at 1300 cm^{-1}. The GIXRD analysis, also indicated the presence of hematite shown by the shallow peak at 41°, and the presence of the austenitic iron at the surface. The presence of the austenitic phase implies that the oxide layer that formed was relatively thin and this is evident in the cross-section image in Figure 4.13.



(a)



(b)

Figure 4.12: (a) Raman and (b) GIXRD spectra obtained on the surface of the 304L stainless steel samples exposed at 650ºC for 21 days.

The cross section results show that the sample underwent some attack as valleys indicative of pits can be observed on the cross-section, but no internal sub-surface oxidation or carburisation can be observed. However, it was observed that cracking initiated at the sub-surface.

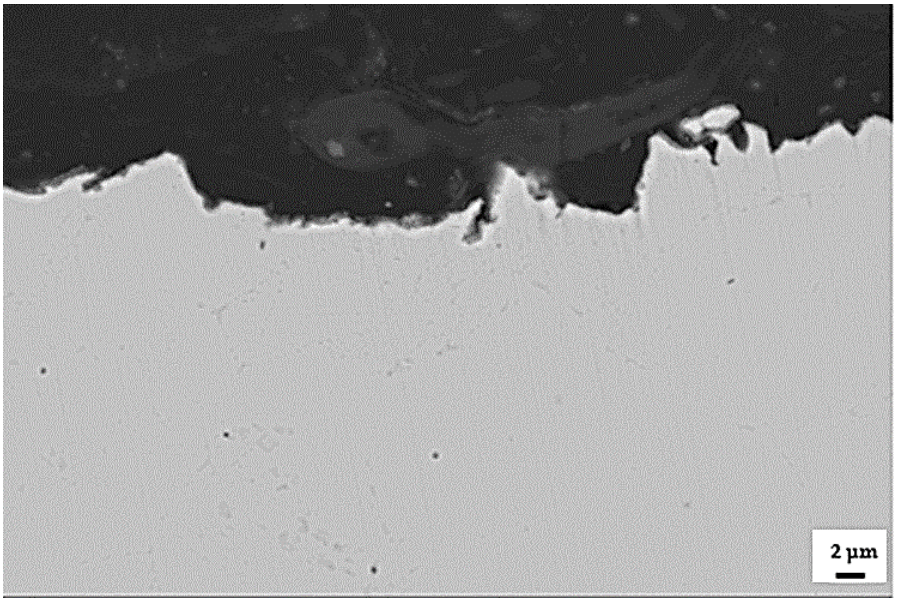


Figure 4.13: FESEM-BSE cross-section image of the 304L sample exposed at 650°C.

4.2.3 Discussion

The generally accepted metal dusting mechanism of 304L stainless steel occurs via the dissolution of carbon into the 304L stainless steel substrate, which results in supersaturation of the steel with carbon. The supersaturation leads to the formation of graphite that causes volume expansion that subsequently causes material disintegration [36-38]. In this work 304L stainless steel was studied in both $a_C < 1$ atm and $a_C >> 1$ atm environments that were conducive for metal dusting to understand the behaviour of the 304L relative to 304L stainless steel that has been treated.

The exposed 304L stainless steel gained mass at most of the exposure times and temperatures implying that the alloy formed an oxide layer, as identified using Raman analysis. No significant metal dusting attack was observed on the surface of the exposed 304L stainless steel samples. However, the samples formed a protective oxide layer as well as a porous rich oxide suspected to be hematite (Fe_2O_3) layer. The iron rich layer is suspected to have buried the attack as it was very prominent particularly after 21 days of exposure. The protective oxide layer was expected due to the relatively high chromium content in 304L stainless steel of approximately 18 wt.%. It was postulated

that the hematite forms on the surface of the samples in the regions and areas after the oxide layer that formed initially cracked and spalled. This cracking and spalling of the oxide would be a result of stresses caused by oxide formation, and could lead to the depletion of chromium, therefore resulting in an unstable oxide. This subsequently resulted in the exposure of the 304L stainless steel substrate to the corrosive gaseous environment as was the case in Figure 4.6, 4.7 and 4.10. The depletion of the chromium was due to the slow diffusion of the chromium in the FCC material. The exposed 304L stainless steel therefore attempts to self-heal by forming an oxide, however the oxide formed is rich in iron because of the high affinity that iron has to oxygen and it is the most abundant species available to react with the oxygen. Consequently, promoting the formation of the iron rich oxide similarly to what was found by Hänsel et al. [7].

Additionally, it was suspected that the relatively low partial pressure of oxygen promoted the formation of hematite identified by Raman Spectroscopy, rather than that of the chromium oxide layer [24]. The porosity of the hematite allowed for easy diffusion of the corrosive gases to the surface of the substrate allowing for the catalysis of the deposition of carbon, hence the presence of the graphitic carbon [39,40].However, there was attack that was initiating on the surface of the samples.

The GIXRD and Raman spectra results obtained for this alloy are found to be consistent with Szakálos [20,24] work where he simulated on ThermoCalc 304L stainless steel exposed to a high temperature environment. Szakálos [20,24] found the dominant phases when the PO_2 of oxygen is between 10^{-24} and 10^{-28} atm, are the austenite and $FeCr_2O_4$ phases Szakalos deduced that the 304L was prone to metal dusting which is caused by the simultaneous attack of carbon and oxygen, hence the materials formed an oxide layer that failed and metal dusting was in the initiation stage [20,24]. The presence of the graphitic carbon also emphasise that metal dusting was initiating on the samples.

4.2.4 Chapter Summary

A study was conducted to determine the behaviour of 304L stainless in a metal dusting favourable environment at two different temperatures 525°C and 650°C, for two different time periods 7 and 21 days, at two low carbon activities, 0.679 and 0.512 atm, and high a carbon activity of 35 atm. The study showed that exposure of the 304L stainless steel resulted in the formation of a mixture of the protective oxide and the porous iron rich oxide, which was adherent and continuous, resulting in minimum attack after seven days of exposure. However, after longer exposures the oxide layer failed and the substrate was exposed to form mostly porous iron rich oxide, which catalysed carbon deposition. This implied that metal dusting had initiated and was continuing. The formation of this, rich iron oxide is evidence of the self-healing nature of the oxide to form a hematite oxide layer. Although self-healing did occur, the presence of the graphitic carbon is evidence for the initiation of metal dusting.

4.2.5 References

1. ASTM E112-13, Standard test methods for determining average grain size, ASTM International, West Conshohocken, PA, (2013).
2. S. Gosh, M.K. Kumar and V. Kain, High temperature oxidation behaviour of AISI 304L stainless steel- effect of surface working operations, *Applied Surface Science*, vol. 264, pp. 312-319, (2013).
3. *http://nickelinstitute.org/~/Media/Files/TechnicalLiterature/Types304and304LStainlessSteelsforLowTemperatureService_328_.pdf#page=* (Last accessed, 15 October 2018)
   Low Temperature Data Sheet of Stainless Steels, Types 304 and 304L
4. J.C Nava Paz and H.J. Grabke, Metal dusting, *Oxidation of Metals*, vol. 39, pp. 437-456, (1993).
5. C.H. Toh, P.R. Munroe and D.J. Munroe, Metal dusting of Fe-Cr and Fe-Cr-Ni alloys under cyclic conditions, *Oxidation of Metals*, vol. 58, pp. 1-21, (2002).
6. A. Rouaix-Vande Put, K.A. Unocic, M.P. Brady, and B.A. Pint, Performance of chromia- and alumina-forming Fe- and Ni-base alloys exposed to metal dusting environments: The effect of water vapor and temperature, *Corrossion Science*, vol. 92, pp. 58–68, (2015).
7. M. Hänsel, C.A. Boddington and D.J. Young, Internal oxidation and carburisation of heat-resistant alloys, *Corrosion Science*, vol. 45, pp. 967-981, (2003).
8. J. Zhang, K. Boddington and D.J. Young, Oxidation, carburisation and metal dusting of 304 stainless steel in CO-CO_2 and CO-H_2-H_2O gas mixtures, *Corrosion Science*, vol. 50, pp. 3107–3115, (2008).
9. K. Natesan and Z. Zeng, Development of materials resistant to metal dusting degradation, Final report, *Nuclear Engineering Division, Argonne National Laboratory*, pp. 39-44, (2007).
10. E.M. Müller-Lorenz and H.J. Grabke, Coking by metal dusting of steels, *Materials and Corrosion*, vol. 50, pp. 614-621, (1999).
11. S. Strauß, R. Krajak and H.J. Grabke, Coking by metal dusting of nickel-base alloys, *Materials and Corrosion*, vol. 50, pp. 622-627, (1999).
12. C-Y. Lin and W-T Tsai, Nano-sized carbon filament formation during metal dusting of stainless steel, *Materials Chemistry and Physics*, vol. 82, pp. 929–936, (2003).
13. M.L. Holland and H.J. De Bruyn, Metal dusting failures in methane reforming plant, *International Journal of Pressure Vessels and Piping*, vol. 66, pp. 125-123, (1996).

14. G. Palasantzas, H.J. Kooij and J.Th.M. DeHosson, Carbon induced metal dusting of iron–nickel–chromium alloy surfaces: a scanning auger microscopy study, *Applied Surface Science,* vol. 229, pp. 190–196, (2004).
15. D. Melo-Máximo, A.E. Murillo, O. Salas, L. Melo-Máximo and J. Oseguera, Behavior of uncoated and coated pure Fe in metal dusting conditions, *Surface and Coatings Technology,* vol. 308, pp. 10-18, (2016).
16. L. Melo-Máximo, O. Salas, D. Melo-Máximo, J. Oseguera, V.M. López-Hirata, R.D. Torres, C.M. Lepienski and R.M. de Souza, Performance of Cr oxide coatings on 304 steel against metal dusting, *Surface & Coatings Technology*, vol. 237, pp. 39–50, (2013).
17. H.J. Grabke, Corrosion by carbonaceous gases, carburization and metal dusting, and methods of prevention, (*Reprinted from proceedings of High-Temperature Corrosion and Protection 2000), Materials at High Temperatures*, vol. 17, pp. 483-487, (2000).
18. H.J. Grabke, Carburization, carbide formation, metal dusting, coking, *Materiali in Tehnologije,* vol. 36, pp. 297-305, (2002).
19. P. Szakálos, Mechanisms and driving forces of metal dusting, *Materials and Corrosion*, vol. 54, pp. 752–762, (2003).
20. P. Szakálos, R. Pettersson, and S. Hertzman, An active corrosion mechanism for metal dusting on 304L stainless steel, *Corrosion Science*, vol. 44, pp. 2253–2270, (2002).
21. J.Z. Albertsen, Experimental and theoretical investigations of metal dusting corrosion in plant exposed nickel-based alloys, *PhD thesis, Norwegian University of Science and Technology, Norway,* (2007).
22. H.J. Grabke and I. Wolf, Carburization and oxidation, *Material Science and Engineering*, vol. 87, pp. 23–33, (1987).
23. I. Wolf, H. J. Grabke, and P. Schmidt, Carbon transport through oxide scales on Fe-Cr alloys, *Oxidation of Metals*, vol. 29, no. 3–4, pp. 289–306, (1988).
24. P. Szakálos, Mechanisms of metal dusting, *PhD thesis, Royal Institute of Technology Stockholm*, Sweden, (2004).
25. I. Kaur, W. Gus and L. Kozma, Handbook of grain and interphase boundary diffusion data, *Stuttgart, Ziegler press*, (1989).

26. M. Szkodo, and G. Gajowiec, Studies of the mechanism of metal dusting of 10CrMo9-10 steel after 10 years of operation in the semi-regenerative catalytic reformer, *Corrosion Science*, vol. 102, pp. 279–290, (2016).
27. C.G.M. Hermse, H. Asteman, R.M. IJzerman and D. Jakobi, The influence of surface condition on the metal dusting behavior of cast and wrought chromia forming alloys, *Materials and Corrosion*, vol. 64, pp. 856-865, (2013).
28. H. Singh, D. Puri, S. Prakash and R. Maiti, Characterization of oxide scales to evaluate high temperature oxidation behavior of Ni-20Cr coated superalloys, *Materials Science and Engineering A*, vol. 464, pp. 110–116, (2007).
29. A. Wang, K.E. Kuebler, B.L. Jolliff and L.A. Haskinj, Raman spectroscopy of Fe-Ti-Cr-oxides, case study: Martian meteorite EETA79001, *American Mineralogist*, vol. 89, pp. 665–680, (2004).
30. B. J. Reddy and R. L. Frost, Spectroscopic characterization of chromite from the Moa-Baracoa Ophiolitic Massif, Cuba, *Spectrochimica Acta Part A*, vol. 61, pp. 1721–1728, (2005).
31. M. Da Cunha Belo, M. Walls, N. E. Hakiki, J. Corset, E. Picquenard, G. Sagon and D. Nöel, Composition, structure and properties of the oxide films formed on the stainless steel 316L in a primary type PWR environment. *Corrosion Science*, vol. 40, pp. 447–463, (1998).
32. D. Renusch, B. Veal, K. Natesan and M. Grimsditch. Transient oxidation in Fe-Cr-Ni alloys: A Raman-scattering study, *Oxidation of Metals*, vol. 46, pp. 365–381, (1996).
33. Z. Zeng, K. Natesan and V.A. Maroni, Investigation of metal-dusting mechanism in Fe-base alloys using Raman spectroscopy, X-ray diffraction and electron microscopy, *Oxidation of Metals*, vol. 58, pp. 147-170, (2002).
34. Z. Zeng and K. Natesan, Relationship between the growth of carbon nano-filaments and metal dusting corrosion, *Journal of the American Chemical Society*, vol. 17, pp. 3794-3801, (2002).
35. A.C. Ferrari and J. Robertson, Interpretation of Raman spectra of disordered and amorphous carbon, *Physical Review B*, vol. 61, pp. 14095-14107, (2000).
36. C.M. Chun, J.D. Mumford, and T.A. Ramanarayanan, Mechanisms of metal dusting corrosion of iron, *Journal of the Electrochemical Society*, vol. 149, pp. B348-B355, (2002).
37. D.J. Young, J. Zhang, C. Geers, and M. Schütze, Recent advances in understanding metal dusting: A review, *Materials and Corrosion*, vol. 62, pp. 7–28, (2011).

38. A. Rouaix-Vande Put, A. Fabas, S. Doublet and D. Monceau, Relevance of other parameters than carbon activity in defining the severity of a metal dusting environment, *Oxidation and Metals*, vol. 87, pp. 655–666, (2017).
39. D.J. Young and J. Zhang, Metal dusting: catastrophic corrosion by carbon, *The Journal of The Minerals, Metals & Materials Society*, vol. 64, pp. 1461-14969, (2012).
40. X. Sun, H.T. Ma, L.Z. Yang, M. Sanchez-Pasten, D. Craig Penner, Y.S. Li and Q. Yang, Metal dusting, carburization and diamond deposition on Fe–Cr alloys in CH_4–H_2 plasma atmospheres, *Corrosion Science*, vol. 98, pp. 619–625 , (2015).

4.3 Copper Electroplating

This section outlines the characterisation of samples before and after exposure to the metal dusting environment.

4.3.1 Pre-exposure material characterisation

4.4.1.1 Microstructural Analysis

The visual analysis of the annealed samples as shown in Figure 4.14 showed that these samples have relatively large grains, implying that the annealing process resulted in grain recrystallization which yielded large continuous gains. These grains are regular shaped and distinct. The average grain size in the un-etched condition, observed for the annealed samples is 5.95, 7.56 and 7.70 µm respectively. From this it is observed that increasing the plating time resulted in increased grain size.

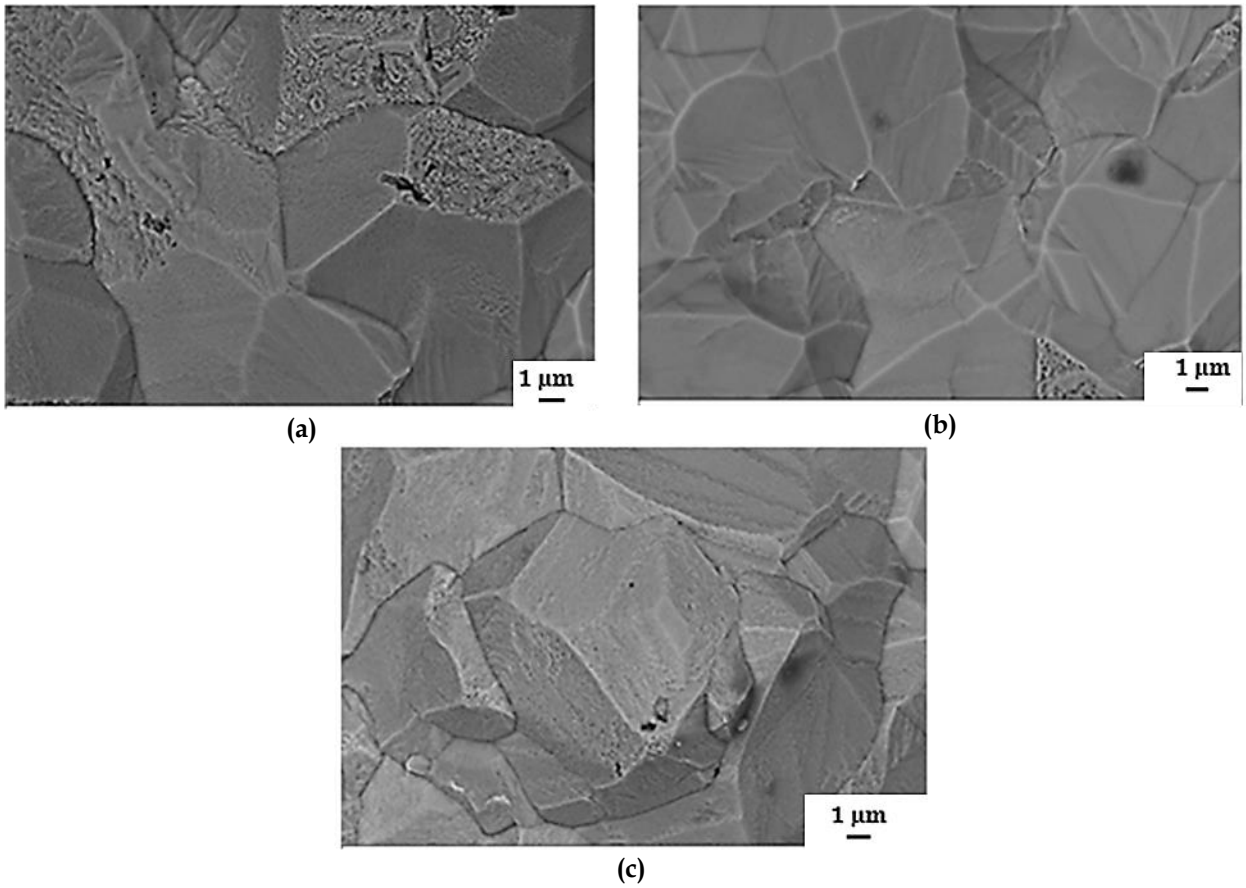


Figure 4.14: FESEM-BSE images of annealed and un-etched samples copper electroplated for (a) 30 minutes, (b) 45 minutes and (c) 60 minutes.

The annealed copper electroplated samples in the etched condition, exhibited relatively small grains (200 nm or less), in the nano-meter size range, Figure 4.15. These nano sized grains have been reported in other pulse plating studies as well, and it was associated with a smooth surface finish with good adhesion and low porosity, which has been the case for the coatings in this study as confirmed by the cross-section analysis shown in Figure 4.16 and the adhesion tests performed and shown in Figure 4.17 [1-5]. The nano-crystallites appear to increase in size with increasing plating time.

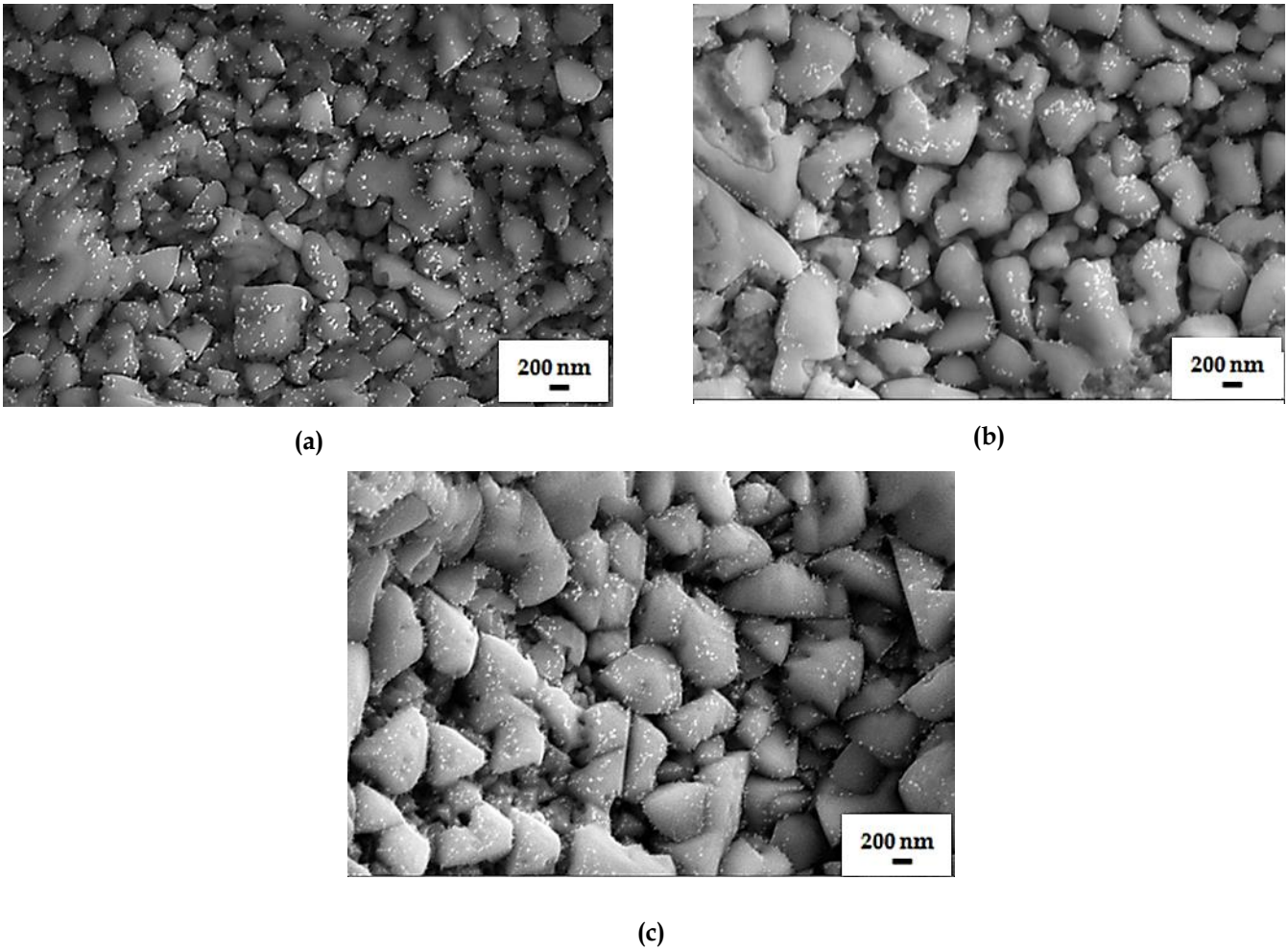


Figure 4.15: FESEM-BSE images of annealed and etched samples copper electroplated for: (a) 30 minutes, (b) 45 minutes, and (c) 60 minutes.

The copper plated coating covered the entire 304L stainless steel substrate homogeneously. Coating thickness was characterised using FESEM by measuring the coating along the cross-section of the coated samples as shown in Figure 4.16 and

GDOES, where the GDOES depth profiling indicated that the coatings were 24.86, 30.36 and 50 µm thick. Both techniques showed that the copper electroplated samples adhered well to the substrate forming an overlay coating where the coating-substrate interface was clearly visible. Such that there was no significant mixing between the substrate and the coating, a clear transition could be seen at the coating-substrate interface, and the copper did not diffuse into the substrate as is evidenced by the relatively sharp decline of the copper graph in Figure 4.18. The copper concentration has a relatively steep slope just before it is entirely not present and the copper concentration was recorded as 0wt% for all the plated samples.

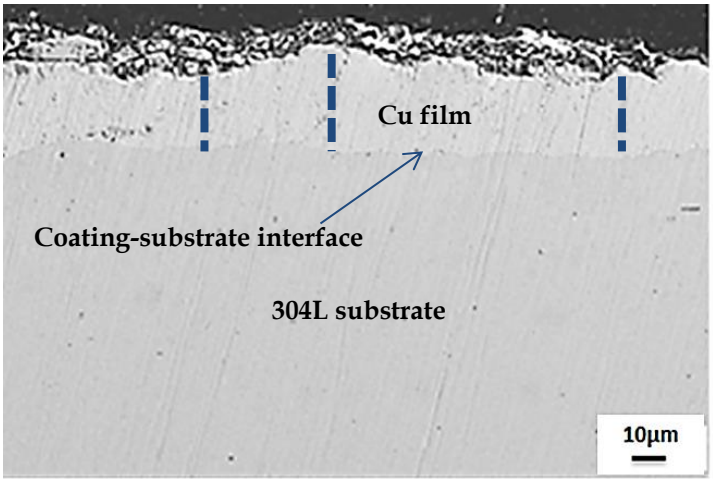


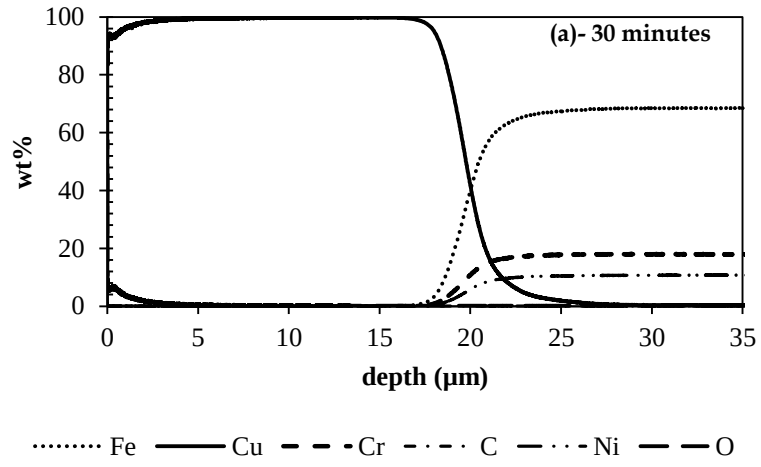
Figure 4.16: FESEM-BSE showing the difference between the copper coating and the 304L stainless steel substrate, as well as typical measuring points to determine coating thickness.

To confirm the adhesion of the coating, a heat-quench adhesion test was performed and the adhesion results are shown in Figure 4.17. The coatings experienced blistering and this was attributed to the entrapment of the plating solution during the deposition process. No peeling was observed adjacent to these blisters. Therefore, the coatings exhibited superior adhesion as indicated by the ASTM B571-97 standard [6]. However, it was noted that these blisters can become areas of initiation of the attack of the coating, as they can easily be eroded away by the fast moving gases in the exposure environment.

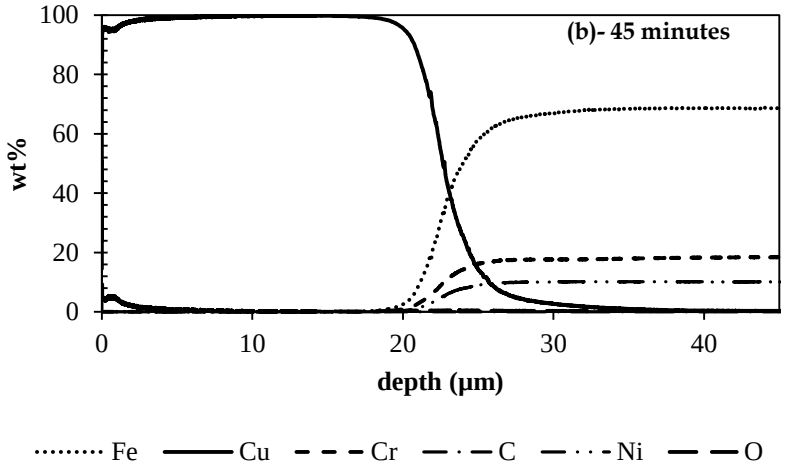


Figure 4.17: Heat-quenched of the copper electroplated samples.

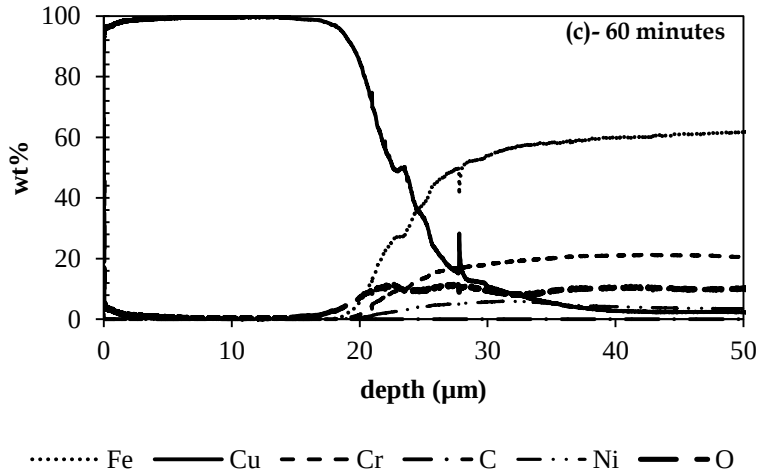
Elemental analysis of the copper coatings obtained from GDOES analysis indicated that the coatings consisted of copper only, with no contaminants except for the sample plated for 60 minutes. GDOES analysis indicated that the copper coating contained approximately 8% oxygen along its depth profile, this was suspected to be trace oxygen during the annealing process, as will be evidenced by the XRD analysis. The copper and iron depth profiles also show a variation in the concentrations close to the transition point as shown in Figure 4.18 (c).



(a)



(b)



(c)

Figure 4.18: GDOES plots of depth vs wt% of the electroplated copper samples and the elemental concentration profile of Fe, Ni, Cu, Cr, C, Ni and O at the interface of the copper plated 304L samples: (a) 30 minutes, (b) 45 minutes and (c) 60 minutes.

4.3.1.2 XRD surface characterization

X-ray diffraction characterisation of the copper electroplated surface indicated the presence of copper and copper oxide (Cu_2O) after annealing as shown in Figure 4.19. Therefore, the electroplated samples were entirely covered by the plating, since no stainless steel phases were detected.

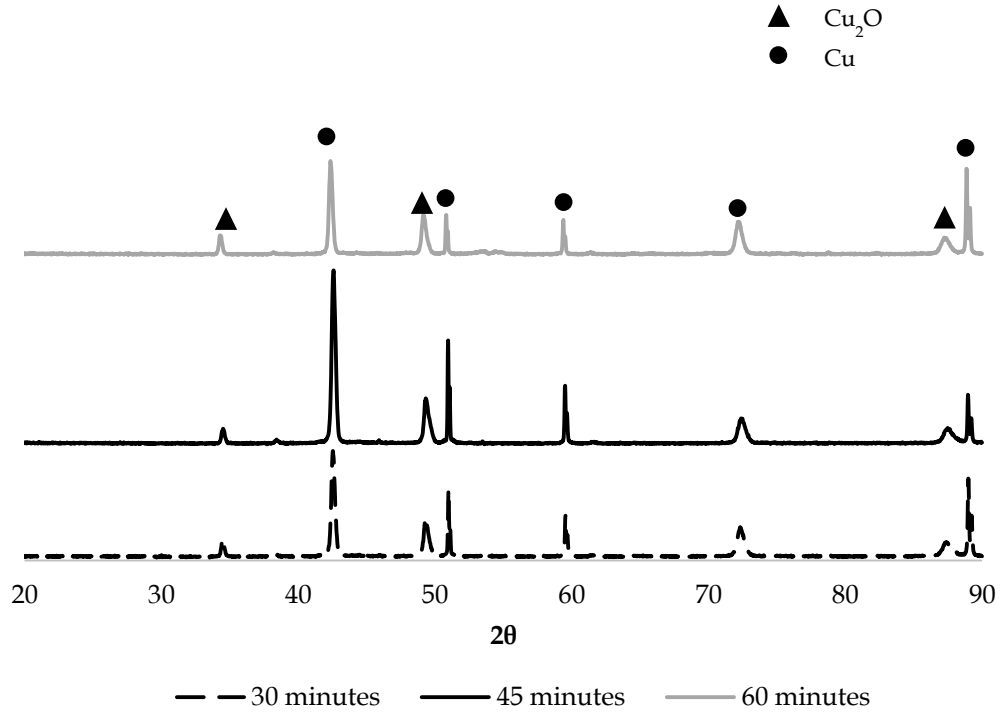


Figure 4.19: XRD spectra of surface of the samples electrodeposited with copper for 30, 45 and 60 minutes.

4.4.1.3 Hardness Profile

The hardness of the copper coating at the 304L interface increased with increasing plating time as shown in the hardness profiles in Figure 4.20. The average hardness of the coatings were 43, 55 and 66 HV for the 30, 45 and 60 minutes electroplated samples respectively. This was unexpected because the etched microstructural analysis showed that the copper electroplatings consist of nano-sized grains with their size that increased with increasing plating time. Therefore coating thickness could have contributed to the increase in hardness and possibly the introduction of residual stresses. However, the 304L substrate hardness remained constant at an average of 180 HV.

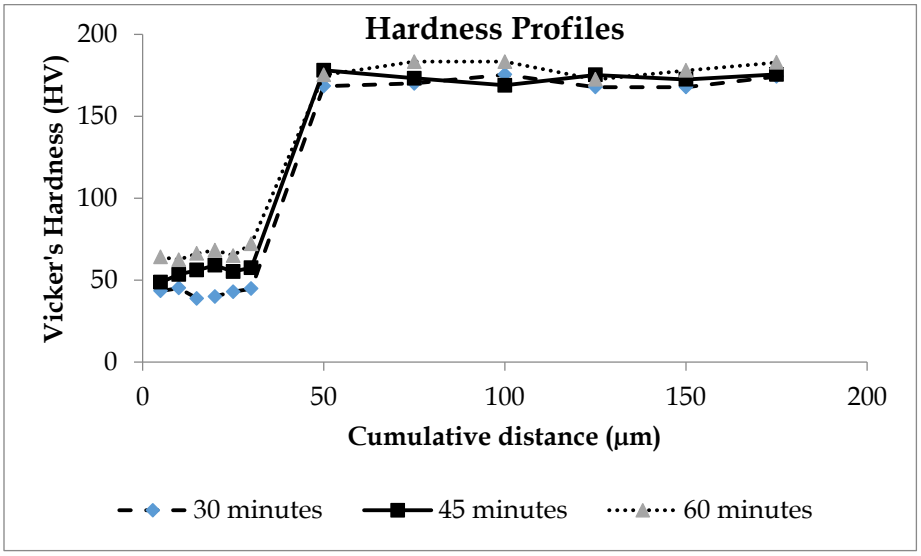


Figure 4.20: Hardness profiles at the interface of the cross-section of the electroplated 304L stainless steel.

4.3.2 Post-exposure results

After exposing the samples to a metal dusting environment, the samples were analysed using the FESEM, XRD-grazing incidence and Raman spectroscopy. A cross-sectional analysis was also conducted using the FESEM.

4.3.2.1 Mass Change results

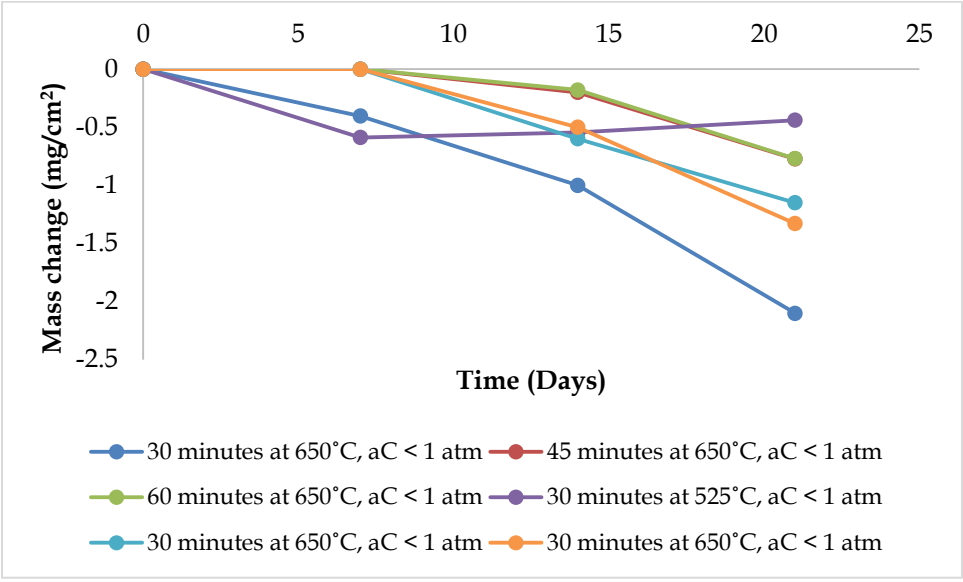


Figure 4.21: Change in mass of the 304L stainless steel copper electroplated for 30,45 and 60 minutes, exposed for 21 days at 525 and 650˚C.

The change in mass of the copper electroplated samples was measured after exposure to a metal dusting favourable environment. Figure 4.21 shows the changes in the mass of the copper electroplated samples.

(a) Mass change results after exposure to aC < 1 atm

Mass change due to exposure to 525˚C over a period of 21 days with an a_C of 0.657 atm and a P_{O2} of 1.559×10^{-27} atm, only occurred on the sample electroplated for 30 minutes and not on any of the other exposed samples. The sample lost a total mass of 1.15mg/cm^2 after 21 days of exposure as shown in Figure 4.21. It was postulated that the mass loss was caused by oxidation of the copper coating.

After exposure to the metal dusting environment at 650˚C with a carbon activity of 0.512 atm and partial pressure of oxygen, 5.118×10^{-24} atm, for 21 days; the samples on which copper was electrodeposited for 30 and 45 minutes exhibited mass loss. However, the sample electroplated for 60 minutes, did not show any mass change. Where the sample plated for 30 minutes lost 0.59 mg/cm^2 after seven days of exposure and then started to gain mass after continued exposure, this increase in mass is postulated to be a result of the mass gained by the substrate as continued exposure to the corrosive environment results in the exposure of the substrate, this will be further discussed under the cross-section results.

The sample plated for 45 minutes gradually lost mass over the exposure period, in total 1.33 mg/cm^2 over the exposure period of 21 days, as shown in Figure 4.21. It was postulated that the mass loss was caused by oxidation of the copper coating.

(b) Mass change results after exposure to aC >> 1 atm

The copper plated samples were exposed to a metal dusting environment at 650˚C containing a carbon activity of 35 atm. All the exposed samples showed a mass loss over the exposure period, with the highest mass loss on the sample plated for 30 minutes. After 21 days of exposure the sample electroplated for 30 minutes showed a total mass loss of 2.10 mg/cm^2. However, the samples electroplated for 45 and 60 minutes only

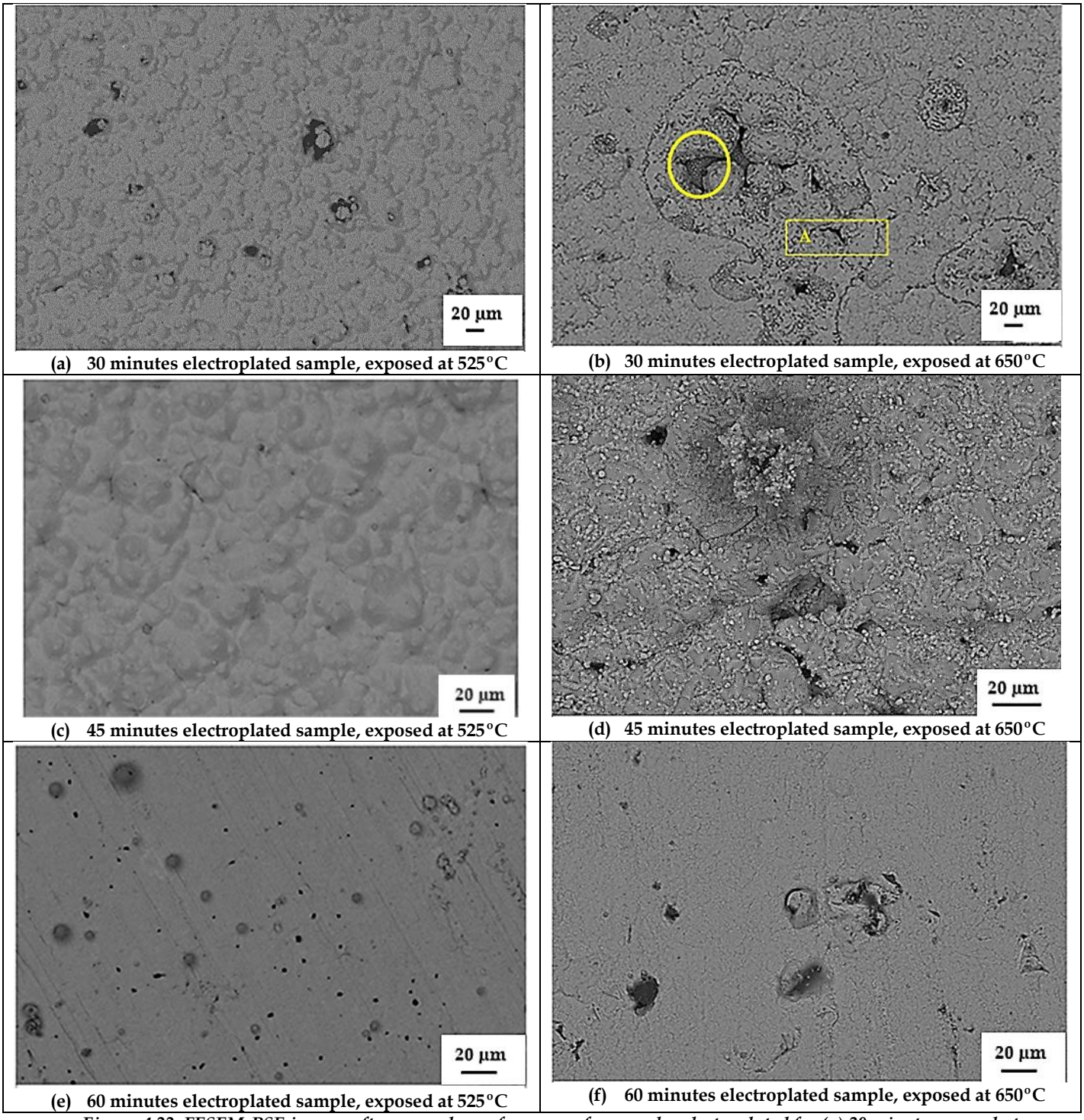
lost 0.778 and 0.771 mg/cm^2 respectively after 21 days of exposure as shown in Figure 4.21.

4.3.2.2 Exposure to low carbon activity (aC < 1 atm)

The copper plated samples exhibited surface degradation for the samples exposed at 525˚C after seven days, with an a_C of 0.657 atm and a P_{O2} of 1.559×10^{-27} atm as shown in Figure 4.22, though relatively low or no mass losses were observed. The FESEM images of the samples exposed at 525˚C showed that the samples plated for 30 and 45 minutes were relatively rough with large grains on the surface Figure 4.22 (a) and (c). The sample plated for 30 minutes indicated areas of corrosion debris and holes in the copper plating. The microvoids observed on the 60 minutes plated sample are speculated to be a result of corrosion attack as the microvoids/pores were not observed pre-exposure.

In contrast the FESEM analysis of the samples exposed at 650˚C for seven days, showed a rough surface with pores on the 30 minutes plated sample as seen in Figure 4.22 (b), in contrast to the 45 and 60 minutes plated samples which exhibited relatively smoother surfaces, very few pores, with the grinding lines still visible as shown in Figure 4.22 (d) and (f).

The sample on which copper was deposited for 30 minutes exposed at 650˚C exhibited the largest pores and in those pores is a structure that is made up of smaller grains as seen in the highlighted area in Figure 4.22 (b). These visible smaller grains are suspected to be the micron and nano-particles that make up the coating as shown in Figure 4.15. Furthermore, these pores appear to be as a result of the grains being dislodged from the structure, appearing as if the dislodging occurs due to attack of the copper along the grain boundaries as indicated by the area labelled A, in Figure 4.22(b).



(a) 30 minutes electroplated sample, exposed at 525°C

(b) 30 minutes electroplated sample, exposed at 650°C

(c) 45 minutes electroplated sample, exposed at 525°C

(d) 45 minutes electroplated sample, exposed at 650°C

(e) 60 minutes electroplated sample, exposed at 525°C

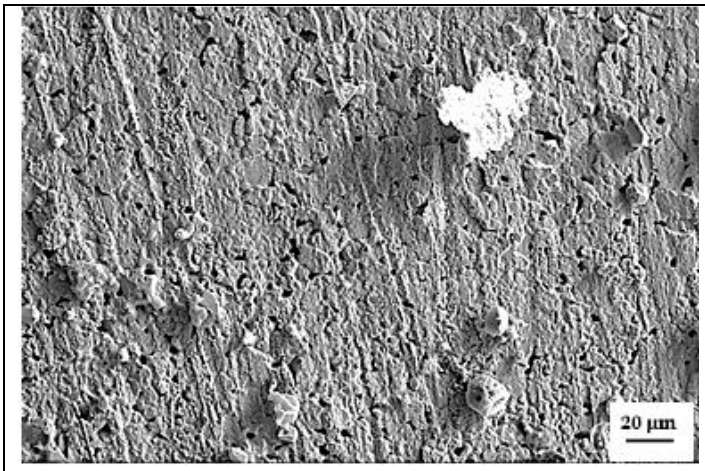
(f) 60 minutes electroplated sample, exposed at 650°C

Figure 4.22: FESEM-BSE images after seven days of exposure for samples electroplated for (a) 30 minute exposed at 525°C (b) 30 minutes exposed at 650°C, (c) 45 minutes exposed at 525°C, (d) 45 minutes exposed at 650°C, (e) 60 minutes exposed at 525°C and (f) 60 minutes exposed at 650°C.

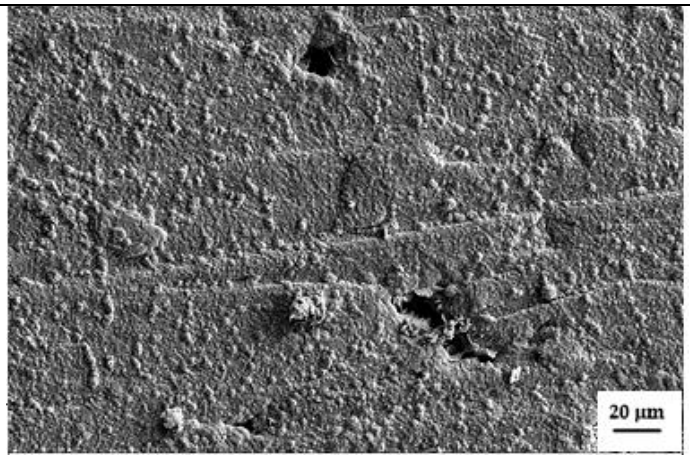
The sample on which copper was deposited for 45 minutes also exhibited pores, however, the pores were smaller in size relative to those observed on the sample electroplated for 30 minutes. Moreover, corrosion debris was deposited on the sample. It was also much clearer that the pores occur on the grain boundaries indicating that the sample undergoes intergranular attack. The 60 minutes plated sample did not have any pores but there are areas that appear to be uneven where it looks like the attack was being initiated as highlighted in Figure 4.23 (d). However, no significant attack was observed on the 60 minutes plated sample. The pores observed on this sample are suspected to be a result of corrosion attack as they were not observed on the as-received samples as shown in Figure 4.14.

Analysis of the copper electroplated samples after 21 days of exposure at 525^{o}C, indicated that the coatings had increased porosity but this porosity appeared to decrease with increasing deposition time. The pore size seemed to fluctuate, with the sample deposited for 30 minute exhibiting the largest pores and the sample deposited for 45 minutes containing the smallest pores. An anomaly was that the sample on which copper was deposited for 60 minutes formed larger pores than the 45 minutes sample. The pores are not clearly defined on the sample electroplated for 60 minutes however, it was observed that there was an intergranular type pattern of attack as highlighted in Figure 4.23 (e). No carbon was detected using EDS on these samples, however copper and oxygen were detected in high quantities indicating the formation of a copper oxide layer on the samples as well as other substrate ions such iron.

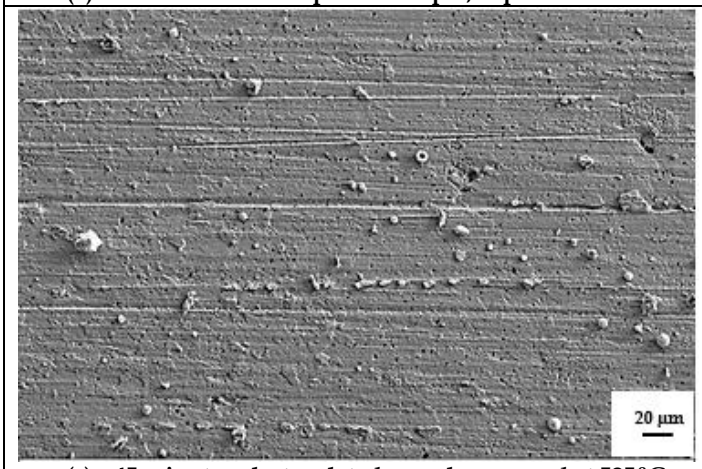
After exposure at 650^{o}C for 21 days the copper plated samples were analysed, using FESEM it is seen that the 30 and 45 minutes plated samples had pits on them, where the 30 minutes sample had larger pits which were fewer than the smaller and many pits found on the 45 minutes plated sample as indicated in Figure 4.23 (c) and (e). No pits or pores were observed on the 60 minutes plated sample in fact the coating had no indication of any attack, only corrosion debris was visible on the sample surface.



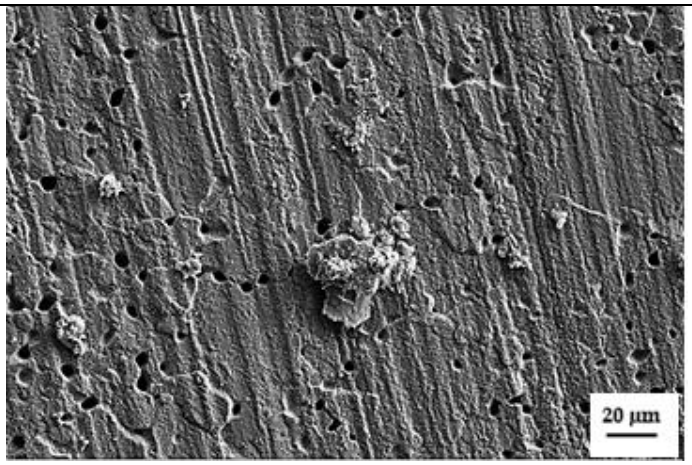
(a) 30 minutes electroplated sample, exposed at 525°C



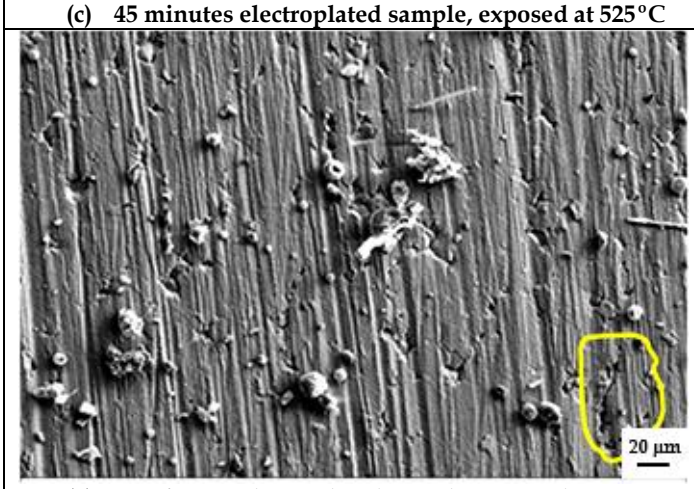
(b) 30 minutes electroplated sample, exposed at 650°C



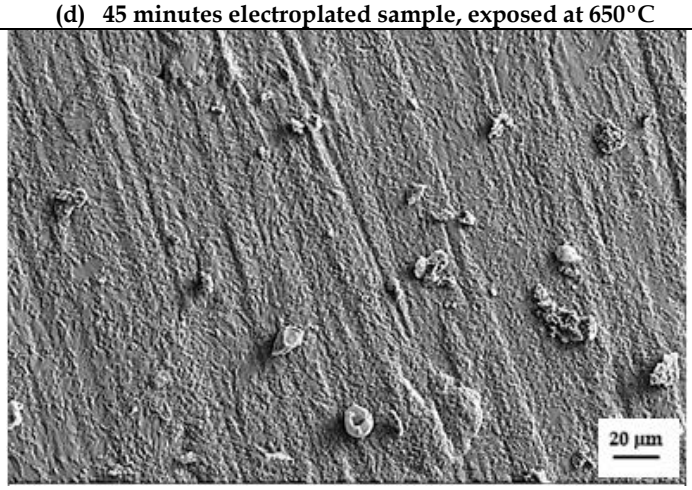
(c) 45 minutes electroplated sample, exposed at 525°C



(d) 45 minutes electroplated sample, exposed at 650°C

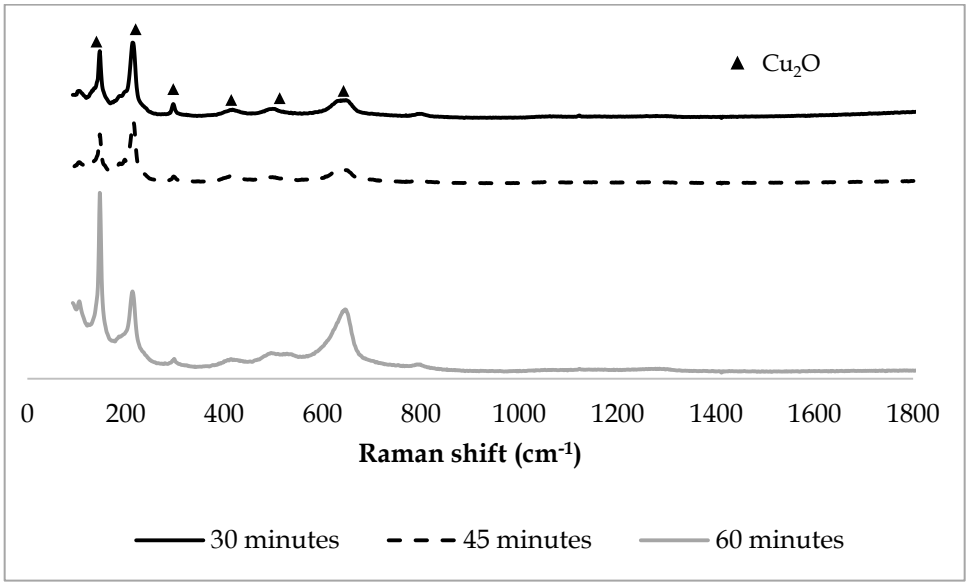


(e) 60 minutes electroplated sample, exposed at 525°C

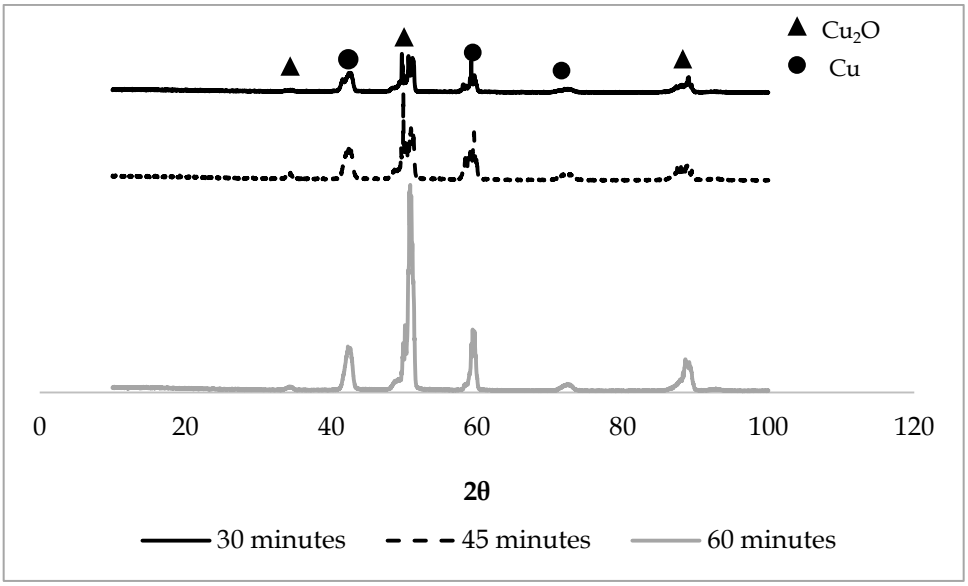


(f) 60 minutes electroplated sample, exposed at 650°C

Figure 4.23: FESEM-BSE after 21 days of exposure for samples electroplated for (a) 30 minutes exposed at 525°C, (b) 30 minutes exposed at 650°C, (c) 45 minutes exposed at 525°C, (d) 45 minutes exposed at 650°C, (e) 60 minutes exposed at 525°C and (f) 60 minutes exposed at 650°C.

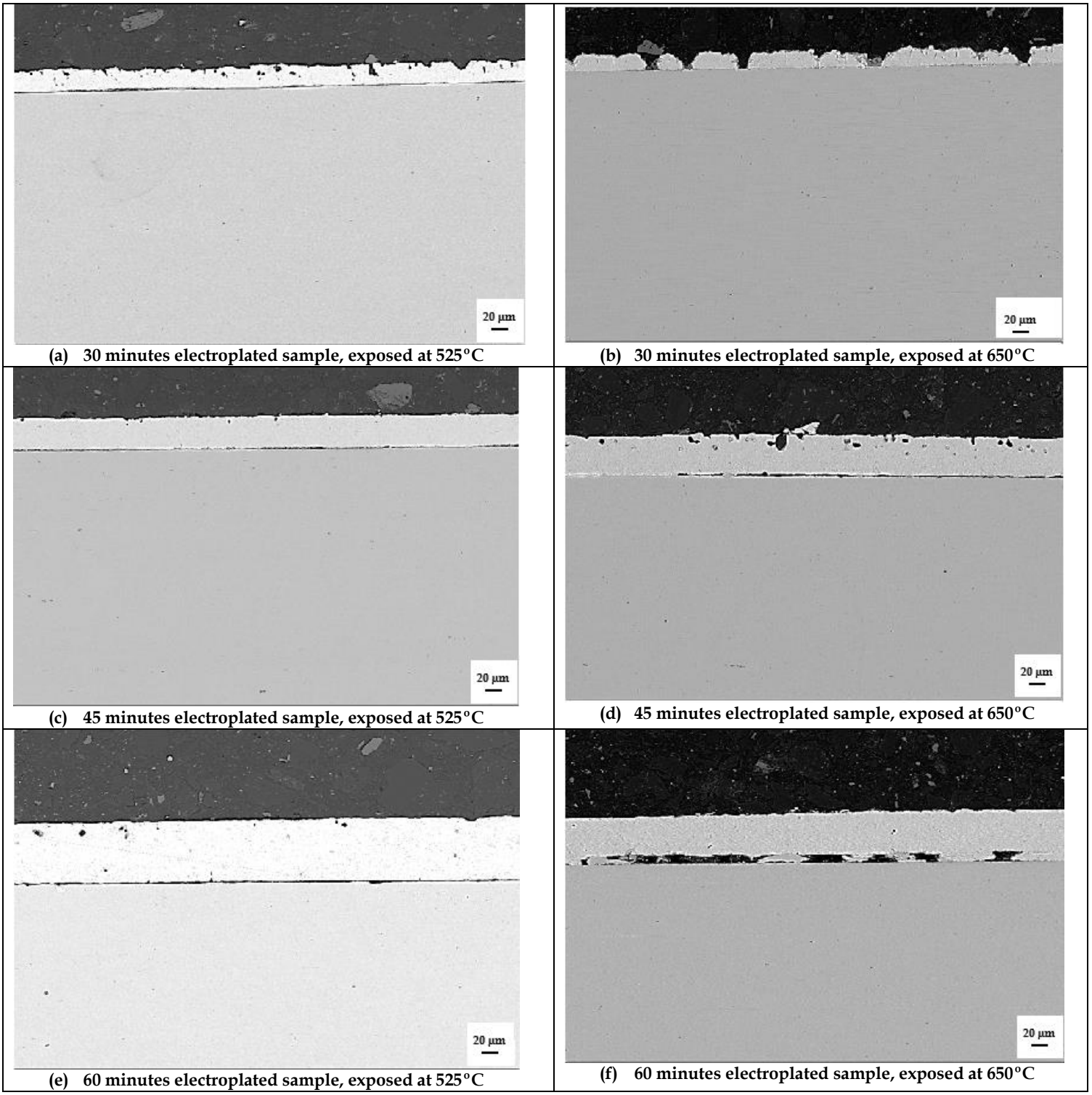


(a)



(b)

Figure 4.24: (a) Raman spectra and (b) GIXRD spectra of the samples copper electroplated for 30, 45 and 60 minutes exposed for 21 days.



(a) 30 minutes electroplated sample, exposed at 525°C

(b) 30 minutes electroplated sample, exposed at 650°C

(c) 45 minutes electroplated sample, exposed at 525°C

(d) 45 minutes electroplated sample, exposed at 650°C

(e) 60 minutes electroplated sample, exposed at 525°C

(f) 60 minutes electroplated sample, exposed at 650°C

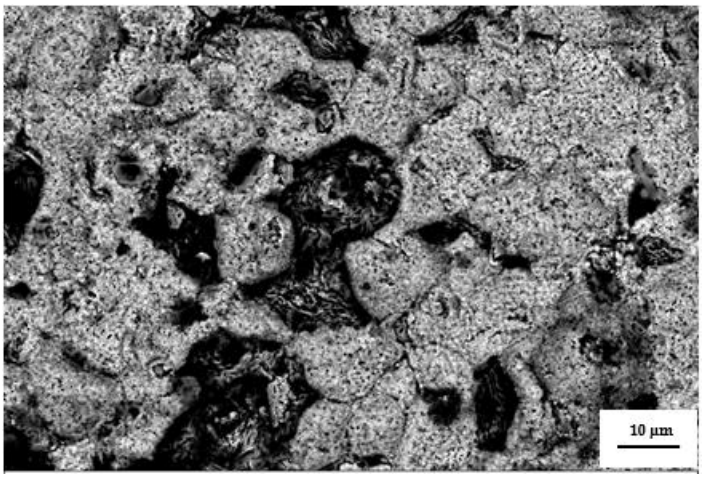
Figure 4.25: FESEM-BSE cross-section after 21 days of exposure for samples (a) 30 minutes exposed at 525°C, (b) 30 minutes exposed at 650°C, (c) 45 minutes exposed at 525°C, (d) 45 minutes exposed at 650°C, (e) 60 minutes exposed at 525°C and (f) 60 minutes exposed at 650°C.

All the exposed samples formed cuprous oxide on the exposed surface at both 525°C and 650°C, as characterised by the Raman and GIXRD spectra shown in Figure 4.24 (a) and (b) respectively. There was also some metallic copper as shown by the GIXRD analysis.

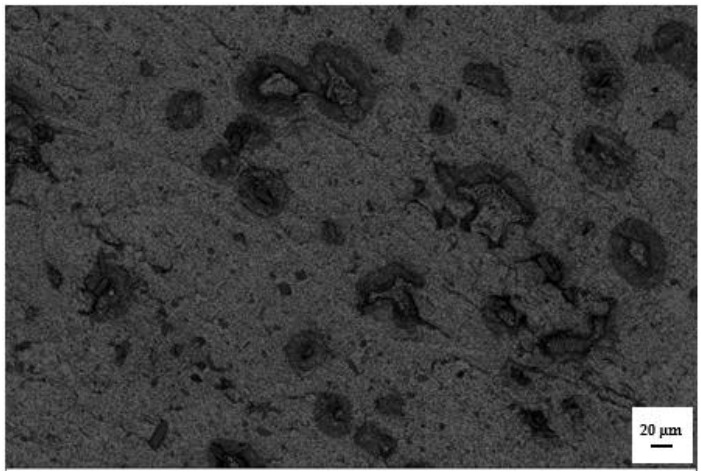
The cross-section of the copper coatings shows that the samples on which copper was deposited on for 30 minutes and 45 minutes were porous after exposure. The 30 minutes sample exposed at 650°C, for 21 days resulted in the copper almost being entirely removed as seen in Figure 4.25 (b). No internal subsurface oxidation or cracking was observed on any of the samples except the sample electroplated for 30 minutes and exposed at 650°C. The copper coating shielded the 304L from attack, from the gaseous aggressive environment on the majority of the samples. The coatings did, however exhibit poor adhesion as it can be distinctly seen that the coating is delaminating from the surface of the 304L.

4.3.2.3 Exposure to high carbon activity (aC >> 1 atm)

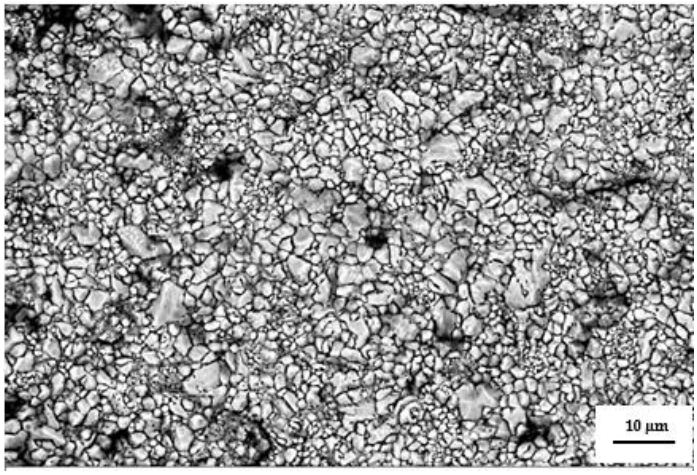
FESEM investigation of the samples exposed at 650˚C, to high carbon environment of a_C = 35 atm, after seven days showed that the copper coatings remained intact. However, pores formed on the coating as a result of copper oxidation. The pores density decreased with increasing coating deposition time as shown in Figure 4.26. It appears that these pores initiate at the grain boundaries and eventually agglomerate to form large pores. The copper oxidation was initially intergranular, and appears to eventually become intragranular since complete grains are removed.



(a) 30 minutes electroplated sample, exposed at 650°C



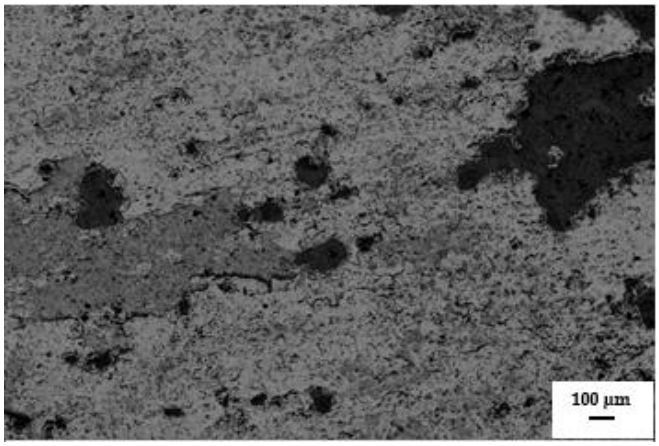
(b) 45 minutes electroplated sample, exposed at 650°C



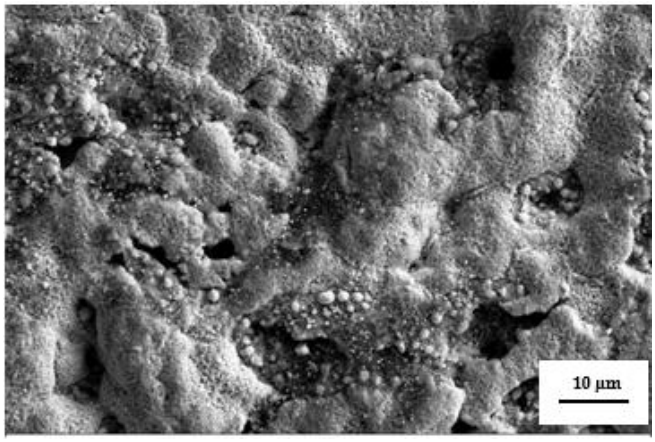
(c) 60 minutes electroplated sample, exposed at 650°C

Figure 4.26: FESEM-BSE images of samples after seven days of exposure to 650ºC for samples plated for: (a) 30 minutes, (b) 45 minutes and (c) 60 minutes.

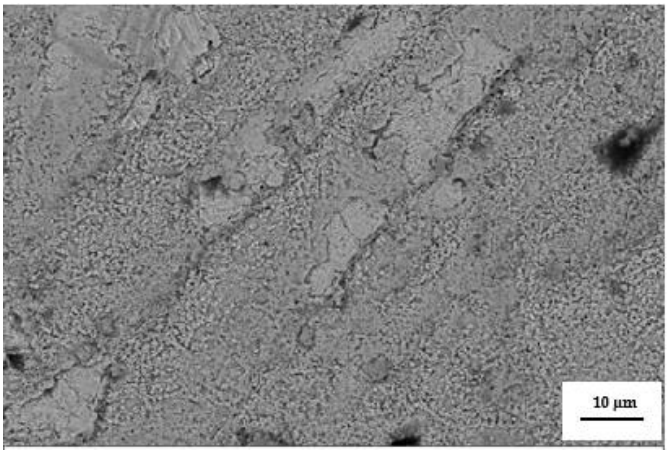
After 21 days of exposure the samples, under FESEM analysis, exhibited the same behaviour as the samples exposed to a metal dusting environment for seven days. Though, the oxidation had occurred to a larger extent, such that all the samples had formed pores on the surface. In addition the copper coating on the sample electroplated for 30 minutes was entirely removed in some areas, exposing the substrate, which catalysed carbon deposition, hence the black areas in Figure 4.27 (a). The porosity of the exposed samples is postulated to have provided the corrosive gases access to the substrate which allowed for catalysis of solid carbon deposition.



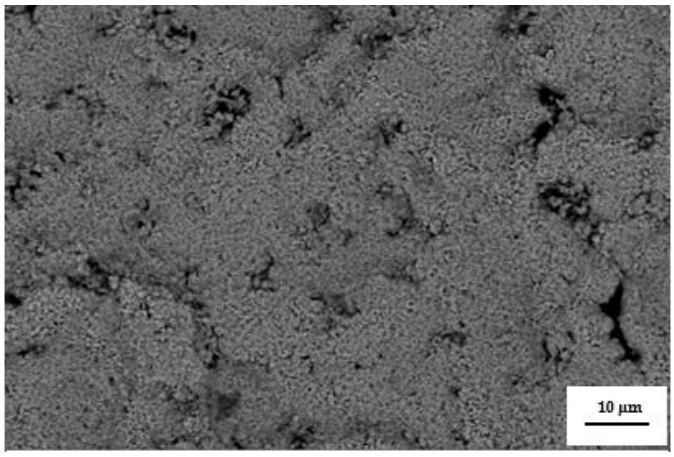
(a) 30 minutes electroplated sample, exposed at 650°C



(b) 30 minutes electroplated sample, exposed at 650°C



(c) 45 minutes electroplated sample, exposed at 650°C

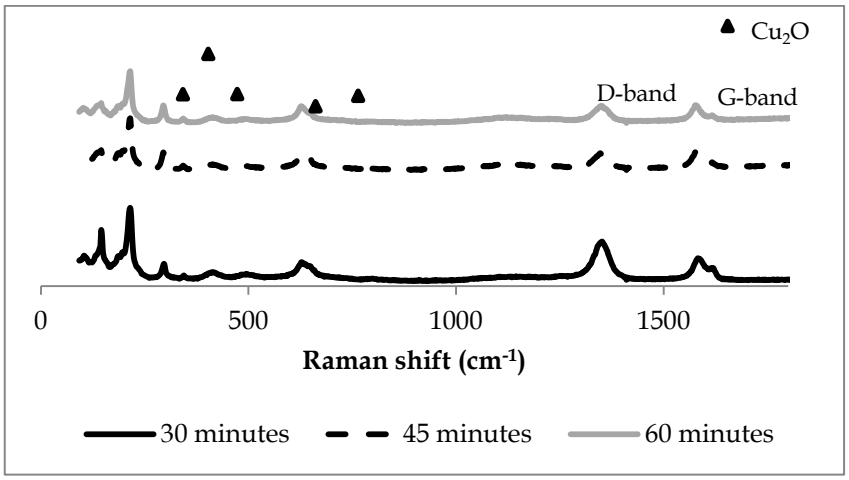


(d) 60 minutes electroplated sample, exposed at 650°C

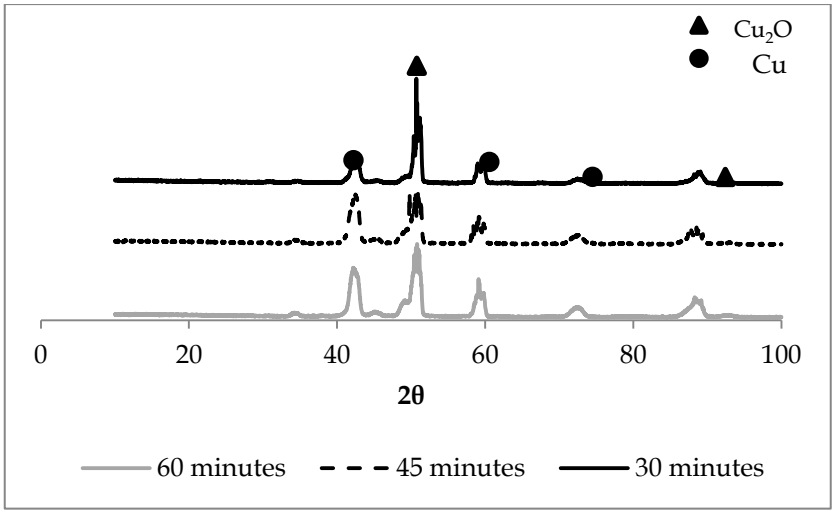
Figure 4.27: FESEM-BSE after 21 days of exposure for samples plated for (a) 30 minutes at low magnification (b) 30 minutes at high magnification, (c) for 45 minutes and (d) for 60 minutes.

The samples exposed to a high carbon activity containing environment behaved in a similar manner as those exposed to a low carbon environment ($a_C < 1$), by forming

cuprous oxide as characterised by the Raman and GIXRD spectra shown in Figure 4.28 (a) and (b) respectively. All the copper electroplated samples had carbon deposited on them after 21 days of exposure as shown by the presence of the D and G bands in Figure 4.28. The carbon was amorphous in nature with an I_D/I_G ration less than unity, falling in the range between 0.84-0.95 [7-9]. The GIXRD analysis showed the presence of copper on the surface as well. Additionally, there was carbon deposited on the surface of the electroplated samples as shown by the Raman spectra in Figure 4.28 (a).

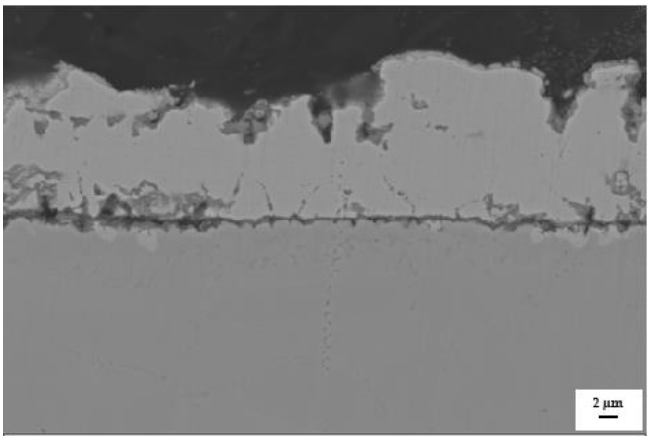


(a)

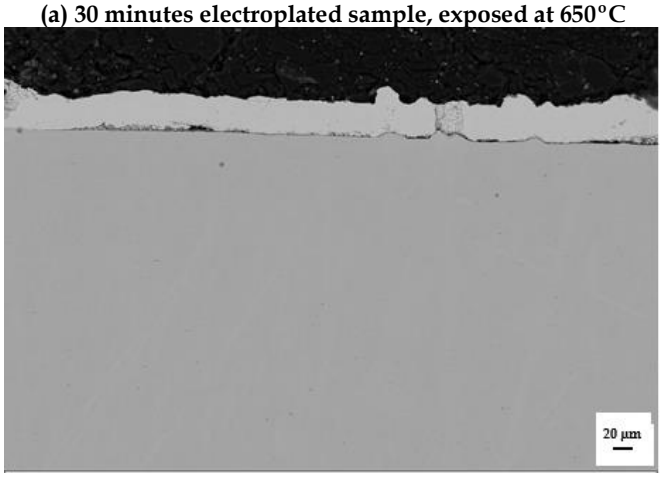


(b)

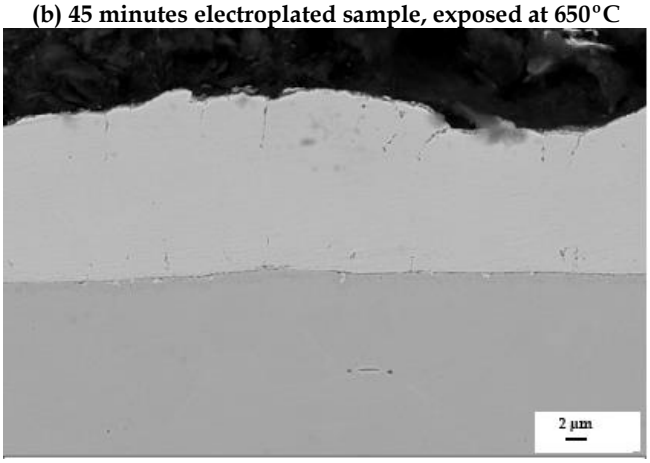
Figure 4.28: (a) Raman spectra and (b) GIXRD spectra of the copper electroplated samples exposed for 21 days at 650°C.



(a) 30 minutes electroplated sample, exposed at 650°C



(b) 45 minutes electroplated sample, exposed at 650°C



(c) 60 minutes electroplated sample, exposed at 650°C

Figure 4.29: FESEM-BSE cross-section after 21 days of exposure at 650ºC, with a carbon activity of 35 atm, for samplescopper plated for: (a) 30 minutes (b) 45 minutes (c) 60 minutes.

The cross-sectional analysis of the samples electroplated for 30 and 45 minutes showed that the corrosive gases penetrated to the substrate interface, as shown in Figure 4.29 (a) and (b). However, the sample electroplated for 60 minutes as shown in Figure 4.29 (c),

there was no evidence of the substrate- interface interacting with the corrosive gases and this is hypothesised to be a result of the relatively thick coating preventing the ingress of the gases.

4.3.3 Discussion

A general observation was that most of the samples did not undergo significant mass loss in the first seven days and maintained relatively the same mass, and yet there was evidence of surface degradation. It is proposed that the copper samples underwent a cyclic process of corrosion and self-healing where the copper oxide formed would form and subsequently decompose freeing up oxygen and copper ions to form further copper oxide. This concept would need further study using Thermo Gravimetric Analysis (TGA), which tend to be more sensitive to mass changes leading to more accurate mass changes and subsequently a more precise study of the kinetics of copper oxidation.

The copper coatings imparted complete protection of the coated substrate against metal dusting. The results obtained for the exposed samples confirm what other researchers [10-15] have found, that copper is non-catalytic to carbon deposition therefore preventing metal dusting by inhibiting subsequent metal dusting steps such as the dissolution of copper and graphite formation. This protection was independent of how thick the coating was and this was confirmed by others such as Chun, Desai and Ramanarayanan as well as Natesan and Zeng [10,11]. The deposition technique also does not influence the protection as the mentioned works used different plating techniques and achieved full protection against metal dusting even on steels with inferior corrosion resistance to stainless steel 304L.

In metal dusting environments there is often competition between the carbon and oxygen species to react with the material. As a result copper oxidised to form the non-protective Cu_2O, which causes accelerated copper oxidation, explaining the presence of the "pores" which are indicative of copper oxidation [15-20]. The pores are a result of the oxidation by bulk diffusion along the grain boundaries of the Cu^{2+} ion, leaving vacancies allowing for pitting where these pits agglomerate into large pores [15,16]. The

rate at which copper was being consumed was most likely the same on all the coatings; therefore the variation in the "pore" size is suggested to be a result of the thickness of the coating allowing for easy diffusion (Kirkendall Effect) of the ions in the substrate such as iron therefore accelerating the oxidation of the copper and the formation of voids at the surface [21-24]. This theory can be further supported by the fact that the oxidation of copper occurs by outward bulk diffusion of copper cations along the grain boundaries at this exposure temperature, therefore implying outward cation diffusion was the oxidation catalyst.

The deposition time influenced the thickness of the coating and the length of time the coating would protect the stainless steel against metal dusting [3,4]. However, a longer exposure time would certainly result in the removal of the copper due to copper oxidation therefore exposing the 304L stainless steel.

4.3.4 Summary

The protective effect of copper electrodeposition on 304L stainless steel by the pulse plating technique was investigated in a metal dusting environment. The copper coatings protected the stainless steel substrate against metal dusting regardless of the deposition time.

It was found that increasing plating time resulted in thicker coatings and the thicker the coating the smaller and the fewer the number of microvoids/pores formed on the coating therefore resulting in better protection as the gas diffusion towards the substrate was reduced. The thicker coatings protected the substrate for longer periods as the oxidation process had to corrode away a much thicker copper layer therefore increasing the life span of the coating. Longer exposure times would however, result in the eventual removal of the copper exposing the 304L stainless steel substrate.

It was found that the higher the exposure temperature the faster the copper oxidation was most likely to take place as evidenced by the sample that was plated for 30 minutes and exposed to a metal dusting environment at 650^{o}C for 21 days.

4.3.5 References

1. H. Zhou, Z. Liao, C. Fang, H. Li, B. Feng, S. Xu, G. Cao and Y. Kuang, Pulse electroplating of Ni-W-P coating and its anti-corrosion performance, *Transactions of Nonferrous Metals\society of China,* vol. 28, pp. 88-95, (2018).
2. V. Ezhil Selvi, H. Seenivasan and K.S. Rajam, Electrochemical corrosion behaviour of pulse and DC electrodeposited Co-P coatings, *Surface and Coatings Technology,* vol. 206, pp. 2199-2206, (2012).
3. J.B. Marro, T. Darroudi, C.A. Okorod, Y.S. Obeng and K.C. Richardson, The influence of pulse plating frequency and duty cycle on the microstructure and stress state of electroplated copper films, *Thin Solid Films,* vol. 621, pp. 91-97, (2017).
4. W.Tsai, C. Wan and Y. Wang, Mechanisms of copper electrodeposition by pulse current and its relation to current efficiency, *Journal of Applied Electrochemistry,* vol. 32, pp. 1371-1378, (2002).
5. Y. Feng, G.E. McGuire, O.A. Shenderova, H. Ke and S.L. Burkett, Fabrication of copper/carbon nanotube composite thin films by periodic pulse reverse electroplating using nanodiamond as a dispersing agent, *Thin Solid Films*, vol. 615, pp. 116-121, (2016).
6. ASTM B571-97(2013), Standard Practice for Qualitative Adhesion Testing of Metallic Coatings, ASTM International, West Conshohocken, PA, (2010).
7. Z. Zeng, K. Natesan and V.A. Maroni, Investigation of metal-dusting mechanism in Fe-base alloys using Raman spectroscopy, X-ray diffraction and electron microscopy, *Oxidation of Metals*, vol. 58, pp. 147-170, (2002).
8. Z. Zeng and K. Natesan, Relationship between the growth of carbon nano-filaments and metal dusting corrosion, *Journal of the American Chemical Society*, vol. 17, pp. 3794-3801, (2002).
9. A.C. Ferrari and J. Robertson, Interpretation of Raman spectra of disordered and amorphous carbon, *Physical Review B*, vol. 61, pp. 14095-14107, (2000).
10. C.M. Chun, S. Desai and T.A. Ramanarayanan, Metal dusting resistant copper-based materials, *ECS Transactions*, vol. 41, no. 42, pp. 61-72, (2012).
11. K. Natesan and Z. Zeng, Development of materials resistant to metal dusting degradation, Final report, *Argonne National Laboratory- Nuclear Engineering Division*, pp.112-118, (2007).

12. Y. Nishiyama, K. Moriguchi, N. Otsuka and T. Kudo, Improving metal dusting resistance of transition-metals and Ni-Cu alloys, *Materials and Corrosion,* vol. 56, pp. 806-813, (2005).
13. Y. Nishiyama and N. Otsuka, The role of copper in resisting metal dusting of Ni-base alloys, *Material Science Forum,* vol. 522-523, pp. 581-588, (2006).
14. J. Zhang and D.J. Young, Effect of copper on metal dusting of austenitic stainless steels, *Corrosion Science*, vol. 49, pp. 1450–1467, (2007).
15. J. Zhang, D.M.I. Cole, and D.J. Young, Alloying with copper to reduce metal dusting of nickel, *Materials and Corrosion*, vol. 56, pp. 756–764, (2005).
16. Y. Zhu, K. Mimura, J-W. Lim, M. Isshiki and Q. Jiang, Brief review of oxidation kinetics of copper at 350^{o}C to 1050^{o}C. *Metallurgical and Materials Transactions A*, vol. 37, pp.1231–1237, (2006).
17. J.H. Park and K. Natesan, Oxidation of copper and electronic transport in copper oxides, *Oxidation of Metals*, vol. 39, pp. 411-435, (1993).
18. S.K. Lee, H.C. Hsu, and W.H. Tuan, Oxidation behavior of copper at a temperature below 300 ˚Cand the methodology for passivation. *Materials Research*, vol. 19, pp.51–56, (2016).
19. J. Li, G. Vizkelethy, P. Revesz, J.W. Mayer and K.N. Tu, Oxidation and reduction of copper oxide thin films, *Journal of Applied Physics*, vol. 69, pp. 1020-1029, (1991).
20. Li, J.W. Mayer and E.G. Colgan, Oxidation and protection in copper and copper alloy thin films, *Journal of Applied Physics*, vol. 70, pp. 2820-2827, (1991).
21. J. Hormadaly and M. Prudenziati, Chapter 3 - Materials Science concepts for printed films, Materials Science and Applications in Sensors, *Electronics and Photonics Woodhead Publishing Series in Electronic and Optical Materials*, pp. 63-89, (2012).
22. S.-Z. Qiao, J. Liu and G.Q. Max Lu, Chapter 21 - Synthetic Chemistry of nanomaterials, Second Edition, *Netherlands, Elsevier B.V.,* pp. 613-640, (2017).
23. H.J. Fan, M. Knez, R. Scholz, D. Hesse, K. Nielsch, M. Zacharias and U. Gösele, Influence of surface diffusion on the formation of hollow nanostructures induced by the Kirkendall effect: The basic concept, *Nano Letters*, vol. 7, pp. 993-997, (2007).

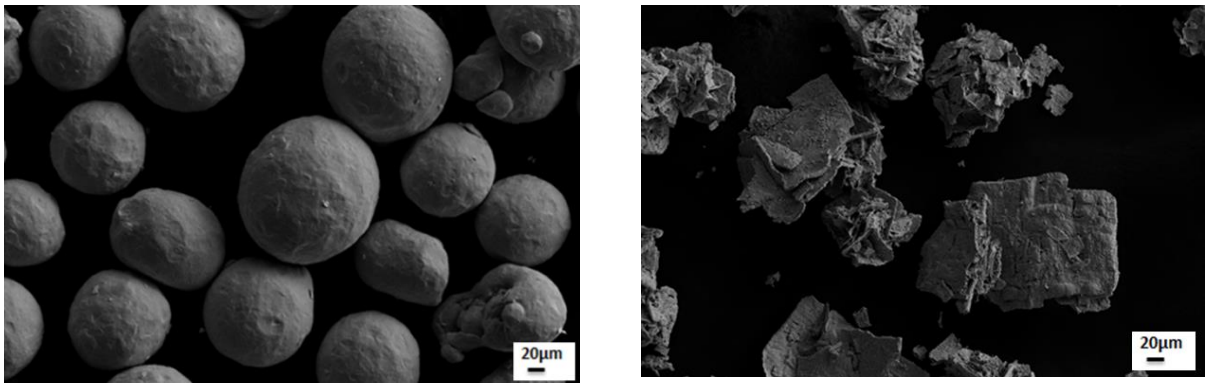
24. H.J. Fan, U. Gösele and M. Zacharias, Formation of nanotubes and hollow nanoparticles based on Kirkendall and diffusion processes: A review, *Small*, vol. 3, pp. 1660-1671, (2007).

4.4 Ruthenium Laser Cladding

This section outlines the characterisation of the laser cladded samples before and after exposure to the metal dusting environment.

4.4.1 Pre-exposure material characterisation

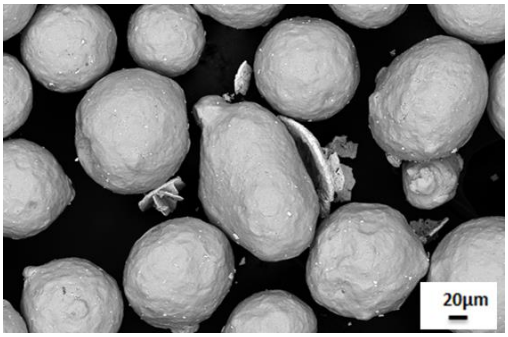
The powders used for the laser cladding process were characterised using FESEM to determine their particle size and shape, as shown in Figure 4.30. The 304L stainless steel powder particles were spherical in shape and approximately 50-120 µm in size. In contrast the ruthenium powder was agglomerated flakes that formed irregular shaped granules as shown in Figure 4.30 (b). The size of these granules varied between 81 µm up to 200 µm, with average size of 144 µm.



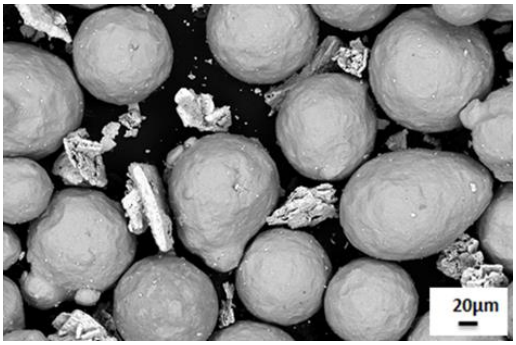
(a) **(b)**

Figure 4.30: FESEM-SE micrographs of the (a) stainless steel 304L and (b) ruthenium powder used for the laser cladding process.

The powders were mixed in a tubular mixer for two hours at a speed of 50 rpm and the powders appear to have mixed well as shown if Figure 4.31, particularly when considering the low concentrations of ruthenium added. The ruthenium appears to have been broken down during the mixing process, into smaller flakes, which contributed to the relatively good mixing process. However, pre-mixing the powders did not result in the production of a homogeneous laser cladded layers, since the claddings contained second phases which were ruthenium rich islands as shown in Figure 4.32.

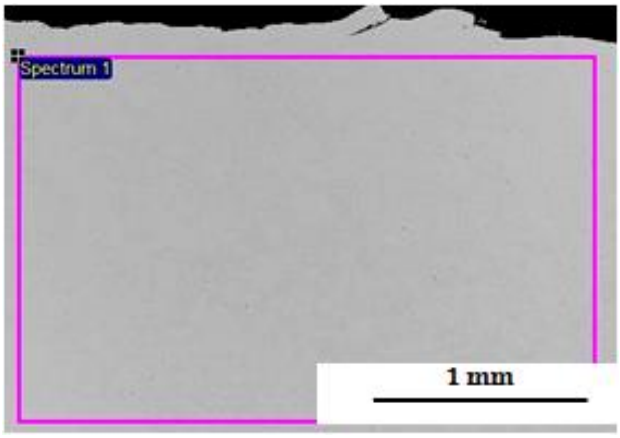


(a) 0.5 wt.% Ru

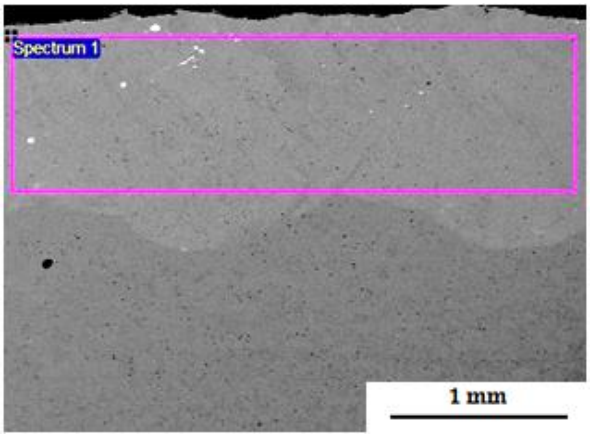


(b) 5 wt.% Ru

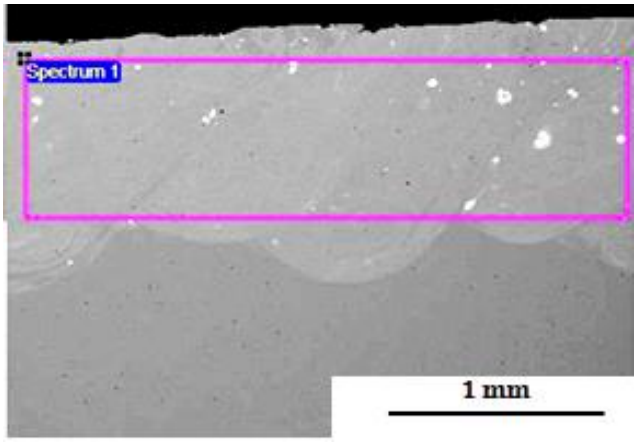
Figure 4.31: FESEM-BSE micrographs of the mixed powders with (a) 0.5 wt.% Ru and (b) 5 wt.% Ru used for the laser cladding process.



(a) 0 wt.% Ru



(b) 2 wt.% Ru



(c) 5 wt.% Ru

Figure 4.32: FESEM-BSE micrographs of the loaser cladded region with (a) 0.5 wt.% Ru and (b) 5 wt.% Ru used for the laser cladding process.

To elucidate the precipitation of the ruthenium seen in Figure 4.32, the iron-ruthenium phase diagram shown in Figure 4.33, was used as iron is the major constituent of 304L. The phase diagram indicates that for the dissolution of 5 wt.% (x_{Ru}≈ 0.0325) or less ruthenium in FCC iron, the operating temperature was required to be atleast 927°C (1200K). It was therefore suspected that the operating temperature during the laser cladding process was lower than this temperature hence the precipitation of the ruthenium. However, other alloying elements such as nickel may have improved the solubility of ruthenium at these lower temperatures for lower concentrations of ruthenium as the 0.5 wt.% Ru sample did not have any ruthenium precipitates [1,2].

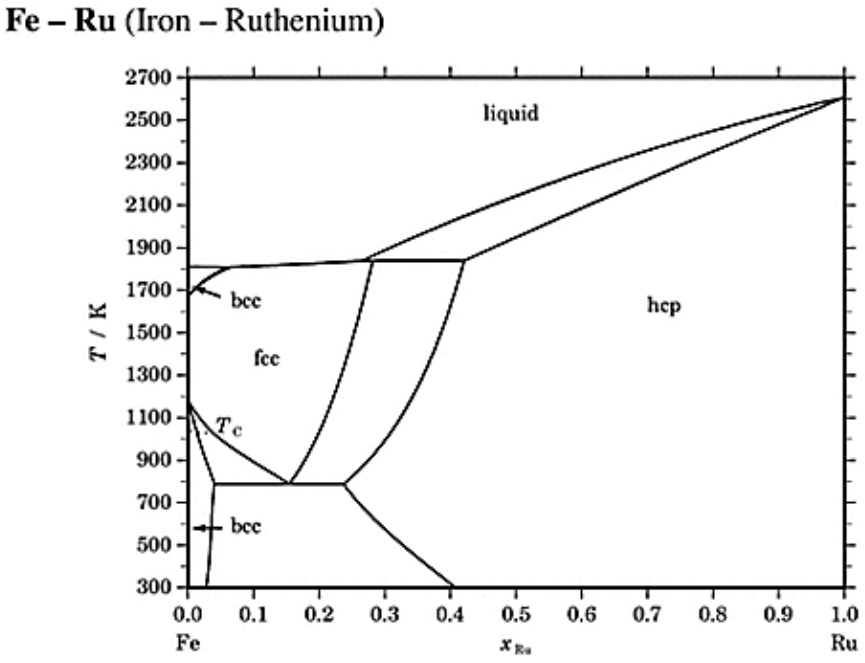


Figure 4.33: Fe-Ru phase diagram [3].

The laser cladding was achieved by melting the powders at temperatures greater than the melting temperatures of both metal powders and was solidified rapidly at conditions far removed from equilibrium. It would therefore be expected that the ruthenium would dissolve in the 304L stainless, however, Adenike showed in his PhD that austenite was able to maintain its structure in the presence of ruthenium at compositions between 0 and 0.2 wt.% hence the lower ruthenium samples were able to

form a uniform solid solution with the ruthenium. However, additions equal to 2 wt.% or greater resulted in the reduction of the austenite phase and the formation of an HCP phase. It was postulated that the ruthenium precipitation was the HCP phase, since ruthenium has an HCP structure [3,4].

The characterization results of the ruthenium laser cladded specimens, prior to exposure to a metal dusting environment are shown.

4.4.1.1 Microstructural Analysis

The analysis of the microstructure of the ruthenium laser cladded samples etched in 10% oxalic acid for 90 seconds, at 10 V revealed that the substrate was made up of large austenitic grains which are evident in Figure 4.34 and Figure 4.35. The rapid solidification due to the laser cladding process resulted in fine grains. The grains were small and equi-axed similar to what other researchers have found [5,6].

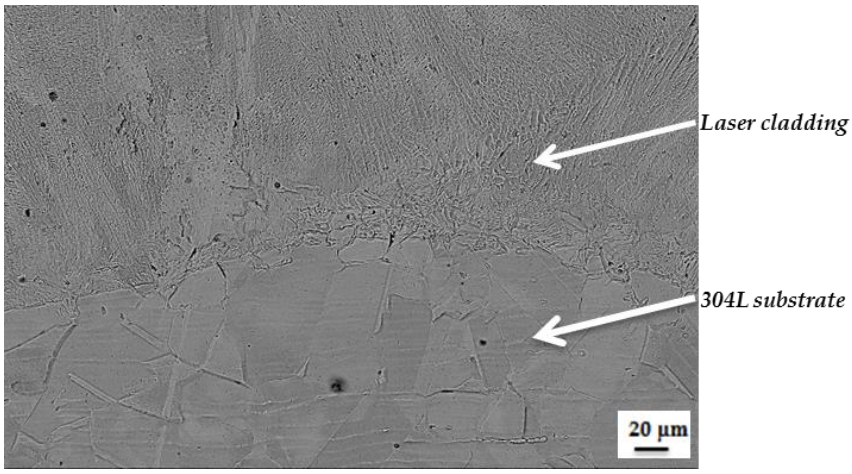


Figure 4.34: FESEM-BSD image of etched cross-section showing the contrast between the grains of the substrate and the laser cladding of the 0 and 0.5 wt.% Ru samples.

The addition of higher concentrations of ruthenium still maintained the grain refinement and a clearly defined interface between the substrate and the laser cladding was evident as shown in Figure 4.35. These higher ruthenium concentration samples where slightly over etched and to rectify this a lower etching time of 30 seconds was used, which unfortunately was not long enough to etch the substrate properly as shown

in Figure 4.36. Here the epitaxial solidification was clear and the grain growth was identified to be cellular as opposed to dendritic [5].

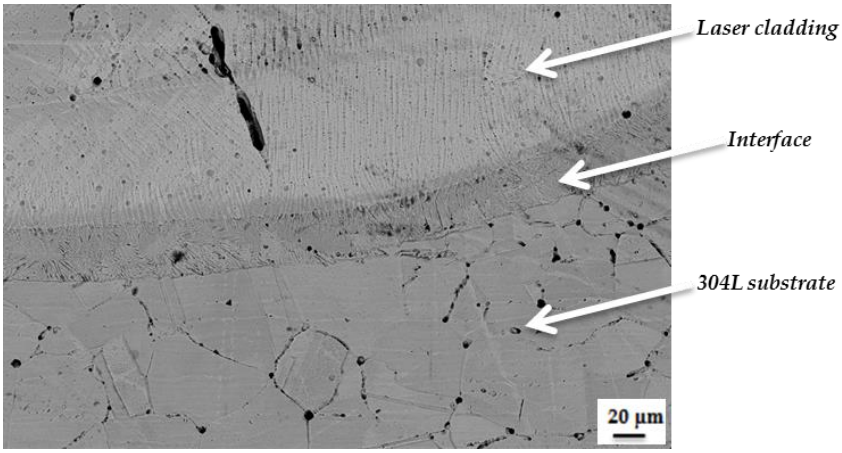


Figure 4.35: FESEM-BSD of the substrate and the laser cladding of the 2-10 wt.% Ru, contrasting different grain images.

Another interesting observation was that the areas enriched with ruthenium appeared to have been sites of nucleation for the solidification of the laser cladding, as the grains grow outwards from the ruthenium enriched areas refer to Figure 4.36. However, the ruthenium was removed at the enriched sites and this was a result of the etching of the 304L stainless. This was because ruthenium does not dissolve in most acids due to its nobility [7,8].

Analysis of the polished cross-section of the samples showed ruthenium enriched areas within the laser clad. This enrichment became visible in the 2 wt.% ruthenium sample and increased with increasing ruthenium concentration as shown in Figure 4.32. The ruthenium appeared as the white spots on the samples. This shows that the addition of ruthenium by laser cladding, did not distribute uniformly.

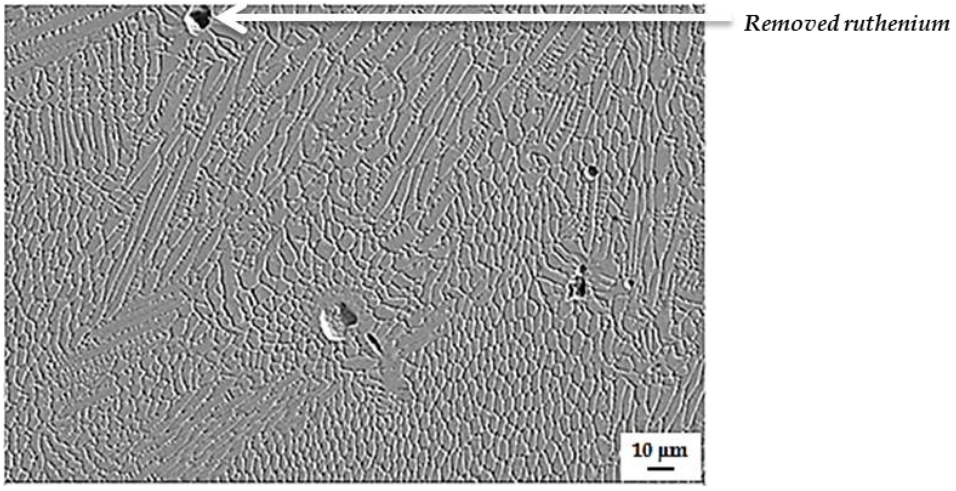


Figure 4.36: FESEM-SE micrograph of the ruthenium enriched sites on which the ruthenium was removed during the etching process.

A distinct fusion zone was shown in Figure 4.37 and the grains are much smaller than those observed on the laser cladding. A clear transition from the laser cladding to the substrate was observed and a distinct change in the grain size is observable in Figure 4.37. The fusion zone, which is the transition from the laser clad to the 304L substrate, is the interface shown in Figure 4.31.

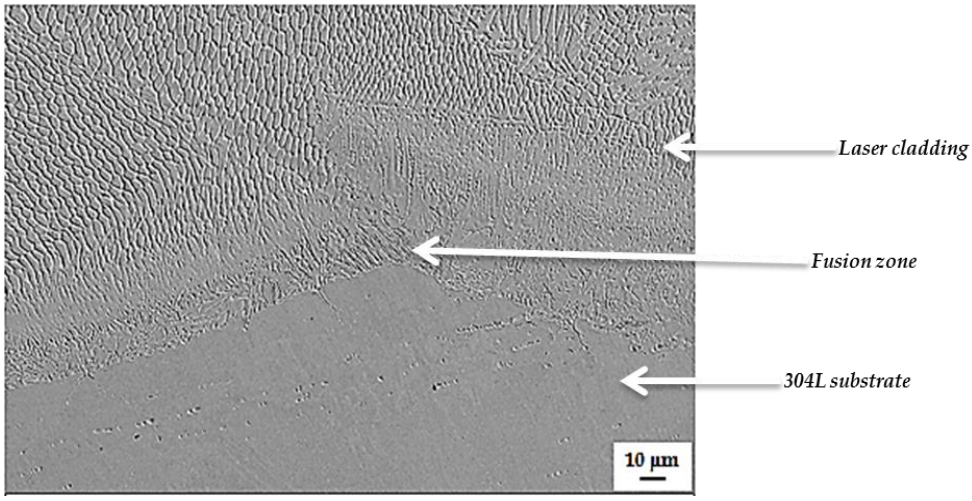


Figure 4.37: FESEM-SE micrograph of the grain size change from the laser cladding transition to the fusion zone and finally the substrate.

The approximate thicknesses of the ruthenium laser cladding, was measured from the microstructural analysis and the results are shown in Table 4-1.

Table 4-1: Approximate thicknesses of the laser cladding.

Sample	0 wt.%	0.5 wt.%	2 wt.%	5 wt.%
Thickness (µm)	1170±5	1186±5	1250±5	1178±5

4.4.1.2 XRD surface characterization

XRD characterization of all the cladded samples were performed and the results are shown in Figure 4.38, indicated the presence of 304L stainless steel peaks at 2θ equals, 50, 60 and 90°, but no ruthenium phase was detected, which may have been a result of the limitations of the XRD-D2 Phaser.

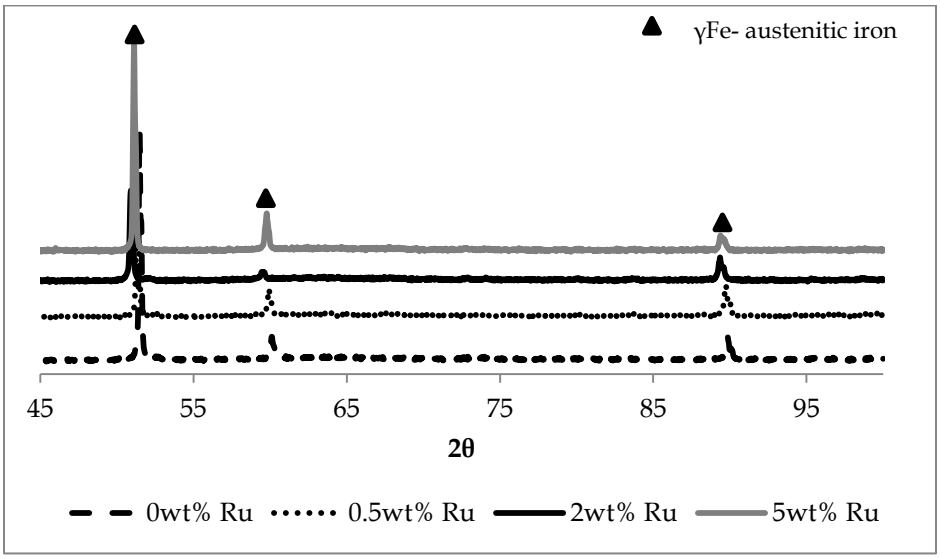


Figure 4.38: XRD spectrum of the laser cladded samples.

4.4.1.3 Hardness Profile

The hardness profiles of the laser claddings shown in Figure 4.39, show consistency in the hardness of the parent metal which is approximately 180 HV on average, which was close to the approximated hardness of 159 reported by suppliers [9]. The laser cladding tends to have higher Vicker's hardness values, Figure 4.39. This result was an expected result because laser cladding is a technique that results in the refinement of grains and improved hardness of the material [6,10]. The increase in the ruthenium content also results in increased hardness and this observation was consistent with reports in literature that claim that ruthenium additions harden materials as well as refine the

grains of a material [11]. Hardness itself is a property that is improved by grain refinement because the smaller the grains the higher the probability of the impedance of dislocation motion because there is a larger grain boundary surface area [12-14]. The higher the ruthenium content that is being cladded, the higher the hardness of the weld.

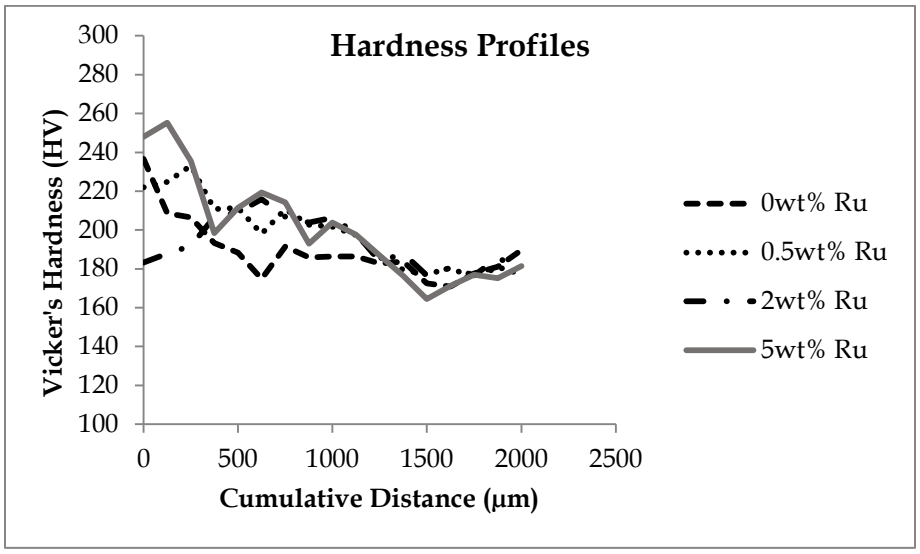


Figure 4.39: Hardness profiles of the laser cladded materials.

4.4.2 Post exposure results

The changes in mass were determined by measuring the mass gain or loss per area with increasing exposure time.

4.4.2.1 Mass Change results

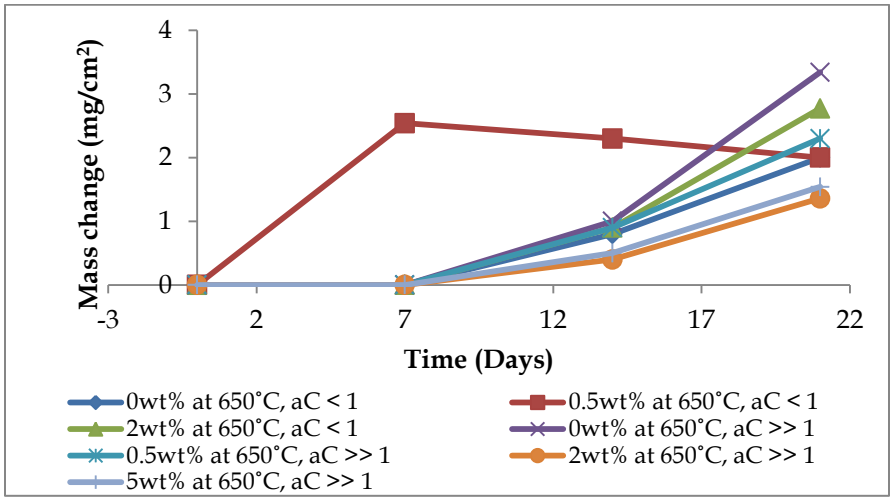


Figure 4.40: Shows the mass change of the ruthenium laser cladded 304L stainless steel.

(a) Mass change results after exposure to a_C < 1 atm

The samples exposed at 525°C did not undergo any mass change, whereas exposure of the ruthenium laser cladded samples to a low carbon activity containing environment at 650°C, resulted in the sample containing 0.5 wt.%Ru gaining a mass of 2.54 mg/cm² after seven days of exposure. After 21 days of exposure all the samples had gained mass except for the 5 wt.% Ru sample, as can be seen in Figure 4.40. An interesting observation was that there was a decrease in the mass gained by the 0.5 wt.% Ru sample after 21 days of exposure, whereas all the other samples gained more mass.

(b) Mass change results after exposure to a_C >> 1 atm

All the samples exposed at 650°C in an environment containing a carbon activity of 35 atm experienced a loss of mass after 21 days of exposure with the 0 wt.% sample losing the most mass of 3.34 mg/cm², followed by the 0.5 wt.% Ru sample losing 2.30 mg/cm², the 5 wt.% Ru sample and the 2 wt.% ruthenium samples losing 1.54 mg/cm² and 1.36 mg/cm², respectively. It was postulated that the 0 wt.% and 0.5 wt.% Ru samples lost the most mass due to general corrosion as opposed to pitting corrosion that occurred on the 2 wt.% and 5 wt.% Ru samples. It has to be emphasised that mass changes here were only used as an indication of the rate of corrosion rather than the actual rate of corrosion [16,17]. Additionally corrosion debris was not entirely removable on all samples, therefore this will affect the mass change measured.

4.4.2.2 Exposure to low carbon activity (a_C < 1 atm)

An FESEM investigation of the samples exposed at 525°C for seven days, show that all the samples formed a continuous oxide layer, Figure 4.41, with black deposits which were confirmed to be rich in carbon by EDS. No cracking or spalling of the oxide layer was observed on the surface of all the laser cladded samples and it stayed intact throughout. Hence the carbon deposited was not concentrated. The oxide layer also prevented the onset of metal dusting as no pitting was observed on any of the samples. The black deposits on the surface were almost entirely made up of carbon.

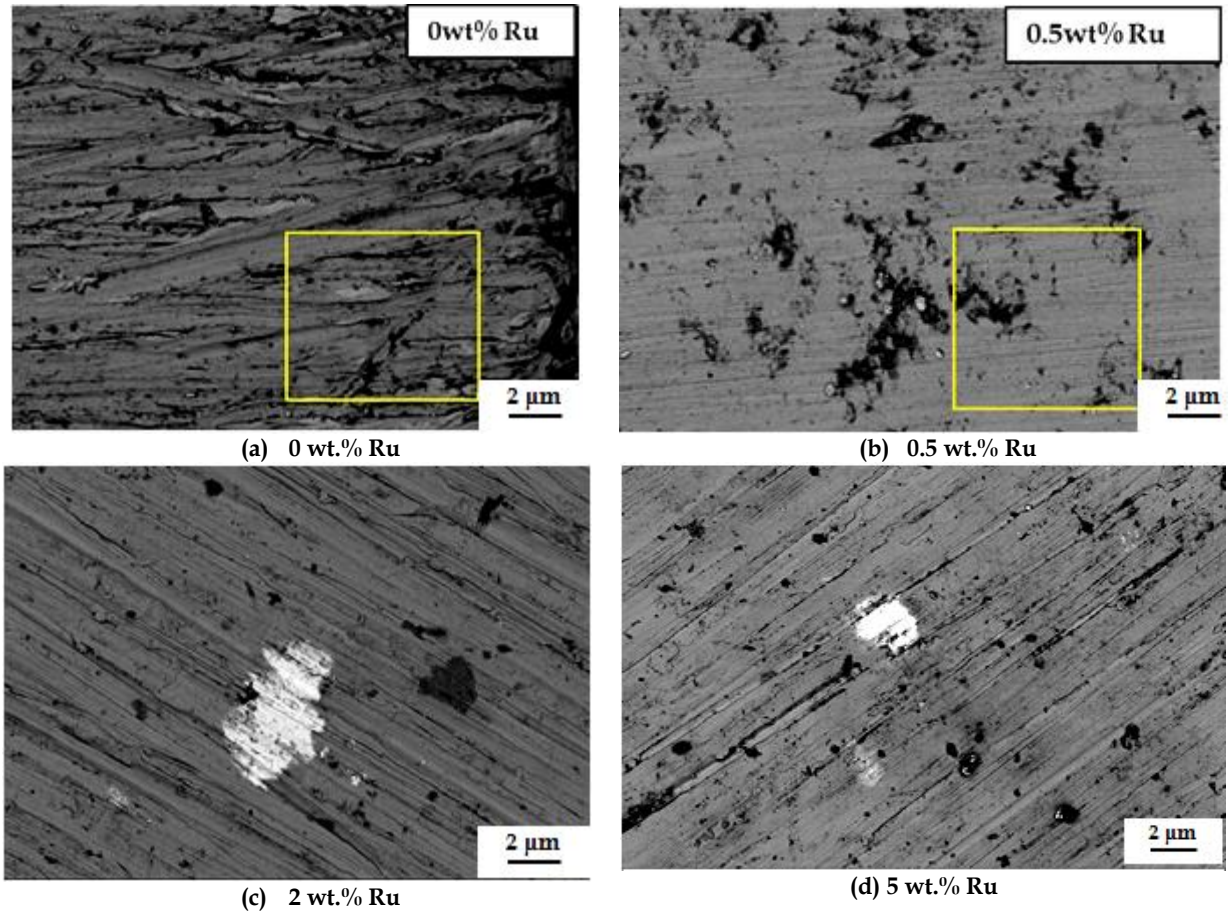
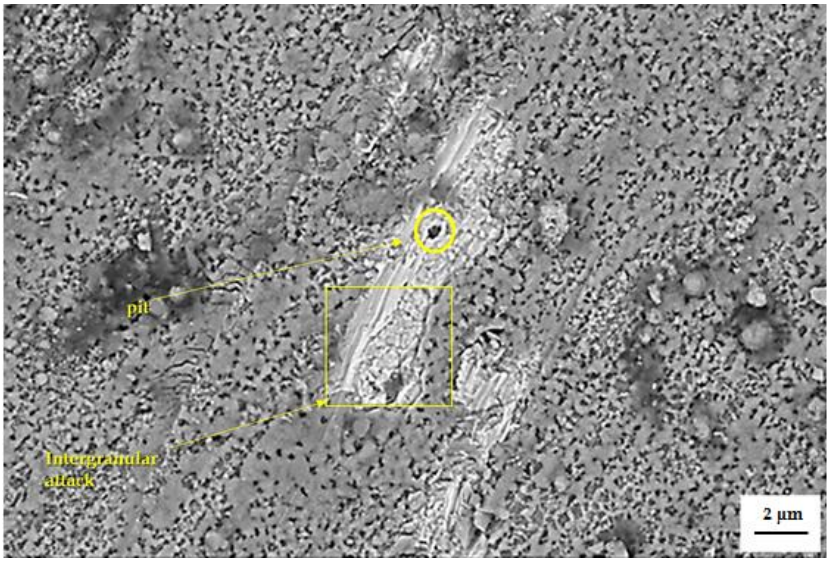
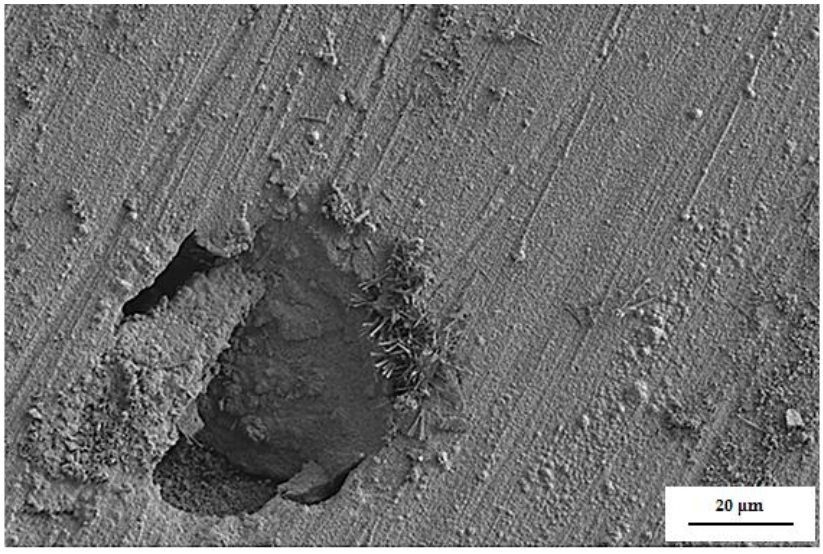


Figure 4.41: FESEM-BSE micrograph of (a) the 0wt% Ru, showing (b) the 0.5 wt.% Ru, (c) the 2 wt.% Ru and (d) 5 wt.% Ru of the oxide layer after seven days of exposure to a metal dusting environment at 525°C.

FESEM analysis showed that the samples had formed an oxide layer, which was meant to be protective against attack of the metal, however the oxide layer showed signs of spallation and cracking, Figure 4.42 (a). All the samples exhibited a spalled oxide layer. The 0 wt.% Ru sample even experienced pitting as, as highlighted in Figure 4.42 (b).



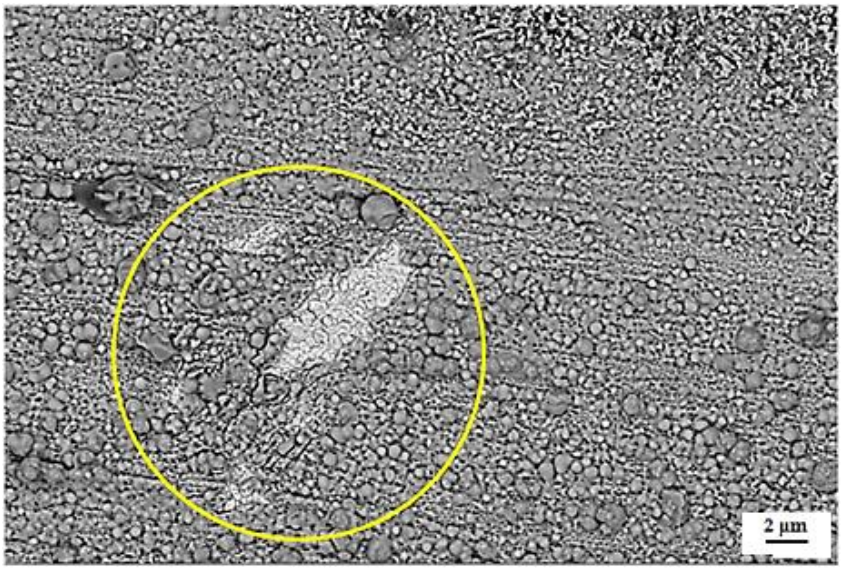
(a)



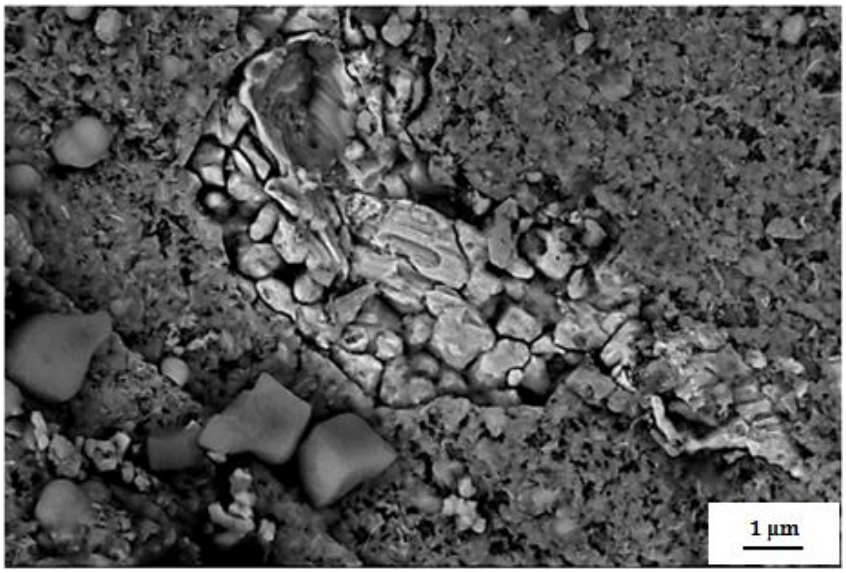
(b)

Figure 4.42: FESEM-BSE micrograph at of the 0 wt.% Ru, showing (a) shows the initiation of spalling of the oxide layer and (b) the spalled oxide, with pits and intergranular attack exposed at 650°C for seven days.

The 0.5 wt.% Ru sample showed the same degradation as the 0 wt.% Ru sample. The sample had a cracked and spalled oxide layer with some intergranular attack. However, the bare substrate on this sample was not pitted as shown in Figure 4.43 (a). The intergranular attack was much clearer in Figure 4.43 (b) and in the same image dislodging of grains from the microstructure as a result of this intergranular attack was observed.



(a)



(b)

Figure 4.43: FESEM-BSE micrograph at of the 0.5 wt.% Ru, showing (a) the spalled oxide, showing the substrate and (b) shows intergranular attack exposed to a metal dusting favourable environment at 650°C, for seven days.

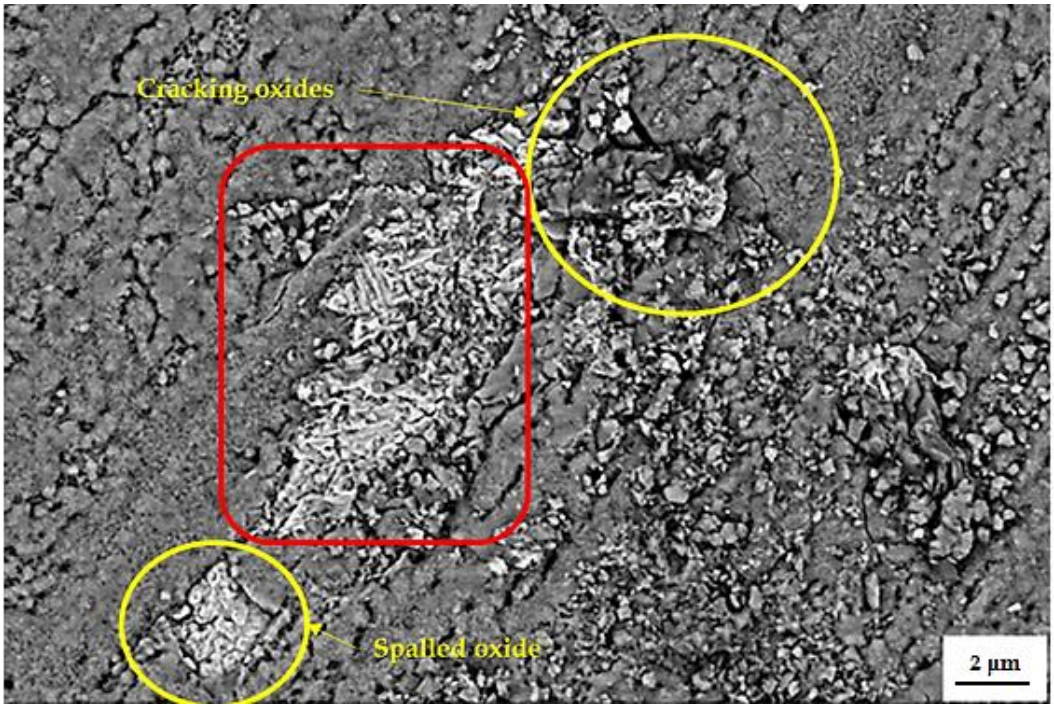


Figure 4.44: FESEM-BSE micrograph at of the 2 wt.% Ru, showing the cracked and spalled oxide, showing the substrate, intergranular attack and self-healing exposed to a metal dusting favourable environment at 650°C, for seven days.

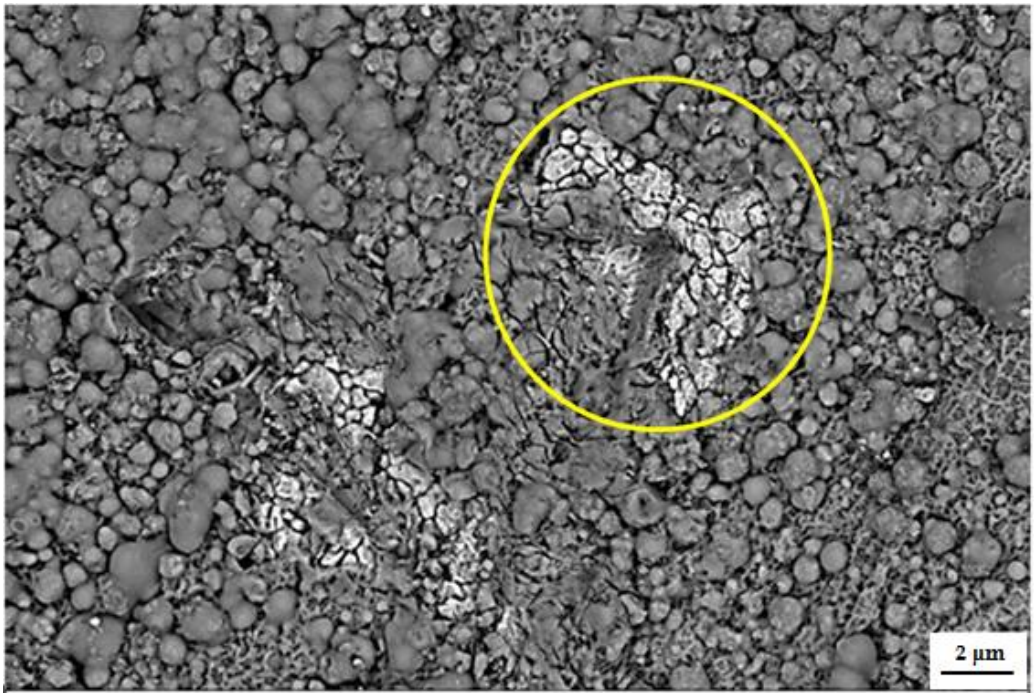


Figure 4.45: FESEM-BSE micrograph at of the 5 wt.% Ru, showing the spalled oxide, showing the substrate and intergranular attack exposed at 650°C, for seven days in a metal dusting favourable environment.

The oxide layer of the 0.5 wt.% Ru sample was rougher than the 0 wt.% Ru sample, due to more corrosion product particles on the surface of the 0.5 wt.% Ru sample. The 2 wt.% Ru sample shown in Figure 4.45, also experienced oxide spalling and cracking, where some intergranular attack was identified, however, it was not as pronounced as that seen on the 0 and 0.5 wt.% Ru samples. An interesting observation was the area highlighted in red in Figure 4.44, shows that though the oxide spalled there was some growth that occurred. This implies that the material may have been self-healing, growing another layer on the substrate. Intergranular features were identified in these regions.

Post exposure to 525°C for 21 days, FESEM analyses showed that all the samples formed an oxide layer where the 0 wt.% Ru, 0.5 wt.% Ru and 5 wt.% Ru samples formed the most adherent and continuous oxide layer, Figure 4.46.

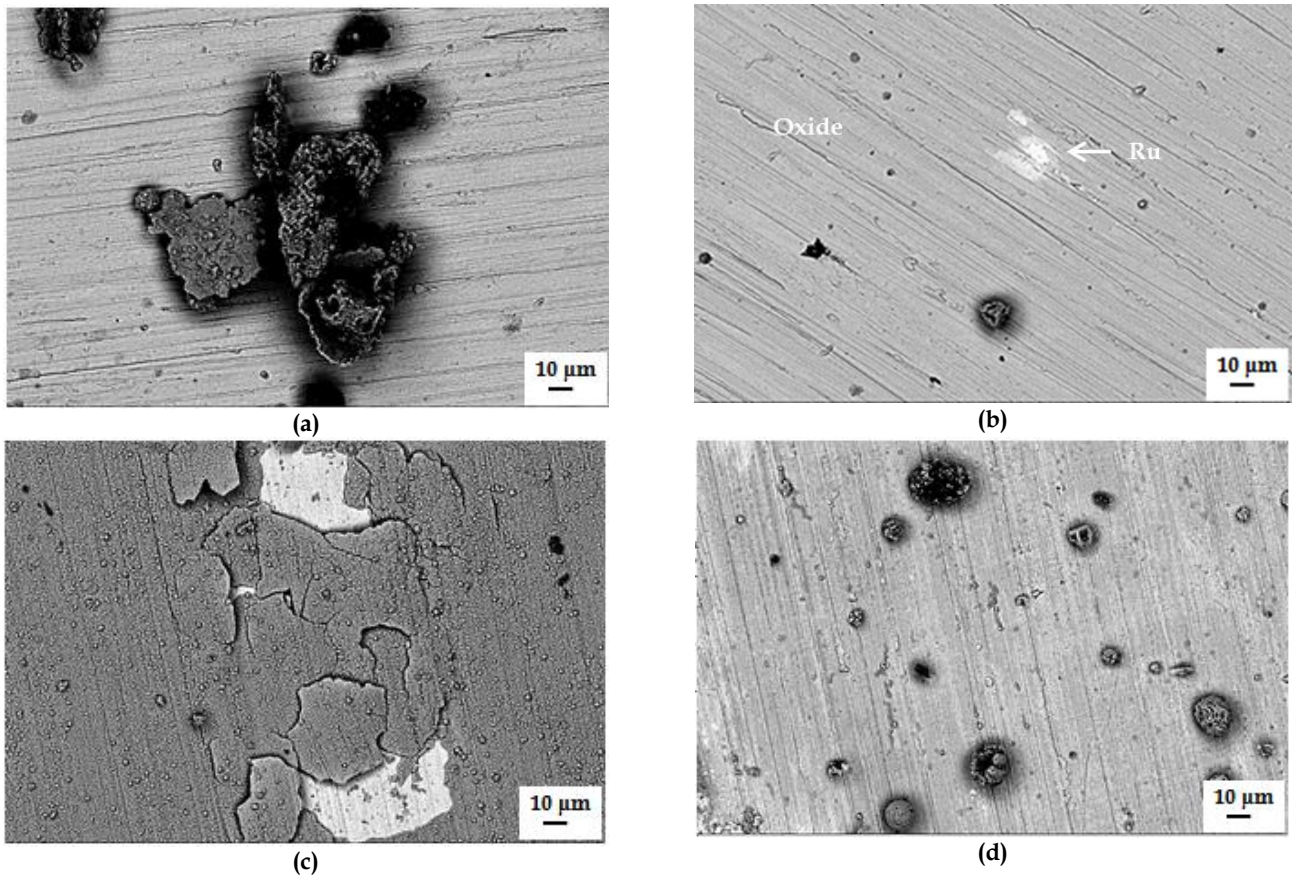


Figure 4.46: FESEM-BSE micrograph of (a) the 0 wt.% Ru, showing (b) the 0.5 wt.% Ru, (c) the 2 wt.% Ru and (d) 5 wt.% Ru of the oxide layer exposed to a metal dusting favourable environment at 525°C, for 21 days.

On the 0.5 wt.% Ru sample, the ruthenium was blended together with the oxide layer, Figure 4.46 (b), forming a homogeneous layer on the cladded surface. The EDS analysis of the samples show that the debris found is actually made up of oxide particles, for all the samples.

The 2 wt.% Ru sample performed the worst as the oxide layer spalled and the substrate was exposed to the gaseous environment. Figure 4.47, shows the bare substrate at higher magnification, revealing that the substrate underwent pitting as well as evidence of intergranular attack.

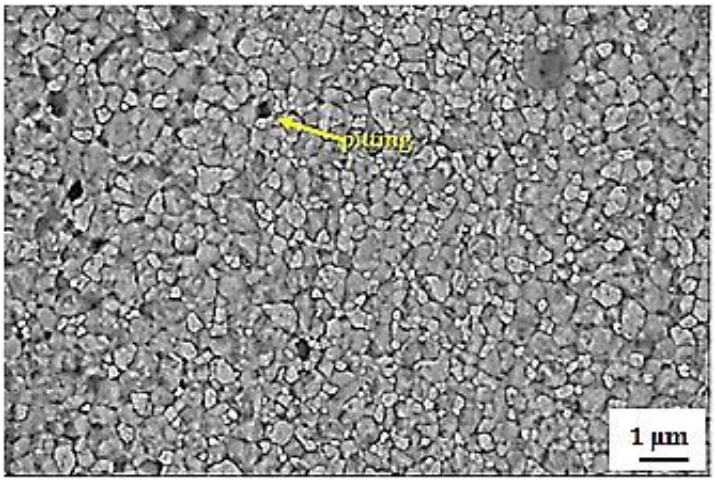


Figure 4.47: FESEM-BSE showing pitting and intergranular attack on the 304L substrate exposed at 525°C, for 21 days in a metal dusting favourable environment.

The Raman spectra results seen in Figure 4.48, indicate the presence of various chromite spinel oxides – a mixture of $(Fe,Ni)Cr_2O_4$, hematite and carbon was dominant in the majority of the ruthenium laser cladded samples, however, the 2 wt.% Ru sample was dominated by spinel oxides and carbon, with no hematite observed [17-24]. In addition to that no carbon was detected by the Raman spectrometer on the 0.5 wt.%. The carbon formed on the samples was graphitic in nature as the I_D/I_G ratio was approximately 1, in the range (0.98-1.49) [22-24]. This implies that with increasing exposure time, the samples became catalytic to crystalline carbon deposition.

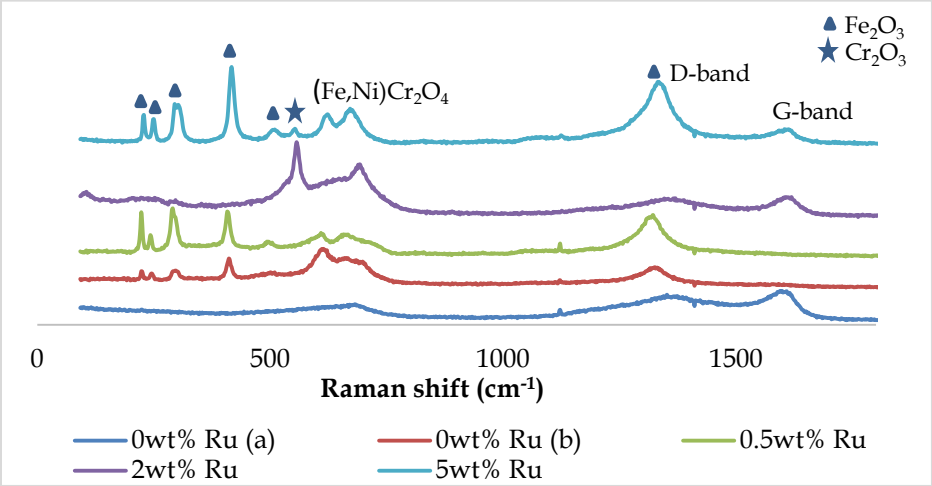


Figure 4.48: Raman spectra of the ruthenium laser cladded samples exposed for 21 days.

Figure 4.49 shows the GIXRD results which indicate the presence of the austenite phase on the surface, and a peak representative of hematite at approximately 53°. The cross-sectional analysis shows that an oxide layer did form over time and no internal cracking oxidation was observed on these samples, Figure 4.50.

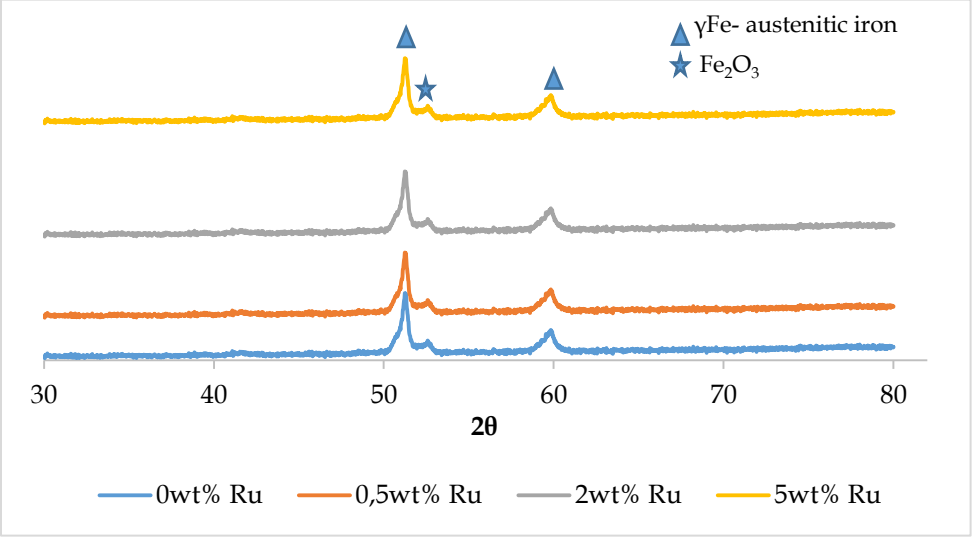


Figure 4.49: GIXRD spectra of the ruthenium laser cladded samples exposed for 21 days.

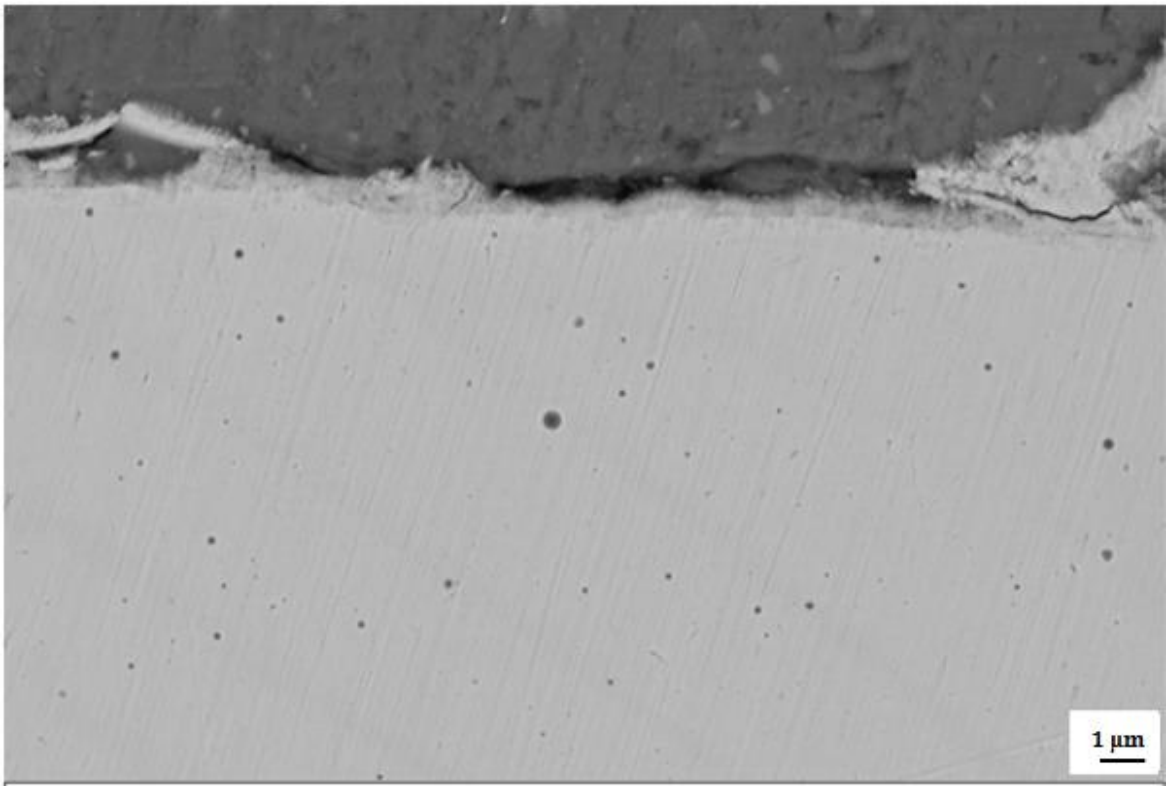
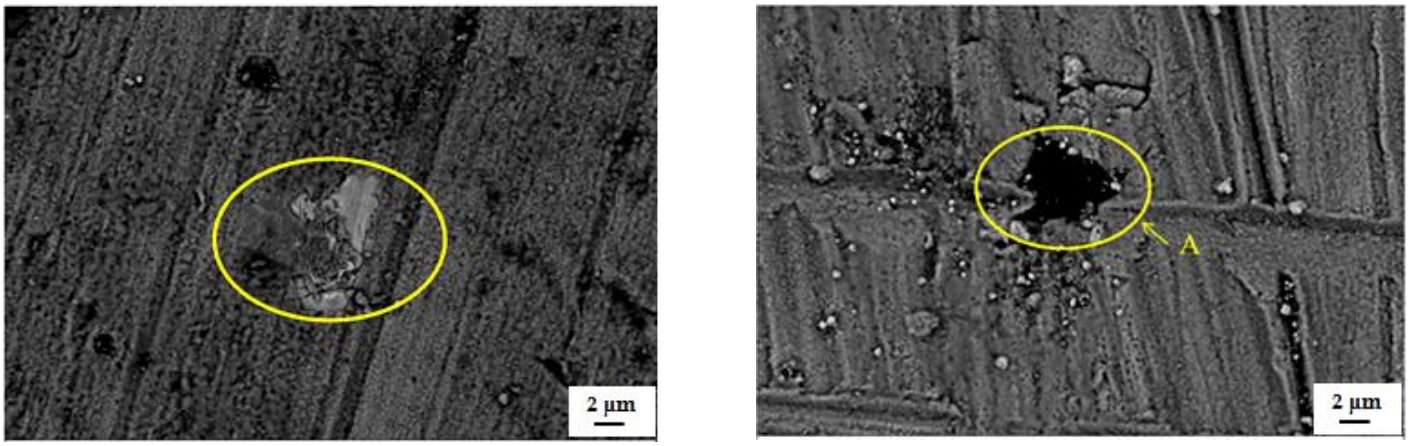


Figure 4.50: Typical FESEM-BSE of the cross-section of the laser cladded samples that have been exposed at 525°C for 21 days.

The surfaces of the samples exposed at 650°C for 21 days were investigated under FESEM, and showed that the samples all formed a continuous oxide layer. The oxide layers that formed on all of these samples appeared to be damaged.



(a) **(b)**

Figure 4.51: FESEM-BSE micrographs showing the oxide layer that formed after exposure at 650°C for 21 days, on the 0 wt.% Ru sample where (a) the oxide layer had spalled revealing the laser cladding (substrate) and, (b) the black particle growing into the oxide layer.

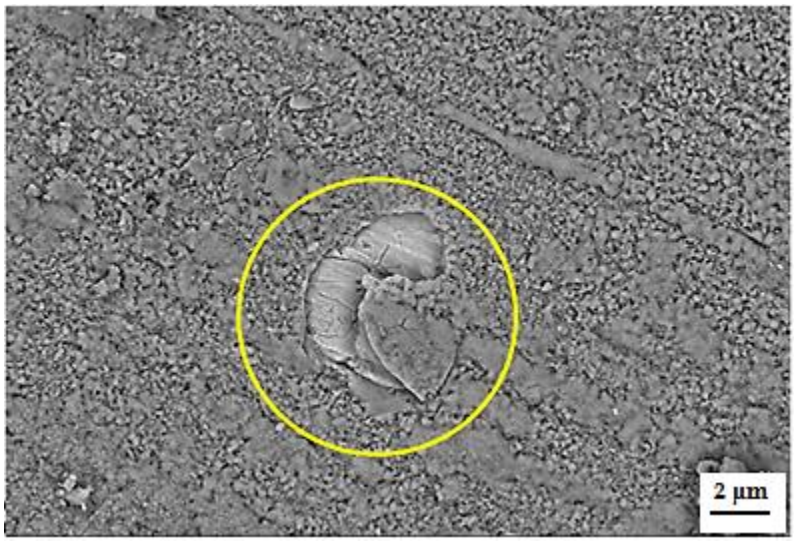
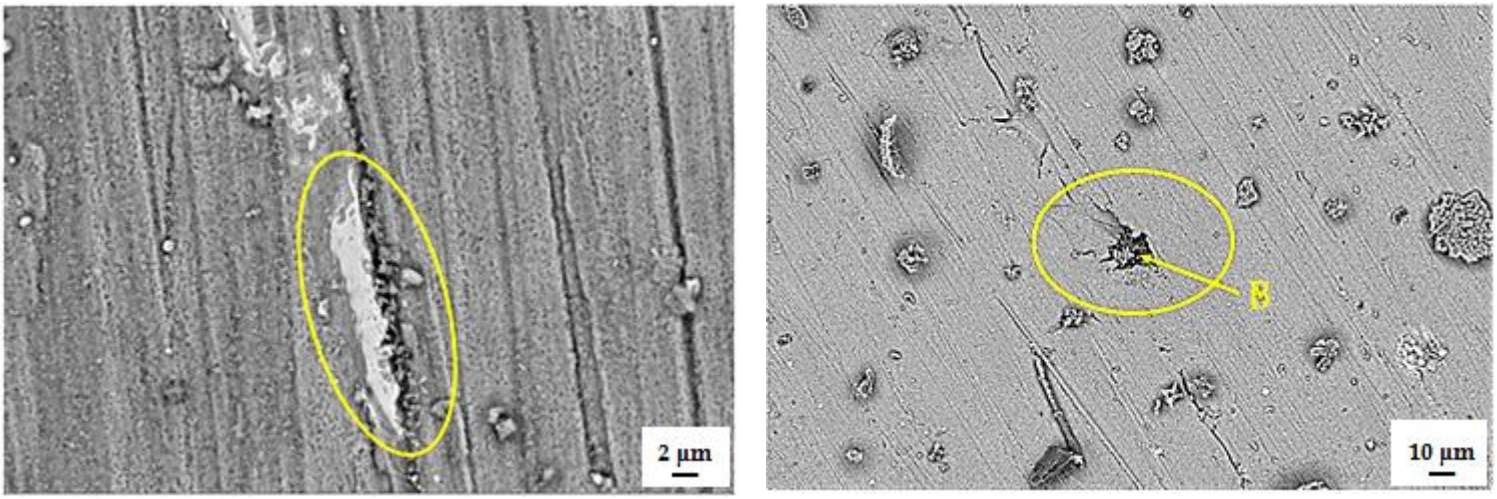


Figure 4.52: FESEM-BSE micrograph of the 0.5 wt.% Ru samples showing the spalling of the oxide layer formed after exposure at 650°C for 21 days.

There was minor spalling of the oxide as well as holes where corrosion growth formed on samples such as the 0 and 2 wt.% Ru samples as can be seen on Figure 4.52 and Figure 4.53. No significant carbon deposition was observed.

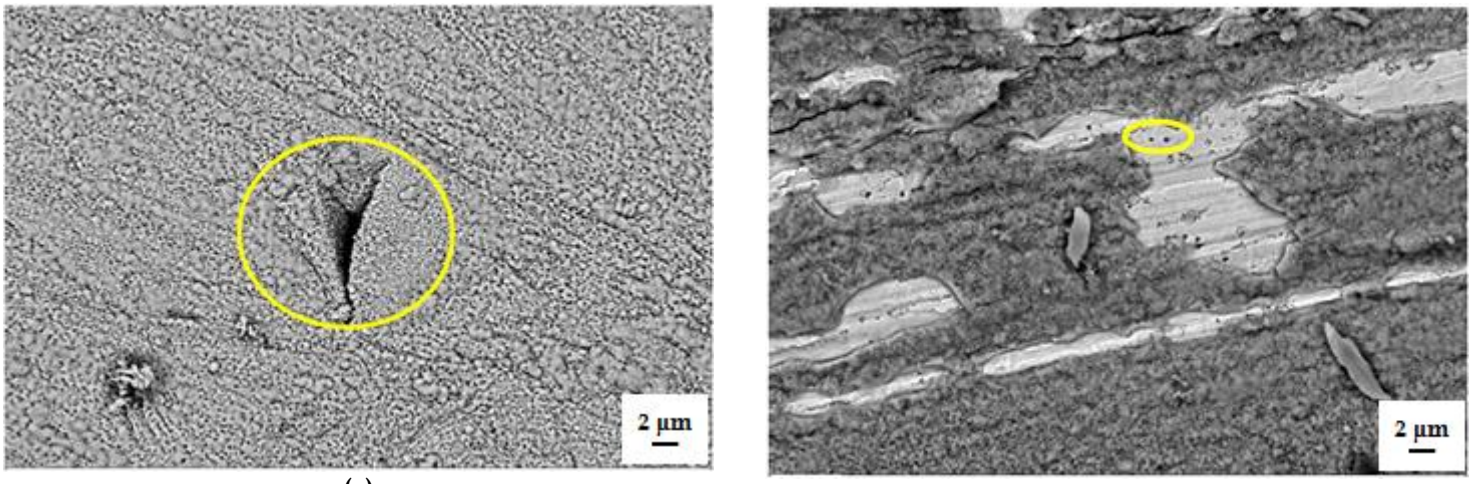


(a) **(b)**

Figure 4.53: FESEM-BSE micrograph of the 2 wt.% Ru samples showing (a) the spalling of the oxide layer formed, and (b) growths into the oxide layer.

The oxide layers formed on all the samples were damaged and where the laser cladding (substrate) was visible under it, the oxide had spalled. However, surprisingly the 5 wt.% Ru sample exhibited the largest damaged area and some shallow pits were visible, Figure 4.54 (b). In addition, carbon was deposited on some areas of this sample. A black

particle grew into the 0 and 2 wt.% samples, when analysed under EDS it was rich in carbon and silicon. This silicon is suspected to have diffused from the substrate to the surface during exposure.



(a) **(b)**

Figure 4.54: FESEM-BSE micrograph of the 5 wt.% Ru samples showing (a) depression in the oxide layer, and (b) the spalled oxide layer after exposure at 650°C for 21 days.

The Raman spectra shown in Figure 4.54, were diverse, the 0 and 0.5 wt.% samples formed a solid solution spinel of $(Fe,Ni)Cr_2O_4$, which is indicated by the broad peak from 640-770 cm^{-1}, peaking at 642 cm^{-1} at the rim of the chromite grain peak [16-20]. In addition, a non-solid solution $FeCr_2O_4$ that formed which peaked at 560 cm^{-1} and carbon indicated by the D-band at approximately 1351 cm^{-1} and 1600 cm^{-1} [17,18,22-24]. However, the carbon content varied with the 0 wt.% sample accumulating the lowest amount of carbon as shown by the relatively lower intensity carbon peaks. The nature of the deposited carbon was highly, ordered therefore graphitic in nature, with an average I_D/I_G ratio between 1.02 and 1.10 [22-24]. And the higher ruthenium containing samples (2 & 5 wt.% Ru) all formed hematite and minor amounts of carbon. The carbon formed was graphitic in nature.

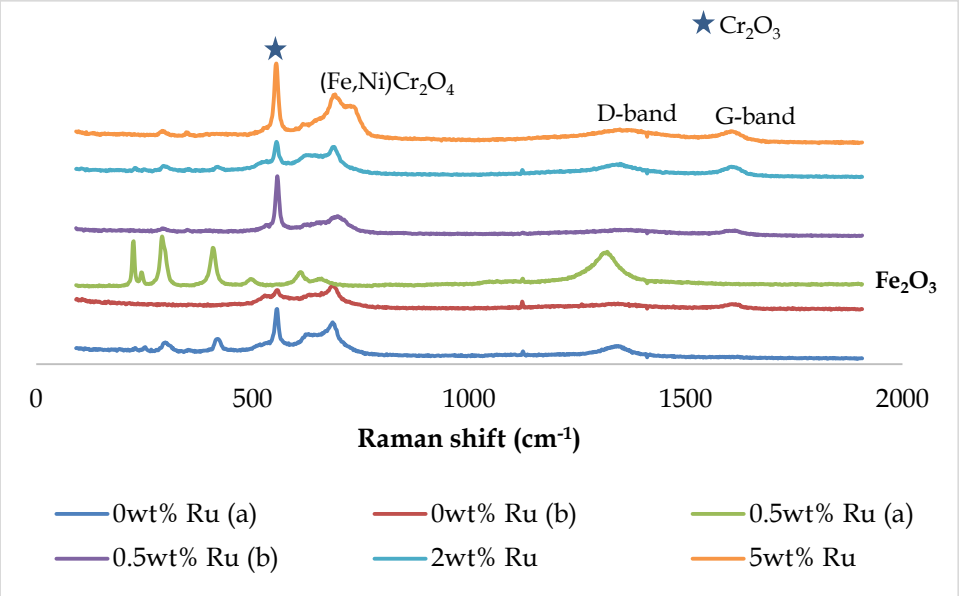


Figure 4.55: Raman spectra of the ruthenium laser cladded samples exposed at 650°C for 21 days.

The GIXRD results showed the presence of the austenitic phase and a shallow peak at 53° indicating the presence of hematite as shown in Figure 4.55. The 0.5 wt.% and 2 wt.% Ru samples did not show much as the hematite peaks were very shallow with low intensities. This result implies that hat the oxide layer formed was relatively thin as was in the cross-section analysis in micrograph Figure 4.57.

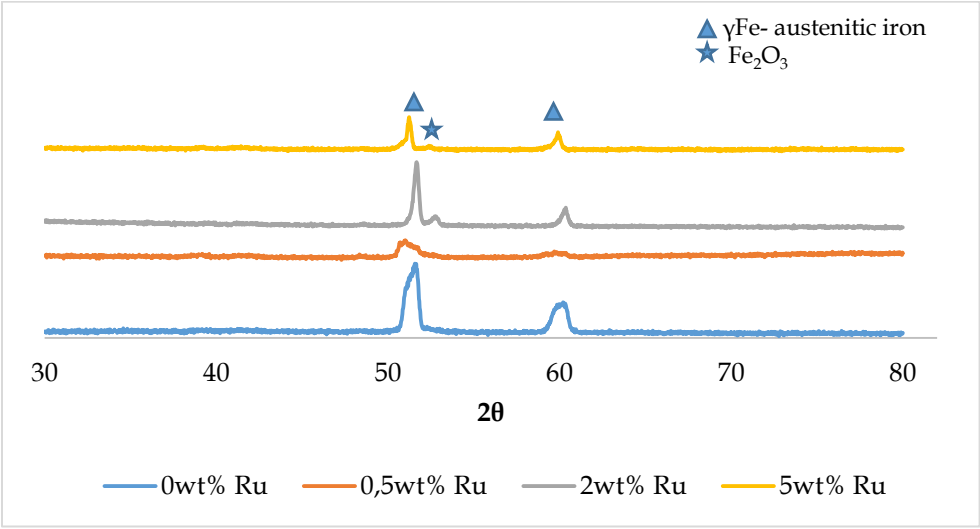


Figure 4.56: GIXRD spectra of the ruthenium laser cladded samples exposed for 21 days.

The cross-section analysis of these samples did not show any surface or subsurface damage on these samples. The cross-section images of the 0-5 wt.% Ru samples were very similar in that they showed an uneven surface oxide that formed and the silicon – carbon rich growth was common in all these samples, a representative image is shown in Figure 4.57.

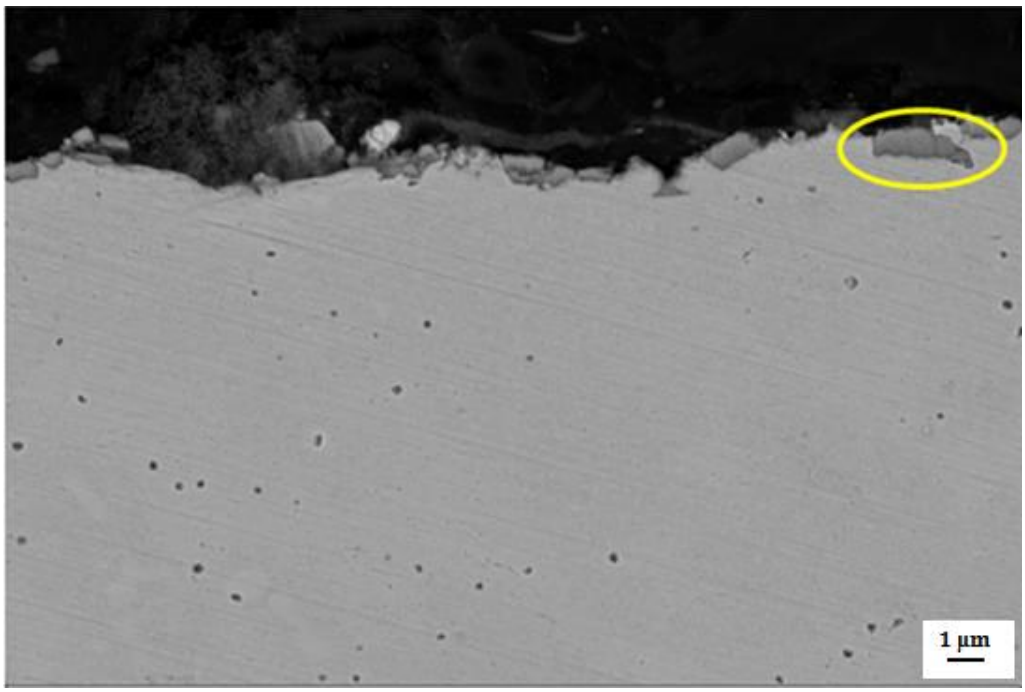
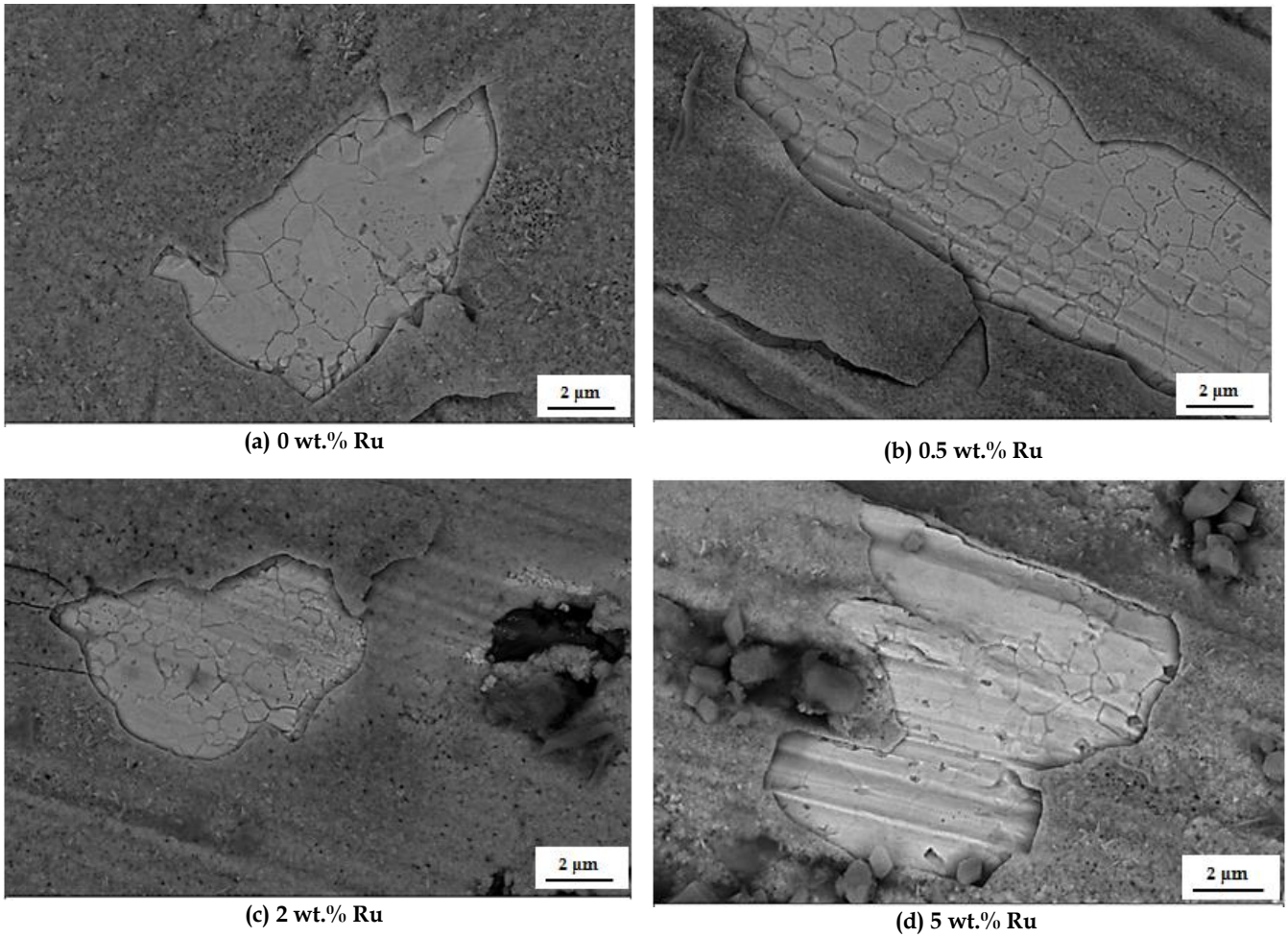


Figure 4.57: Typical FESEM-BSE of the cross-section of the laser cladded samples that have been exposed at 650°C for 21 days, showing carbon growths into the laser clad.

4.4.2.3 Exposure to high carbon activity (aC >> 1 atm)

After seven days of exposure all the laser cladded samples experienced attack by pitting or spalling of the oxide, which ended the metal dusting incubation period, and resulted in the initiation of metal dusting.

All samples were in the initiation stage of metal dusting, as the surface analysis showed a spalled oxide where the revealed substrate consisted of shallow pits and features of intergranular attack as shown in Figure 4.58.



(a) 0 wt.% Ru **(b) 0.5 wt.% Ru**

(c) 2 wt.% Ru **(d) 5 wt.% Ru**

Figure 4.58: FESEM-BSE micrograph of the (a) 0 wt.% Ru and (b) 0.5 wt.% Ru (c) 2 wt.% Ru and (d) 5 wt.% Ru samples revealing the spalling of the oxide layer and the shallow pits formed exposed at 650°C, for seven days with a_C of 35 atm.

Additionally, the 5 wt.% Ru sample also exhibited pitting with relatively larger pits. However, the pits on this sample retained corrosion product and the corrosion product was presumed due to its black colour, to be solid carbon that has been deposited onto the surface of the sample, as shown in Figure 4.59.

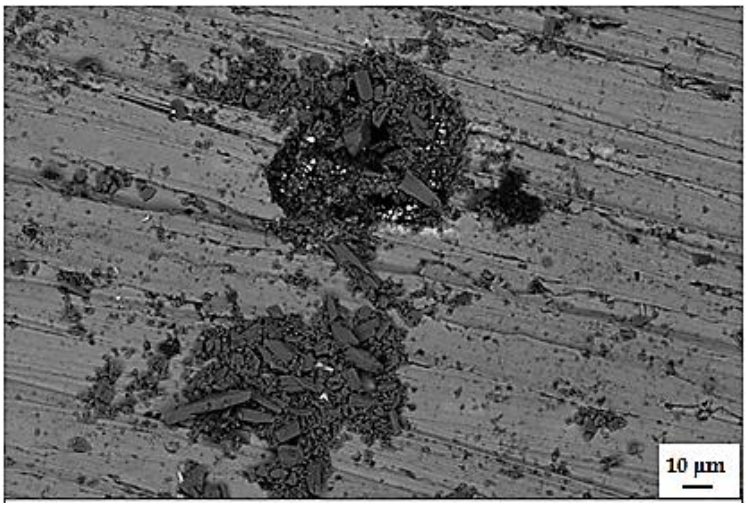
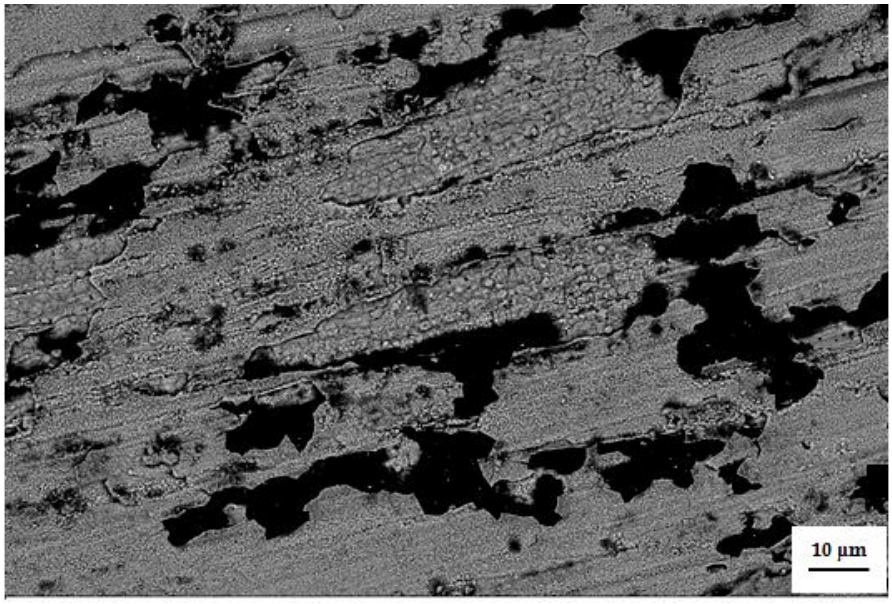
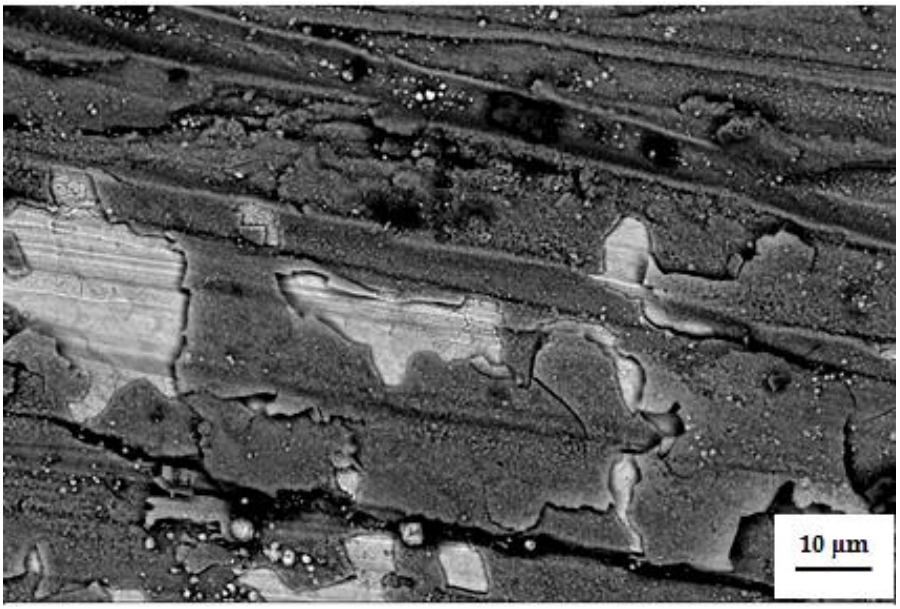


Figure 4.59: FESEM-BSE micrograph showing the 5 wt.% Ru sample with a pit filled with corrosion debris, formed after exposure at 650°C, for seven days in a carbon activity of 35 atm.

After 21 days of exposure all the laser cladded samples experienced attack. The lower ruthenium containing samples, exhibited the same behaviour as they did when exposed for seven days, where the oxide spalled and there were small pits forming on the substrate with initiation of intergranular attack on the surface as shown in Figure 4.60. Additionally, there were carbon deposits on the exposed substrate. Whereas the higher ruthenium containing samples had experience attack that was characterised by deep pits and the pits were large in diameter of 90 µm and greater. The pit diameter increased with increasing ruthenium content as shown in Figure 4.61. FESEM further confirmed that the areas enriched with ruthenium were points of initiation for pitting and EDS analysis showed that there was ruthenium in the pits. Carbon deposited in the pits and is characterised by the black corrosion products in the pits.

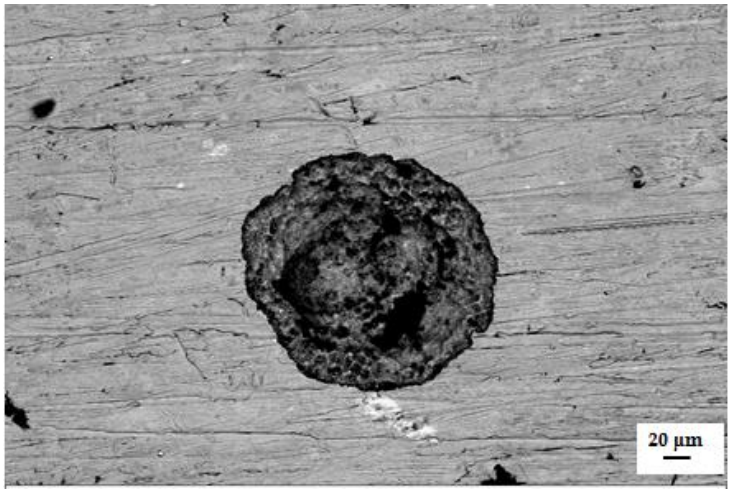


(a) 0 wt.% Ru



(b) 0.5 wt.% Ru

***Figure 4.60**: FESEM-BSE micrograph of the (a) 0 wt.% Ru and (b) 0.5 wt.% Ru samples revealing the spalling of the oxide layer formed and carbon deposits after exposure at 650°C, for 21 days in a carbon activity of 35 atm.*



(a) 2 wt.% Ru



(b) 5 wt.% Ru

Figure 4.61: FESEM-BSE micrograph of the (a) 2wt% Ru, (b) 5 wt.% Ru samples revealing the corrosion pits after exposure at 650°C, for seven days in a carbon activity of 35 atm.

Further analysis of the samples using Raman spectroscopy as shown in Figure 4.62, revealed that formed solid solution spinel of $(Fe,Ni)Cr_2O_4$ which is indicated by the broad peak from 640-770 cm^{-1}, peaking at 642 cm^{-1} at the rim of the chromite grain peak. There was also non-solid solution $FeCr_2O_4$ that formed and was peaking at 560 cm^{-1} [17-21]. Raman analysis showed the presence of graphitic carbon. The nature of the carbon formed was highly ordered therefore graphitic with an average I_D/I_G ratio between 1.00 and 1.02 [22-24].

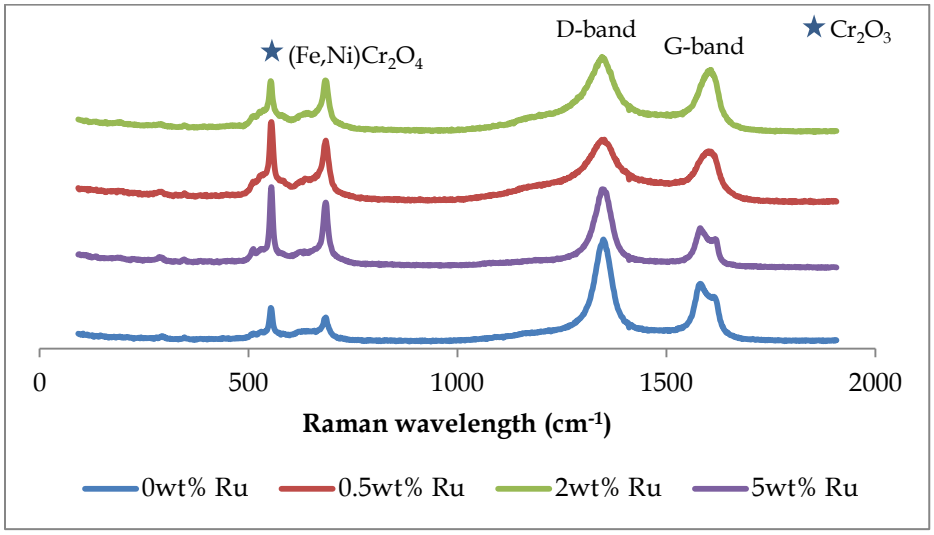


Figure 4.62: Raman spectra of the ruthenium laser cladded samples exposed for 21 days after exposure at 650°C, for 21 days in a carbon activity of 35 atm.

Low intensity hematite peaks were evident below 500 cm^{-1}, on the Raman spectra obtained for the 0 and 0.5 wt.% Ru samples, which resulted in the shoulder observed at the G-band, this shoulder formed due to the hematite peak that is found at approximately 1600 cm^{-1}.

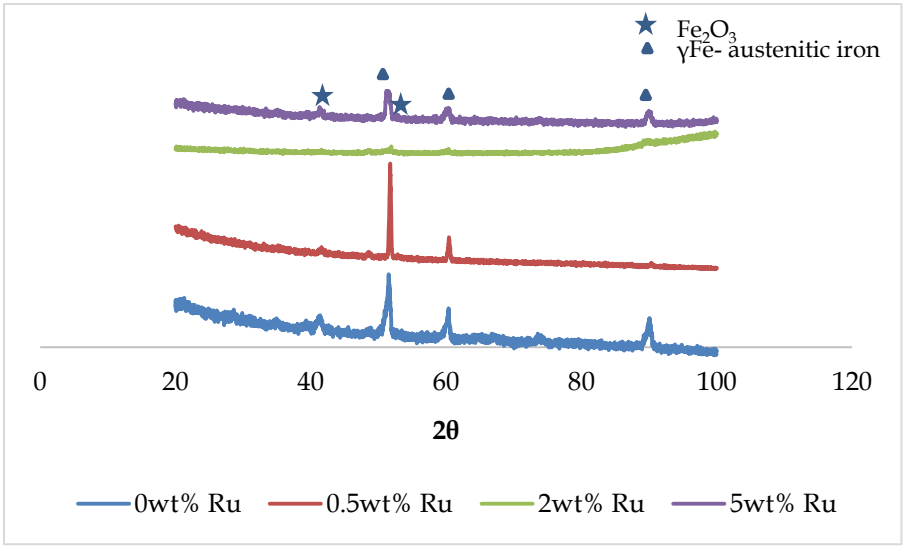
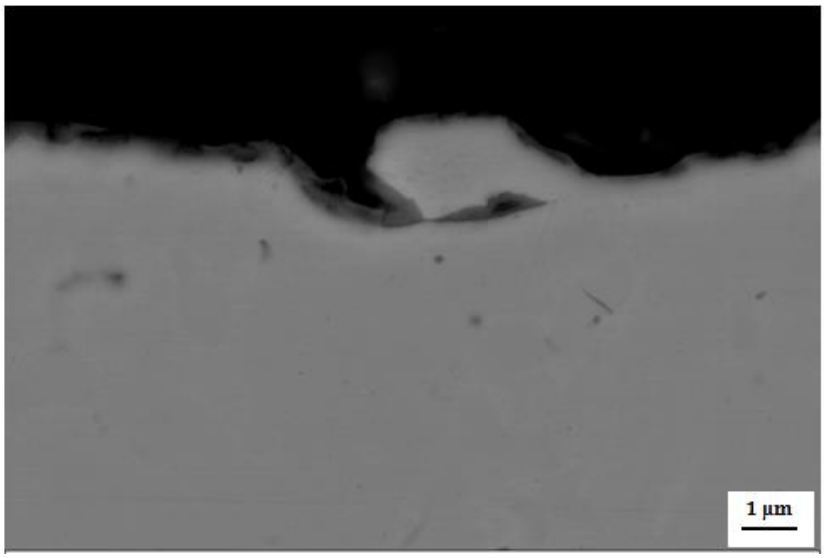
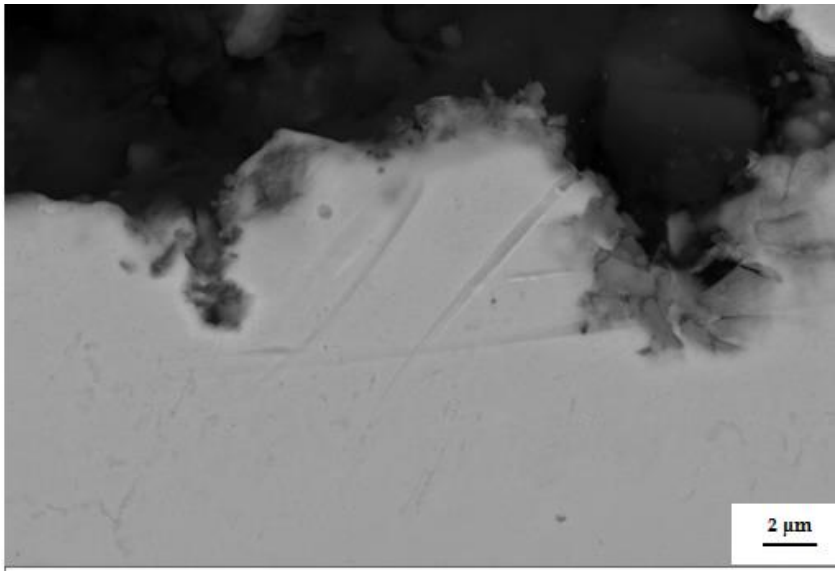


Figure 4.63: GIXRD spectra of the ruthenium laser cladded samples exposed for 21 days at 650°C, with a_C = 35 atm.

Figure 4.63 presents the GIXRD spectra which indicates the presence of the austenitic phase and hematite at 41˚ and 53˚.



(a)



(b)

Figure 4.64: Typical FESEM-BSE of the cross-section of the laser cladded samples that have been exposed at 650°C for 21 days (a) showing cracks and oxidation and (b) shows the cross-section of the pits.

The cross-sectional analysis confirms that the oxide formed was relatively thin as it cannot be seen. Additionally the cross-section showed cracks along the surface as shown in Figure 4.64 (a) and it can also be observed how irregular the surface showing the cross-section of the pits in Figure 4.64 (b).

4.4.3 Discussion

The results after exposure at 525°C indicate that the laser cladding was beneficial in slowing down metal dusting as it promoted the formation of a continuous, dense and protective oxide layer on all the samples. The promotion of the oxide layer formation was attributed to grain refinement of the laser cladding, which increased chromium diffusion paths, along the grain boundaries. This indicated that the original formation of the oxide layer was a rapid process which inhibited corrosive species to diffuse into the substrate and cause detriment to neither the oxide layer nor the substrate. Therefore, the materials have a high self-healing ability.

Exposure at 650°C indicated that the laser cladded samples were highly susceptible to metal dusting since on all the samples the oxide spalled just after seven days of exposure at all carbon activities. Not only did oxide spall off, but intergranular attack and pitting occurred; implying that the samples did not self-heal effectively, when exposed to the corrosive gaseous environment. At lower carbon activities the pitting incubation period was longer than for the high carbon activity containing environment. This was expected seeing that all the samples exposed to the high carbon gas activity environment catalysed graphitic carbon formation and this type of carbon was the most detrimental in metal dusting environments as it causes volume expansion leading to fragmentation of the material into small dust particles [25-27].

At 650°C the laser cladded samples showed the same damage, or worse than the unmodified 304L stainless steel. Therefore, the ruthenium and laser cladding did not add any protection at this temperature, at both the a_C = 0.67 atm and a_C = 35 atm, even after only seven days of exposure, because all the samples showed spalling of the oxide and minor pits. It was expected that metal dusting would initiate and pitting would occur on the laser cladding, but this was not the case in the lower carbon activity environment. This was attributed to the low carbon activity and relatively higher oxygen partial pressure, which resulted in a less aggressive environment. The low carbon activity and possibly the presence of the ruthenium reduced the rate at which

graphite was formed, and therefore, resulting in reduced volume expansion of the material, hence the lengthy incubation period of metal dusting. Ruthenium has been found to enhance the formation of the protective oxide layer in Fe-Cr alloys exposed to high temperature gaseous environments. The continuous oxide was due to the selective oxidation of chromium because of the high chromium affinity for oxygen. The selective oxidation of chromium is further accelerated by the presence of ruthenium, because ruthenium slows down the diffusion of iron by clearing the way for the diffusion of chromium and blocking the diffusion of the iron [28-30].

Ruthenium has the ability to catalyse carbon deposition, in carbonaceous gas environments. It often catalyses armophous carbon, which results in relatively low detriment in metal dusting environments and catalyses graphitic carbon in the presence of a catalyst such as SiO_2 or graphite [31-33]. This deposition of amorphous carbon by the ruthenium therefore minimises and slows down the metal dusting process because for metal dusting to occur, highly crystalline graphite was required for volume expansion, resulting in the disintegration of the substrate; this, however, was not the case in this work. Ruthenium was resistant to carburisation and its ability to catalyse chromium oxide formation results in improved protection of the substrate against metal dusting, therefore increasing the incubation period of metal dusting [34,35].

The relatively higher oxygen partial pressure, with the aid of the ruthenium and the chromium diffusion paths induced by grain refinement, promoted the formation of the oxide layer, including chromites, which are protective. Furthermore, it was suspected that the self-healing of the oxide layer occurred, and was evidenced by the presence of the chromite mixture, since no significant pitting and spalling were observed even after 21 days of exposure [36-38]. Therefore a combination of laser cladding, low ruthenium additions, and low carbon activity were able to slow down metal dusting on 304L stainless steel, in contrast to the work done by De Bruyn [39] who found 304L stainless steel to show metal dusting at 650^{o}C even at a carbon activity of 0.28 atm. Although this temperature was highly conducive for metal dusting there was no sub-surface

degradation or internal oxidation implying that the laser cladded samples were in the incubation stage rather than under metal dusting attack. Furthermore, when the cross-section of the samples was analysed, it was found that the samples had formed carbides, which are only a pre-cursor of metal dusting [40,41].

The higher ruthenium containing samples exhibited signs of low resistance to metal dusting, where the 5 wt.% ruthenium sample exhibited the largest area of oxide spallation and many minor pits. Additionally both the 2 and 5 wt.% ruthenium containing samples formed hematite and a porous oxide, which is not protective. The porosity of the oxide exposes the fresh metal underneath it to the corrosive gases subsequently, accelerating carbon deposition and possible graphite formation, which would accelerate metal dusting [41-43]. However, was suspected that this effect would only be realised after longer exposure periods.

The samples exposed to the higher carbon activity (35 atm) showed a distinct difference in behaviour. After just seven days of exposure they showed pitting on the exposed substrate and after 21 days of exposure the samples formed large, distinct pits particularly on the higher ruthenium (2 and 5 wt.% Ru) containing samples. This behaviour was attributed to ruthenium being able to catalyse graphitic carbon that caused pitting, and as a result metal dusting occurred as the pitting initiated at areas enriched with ruthenium. Higher ruthenium content increased the pit size. At 650^{o}C and high carbon activities with relatively low oxygen partial pressures ruthenium accelerated the metal dusting process since it catalysed graphite formation, as evidenced by the carbon formed on these samples [15,44]. In relatively pure hydrogen-carbon monoxide mixtures, hydrogen was highly catalytic to carbon deposition as a result it was postulated that in the high carbon activity environment (a_C = 35 atm), hydrogen contributed to the rapid growth in the pits [15].

It was also postulated that the low ruthenium content (wt.% Ru < 2 wt.%) was potentially beneficial. Since the ruthenium was able to form a single phase with the

304L stainless steel or in cases where the ruthenium was not dissolved, the ruthenium would form a homogeneous coating with the oxide formed during exposure to a metal dusting environment. The single phase did not contain areas enriched with ruthenium which in the presence of 304L were able to catalyse graphitic carbon deposition. The resultant grain refinement due to laser cladding and/or the addition of ruthenium improved the metal dusting incubation period.

4.4.4 Summary

The behaviour of laser cladded stainless steel 304L was studied. The stainless steel was cladded with 304L stainless steel powder and varied ruthenium concentrations of 0, 0.5, 2 and 5 wt.%, in two gaseous environments containing carbon activities of 0.51, 0.67 and 35 atm. It was found that at the low carbon activities all the samples experienced a prolonged metal dusting incubation period, but did form carbides, though some were only visible along the cross-section. Even after 21 days of exposure the samples had not shown extensive pitting but metal dusting was initiating. Additionally, the presence of chromites and the lack of progressed pitting is evidence of self-healing of the laser cladded samples.

In the high carbon activity environment, it was found that the samples with a high ruthenium (2 and 5 wt.% Ru) contents were not effective in protecting 304L stainless steel against metal dusting attack, especially at the areas where the surface was enriched with ruthenium. Laser cladding coupled with a low ruthenium content have the potential to prolong metal dusting as they result in an increased metal dusting incubation period.

4.4.5 References

1. P. Nash, The Ni-Ru (nickel-ruthenium) system, Bulletin *of Alloy Phase Diagrams*, vol. 7, pp. 130-132, (1986).
2. S. Hallström, Thermodynamic assessment of the Ni-Ru system, *ASM International- Section 1: Basic and Applied Research*, vol. 25, pp. 252-254, (2004).
3. P. Franke and D. Neuschütz, Scientific Group Thermodata Europe (SGTE) () Fe-Ru (Iron - Ruthenium). In: Franke P., Neuschütz D. (eds) Binary Systems. Part 5: Binary Systems Supplement 1. Landolt-Börnstein - Group IV Physical Chemistry (Numerical Data and Functional Relationships in Science and Technology), *Berlin- Heidelberg*,*Springer*, vol. 19B5, pp.1-5, (2007).
4. O.O. Adenike, Heat treatment and corrosion behaviour of 2101 duplex stainless steel cathodically modified with ruthenium, PhD thesis, *University of the Witwatersrand*, South Africa, (2014).
5. M.A. Guitar, Design of new protective systems based on the intermetallic compound RuAl, PhD thesis, *University of Saarland*, Germany, (2014).
6. K. T. Voisey, Z. Liu, and F. H. Stott, Inhibition of metal dusting of Alloy 800H by laser surface melting, *Applied Surface Science*, vol. 252, pp. 3658–3666, (2006).
7. M. B. Lekala, J. W. Van Der Merwe, and S. L. Pityana, Laser surface alloying of 316l stainless steel with Ru and Ni mixtures, *International Journal of Corrosion*, vol. 2012, pp. 1–5, (2012).
8. S. G. Bratsch, Standard Electrode Potentials and Temperature Coefficients in Water at 298.15K, *Journal of Physical and Chemical Reference Data,* vol. 18, pp. 1– 21,(1989).
9. N. Hodnik, P. Jovanovic, A. Pavlisič, B. Jozinovic, M. Zorko, M. Bele, V.S. Selih, M. Sala, S. Hocevar and M. Gaberscek, New insights into corrosion of ruthenium and ruthenium oxide nanoparticles in acidic media, *Journal of Physical Chemistry C*, vol. 119, pp. 10140−10147, (2015).
10. *http://nickelinstitute.org/~/Media/Files/TechnicalLiterature/Types304and304LStainlessSteelsforLowTemperatureService_328_.pdf#page=* (Last accessed, 15 October 2018) Low Temperature Data Sheet of Stainless Steels, Types 304 and 304L
11. S. Toyserkani, E. Khajepour, and A. Corbin, Laser cladding, First Edition, *Washington D.C, CRC Press LLC*, pp. 1-5, (2005).

12. E.S.M. Sherif, J.H. Potgieter, J.D. Comins, L. Cornish, P.A. Olubambi, and C.N. Machio, The beneficial effect of ruthenium additions on the passivation of duplex stainless steel corrosion in sodium chloride solutions, *Corrosion Science*, vol. 51, pp. 1364–1371, (2009).
13. D. R. Askeland, The science and engineering of materials, Third. *Cheltenham: Stanley Thornes Ltd*, (1996).
14. R. H. Hertzberg, Deformation and fracture mechanics of engineering materials, Fourth. *New York: Wiley Coperations*, (1996).
15. A. Karjalainen, L.P. Taulavouri, T. Sellman, M. Kyrolaine, Some strengthening methods for austenitic stainless steels, *Journal of Materials Research and Technology*, vol. 79, pp. 404–412, (2008).
16. P. Szakálos, Mechanisms of metal dusting, *PhD thesis, Royal Institute of Technology Stockholm*, Sweden, (2004).
17. K. Natesan and Z. Zeng, Development of materials resistant to metal dusting degradation, *Final report, Nuclear Engineering Division, Argonne National Laboratory*, pp. 39-44, (2007).
18. H. Singh, D. Puri, S. Prakash and Rabindranath Maiti. Characterization of oxide scales to evaluate high temperature oxidation behavior of Ni-20Cr coated superalloys, *Materials Science and Engineering A,* vol. 464, pp. 110–116, (2007).
19. A. Wang, K.E. Kuebler, B.L. Jolliff and L.A. Haskinj, Raman spectroscopy of Fe-Ti-Cr-oxides, case study: Martian meteorite EETA79001, *American Mineralogist*, vol. 89, pp. 665–680, (2004).
20. B. J. Reddy and R. L. Frost, Spectroscopic characterization of chromite from the Moa-Baracoa Ophiolitic Massif, Cuba, *Spectrochimica Acta Part A*, vol. 61, pp. 1721–1728, (2005).
21. M. Da Cunha Belo, M. Walls, N. E. Hakiki, J. Corset, E. Picquenard, G. Sagon and D. Nöel, Composition, structure and properties of the oxide films formed on the stainless steel 316L in a primary type PWR environment. *Corrosion Science*, vol. 40, pp. 447–463, (1998).
22. D. Renusch, B. Veal, K. Natesan and M. Grimsditch. Transient oxidation in Fe-Cr-Ni alloys: A Raman-scattering study, *Oxidation of Metals*, vol. 46, pp. 365–381, (1996).
23. Z. Zeng, K. Natesan and V.A. Maroni, Investigation of metal-dusting mechanism in Fe-base alloys using Raman spectroscopy, X-ray diffraction and electron microscopy, *Oxidation of Metals*, vol. 58, pp. 147-170, (2002).

24. Z. Zeng and K. Natesan, Relationship between the growth of carbon nano-filaments and metal dusting corrosion, *Journal of the American Chemical Society*, vol. 17, pp. 3794-3801, (2002).
25. A.C. Ferrari and J. Robertson, Interpretation of Raman spectra of disordered and amorphous carbon, *Physical Review B*, vol. 61, pp. 14095-14107, (2000).
26. C. M. Chun, J. D. Mumford, and T. A. Ramanarayanan, Mechanisms of Metal Dusting Corrosion of Iron, *Journal of the Electrochemical Society*, vol. 149, pp. B348-B355, (2002).
27. H. J. Grabke, R. Krajak, and J. C. Nava Paz, On the mechanism of catastrophic carburization: 'metal dusting', *Corrosion Science*, vol. 35, pp. 1141–1150, (1993).
28. A. Schneider and H. J. Grabke, Effect of H_2S on metal dusting of iron, *Materials and Corrosion*, vol. 54, pp. 793–798, (2003).
29. M.J. van Staden, and J.P. Roux, Surface segregation in the alloys Fe-40Cr-3Ru, Fe-40Cr-3Pt and Fe-40Cr with a 1000 Å Pt, *Applied Surface Science*, vol. 44, pp. 271–277, (1990).
30. M.J. Van Staden, and J.P. Roux, The controlled oxidation of the high chromium steel alloys Fe40Cr and Fe40Cr3Ru, *Applied Surface Science*, vol. 44, pp. 263–269, (1990).
31. I.M. Wolff, L.E. Iorio, T. Rumpf, P.V.T. Scheers, and J.H. Potgieter, Oxidation and corrosion behaviour of Fe-Cr and Fe-Cr-Al alloys with minor alloying additions, *Materials Science and Engineering A*, vol. 241, no. 1-2, pp. 264–276, (1998).
32. R.T.K. Baker, and Jr. J.J. Chludzinski, In-situ electron microscopy studies of the- behaviour of supported ruthenium particles. Carbon deposition from catalysed decomposition of acetylene. *Journal of Physical Chemistry*, vol. 90, pp. 4734-4738, (1986).
33. M.L. Mabudafhasi, R. Bodkin, C.P. Nicolaides, X. Liu, M.J. Witcomb, and N.J. Coville, The ruthenium catalysed synthesis of carbon nanostructures. *Carbon,* vol. 40, pp. 2737-2742, (2002).
34. Y. Schuurman, C. Mirodatos, P. Ferreira-Aparicio, I. Rodrıguez-Ramos, and A. Guerrero-Ruiz, Bifunctional pathways in the carbon dioxide reforming of methane over MgO-promoted Ru\C catalysts. *Catalysis Letters,* vol. 66, pp. 33–37, (2000).
35. Z. Zeng, and K. Natesan, Initiation of metal-dusting pits and a method to mitigate metal-dusting corrosion. *Oxidation of Metals*, vol. 66, pp. 1–20, (2006).
36. Z. Zeng, and K. Natesan, Control of metal dusting corrosion in Ni-based alloys. *International Journal of Hydrogen Energy*, vol. 32, pp. 3640–3647, (2007).

37. E.M. Müller-Lorenz and H.J. Grabke, Coking by metal dusting of steels, *Materials and Corrosion*, vol. 50, pp. 614-621, (1999).
38. S. Strauß, R. Krajak and H.J. Grabke, Coking by metal dusting of nickel-base alloys, *Materials and Corrosion*, vol. 50, pp. 622-627, (1999).
39. C-Y. Lin and W-T Tsai, Nano-sized carbon filament formation during metal dusting of stainless steel, *Materials Chemistry and Physics*, vol. 82, pp. 929–936, (2003).
40. H.J. de Bruyn, E.H. Edwin and S. Brendryen, Apparent influence of steam on metal dusting corrosion, *NACE (2001)*, paper no. 01383, (2001).
41. P. Szakálos, Mechanisms and driving forces of metal dusting, *Materials and Corrosion*, vol. 54, pp. 752–762, (2003).
42. A. Agüero, M. Gutiérrez, L. Korcakova, T. T. M. Nguyen, B. Hinnemann, and S. Saadi, "Metal dusting protective coatings. A literature review," *Oxidation and Metals*, vol. 76, pp. 23–42, (2011).
41. D. Melo-Máximo, A.E. Murillo, O. Salas, L. Melo-Máximo and J. Oseguera, Behavior of uncoated and coated pure Fe in metal dusting conditions, *Surface and Coatings Technology,* vol. 308, pp. 10-18, (2016).
42. L. Melo-Máximo, O. Salas, D. Melo-Máximo, J. Oseguera, V.M. López-Hirata, R.D. Torres, C.M. Lepienski and R.M. de Souza, Performance of Cr oxide coatings on 304 steel against metal dusting, *Surface & Coatings Technology*, vol. 237, pp. 39–50, (2013).
43. A. Rouaix-Vande Put, K.A. Unocic, M.P. Brady, and B.A. Pint, Performance of chromia- and alumina-forming Fe- and Ni-base alloys exposed to metal dusting environments: The effect of water vapor and temperature, *Corrossion Science*, vol. 92, pp. 58–68, (2015).
44. P. Szakálos, R. Pettersson, and S. Hertzman, An active corrosion mechanism for metal dusting on 304L stainless steel, *Corrosion Science*, vol. 44, pp. 2253–2270, (2002).

5. Conclusions

The 304L stainless steel substrate was protected against metal dusting by the pulse plating deposited copper coatings. However, the copper was susceptible to oxidation, implying that the copper coatings would provide protection until the copper was depleted. Though deposition time resulted in thicker coatings which resulted in prolonged protection of the stainless 304L substrate, copper electroplating without reducing the oxidation, would not be sufficient for long exposure times to metal dusting environments.

The laser cladded samples were resistant to metal dusting at low carbon activities and relatively high oxygen partial pressures, especially the low ruthenium containing samples. It was also found that it was more beneficial to have ruthenium form a single phase with the 304L stainless steel for maximum protection whereas the enrichment of ruthenium accelerates the initiation and continued pitting of the alloy. Laser cladding and low ruthenium (0.5 wt.% Ru) concentrations showed the best resistance to metal dusting attack of all the laser cladded samples.

The copper electroplated samples performed better than the ruthenium laser cladded samples since the metal dusting of the laser cladded samples initiated just after seven days of exposure due to the failure of the chromium oxide layer. Though the oxide was able to heal it was still risky to use the method because subsurface attack continues during exposure. Utilising the copper pulse electroplating deposition method might also be problematic since attack of the substrate can occur below the coating as a result of the porosity of the coating, while providing the impression that the coating is resistant to attack and therefore protecting the substrate. This was caused by the oxidation of the coating, which allowed easy access for the corrosive gases to the substrate.

6. Recommendations

1. The oxidation of the copper electroplated samples may be improved by the addition of alloying elements such as Al, Mg, Be, therefore alloying the copper with these elements should be investigated.
2. Better adhesion of the copper electroplating should be investigated by adding a strike layer of nickel prior to the deposition of the copper to eliminate blistering.
3. Laser cladded samples with a more uniformly distributed homogeneous solid solution of ruthenium should be investigated.
4. The optimum ruthenium concentration for the low ruthenium concentration samples should be determined.